VIBRATION INDUCED DROPLET GENERATION FROM A LIQUID LAYER FOR EVAPORATIVE COOLING IN A HEAT TRANSFER CELL

A Thesis
Presented to
The Academic Faculty

By

Frank Pyrtle, III.

In Partial Fulfillment
Of the Requirements for the Degree
Doctor of Philosophy in Mechanical Engineering

Georgia Institute of Technology

December 2005

VIBRATION INDUCED DROPLET GENERATION FROM A LIQUID LAYER FOR EVAPORATIVE COOLING IN A HEAT TRANSFER CELL

Approved by:

Dr. William Z. Black, Co-advisor
School of Mechanical Engineering
Georgia Institute of Technology

Dr. James G. Hartley, Co-advisor
School of Mechanical Engineering
Georgia Institute of Technology

Dr. Kenneth A. Cunefare
School of Mechanical Engineering
Georgia Institute of Technology

Dr. William D. Hunt
School of Electrical and Computer Engineering
Georgia Institute of Technology

Dr. Laurence J. Jacobs
School of Civil and Environmental Engineering
Georgia Institute of Technology

Date Approved: August 10, 2005

To my wife Ashanti – Thank You.

and

In dedication to the memory of my loving mother, Lorna J. Pyrtle (1953-2002).

ACKNOWLEDGEMENTS

First, I would like to give honor to God, for He is the head of my life. In Him, I live, I move, and I have my being. Without Him, none of this would be possible.

This dissertation is representative of not only hard work, but is also the result of the encouragement and support of many people. I would like to thank my co-advisors, Dr. William Z. Black and Dr. James G. Hartley, for helping me navigate this course. Thank you Dr. Black, for all the time and support you gave me, even after retirement. Your commitment to my academic development during my graduate experience is greatly appreciated. Dr. Hartley, thank you for sharing your insight and wisdom that led to great ideas. I also thank Dr. Hunt for stepping in and offering support when I was running out of options. Dr. Jacobs thank you for your time and willingness to help when I asked. Finally, Dr. Cunefare, I thank you for your acute attention to the details of this work.

I am also thankful for my lab mates, fellow graduate students, and others who have helped me immensely: Dr. Sam Heffington, Sang Hun Lee, Desmond Stubbs, Anthony Dickherber, Pastor James and Wanda Turner, members of the Black Graduate Student Association, Jackie Worthy, Cosetta Williams, Norma Frank, Trudy Allen, Glenda Johnson, Teddy and Pam Taylor, and Paul Smith. To Willie Crayton, thank you for encouraging me to choose to attend college and to broaden my horizons, instead of pursuing my burgeoning career as a dairyman. I thank each of you for all your help getting me from the beginning to the end of this leg of my journey.

I would like to recognize the following entities for providing funding: the National Consortium for Graduate Degrees for Minorities in Engineering and Science,

Inc., the Georgia Institute of Technology Center for the Enhancement of Teaching and Learning, and Sigma Xi, The Scientific Research Society.

Of all, the person I am most thankful for is my wife, Dr. Ashanti J. Pyrtle. Without her love, patience, and support I certainly would not have finished. Thank you for your faithfulness, commitment, and willingness to postpone your career while I attended Georgia Tech. You are certainly my crown jewel.

Finally, I thank my natural and spiritual family. God placed you in my life to assist in the fulfillment of His ordained purpose and destiny for me. Thank you all for being His instruments to help reveal to me my purpose.

TABLE OF CONTENTS

LIST OF TABLES

LIST OF FIGURES

NOMENCLATURE

a	Acceleration (m/s^2)
A	Dimensionless amplitude
a^*	Dimensionless acceleration $[a \cdot t/(f \cdot d)^2]$
a^{**}	Dimensionless acceleration $[a \cdot t/(f \cdot d \cdot u_w)^2]$
A_H	Area of heat source (m^2)
A_s	Area of sink (m^2)
a_t	Threshold acceleration (m/s^2)
Bo	Bond number
c_p	Specific heat at constant pressure (J/(kg °C))
$c_{p,l}$	Specific heat at constant pressure of liquid (J/(kg °C))
d	Displacement of driver (m)
D_b	Average droplet diameter (m)
d_c	Critical wave amplitude (m)
f	Frequency (Hz)
Fr	Froude number
g	Gravitational acceleration (m/s^2)
G	Liquid mass flux ($kg/(m^2 s)$)
h	Heat transfer coefficient ($W/(m^2 °C)$)
h'_{fg}	Modified latent heat of vaporization (J/kg)
h_{avg}	Average heat transfer coefficient ($W/(m^2 °C)$)
h_{fg}	Latent heat of vaporization (J/kg)
h_{mist}	Heat transfer coefficient for droplet mist cooling ($W/(m^2 °C)$)

I_l	Resistor current (A)
k	Wavenumber (1/m)
k_l	Thermal conductivity of liquid (W/(m °C))
k_s	Thermal conductivity of sink (W/(m °C))
L	Characteristic length (m)
$\dot{m}$	Mass flow rate (kg/s)
P_{RMS}	Root mean square power (W)
q	Heat transfer rate (W)
q″	Heat flux (W/m^2)
R	Electrical resistance (ohms)
R_0	Average thermal resistance (°C/W)
R_l	Electrical resistance of resistor (Ω)
R1-R11	Thermal resistances in heat transfer cell model (°C/W)
Re	Reynolds number
R_s	Two-dimensional spreading resistance (°C/W)
t	Liquid layer thickness (m)
T	Temperature (°C)
T1-T6	Temperatures in heat transfer cell model(°C)
T_s	Temperature of surface (°C)
t_s	Thickness of sink (m)
T_{sat}	Temperature of fluid at saturation (°C)
U_s	Scaling velocity (m/s)
u_w	Wave speed (m/s)

V_{pp1}	Peak-to-peak voltage drop across driver and resistor (V)
V_{pp2}	Peak-to-peak voltage drop across driver (V)
We	Weber number

Greek Symbols

ΔT	Temperature difference (°C)
θ	Phase angle (degrees)
λ	Wavelength of surface waves (m)
μ	Dynamic viscosity (kg/(m s))
μ_l	Dynamic viscosity of liquid (kg/(m s))
ν	Kinematic viscosity (m^2/s)
π	Constant (3.14159…)
ρ_l	Density of liquid (kg/m^3)
ρ_v	Density of vapor (kg/m^3)
ρ	Density (kg/m^3)
σ	Surface tension (N/m)
φ	Constant
ω	Angular frequency (rad/s)
ω^*	Dimensionless frequency
Ω	Dimensionless frequency

SUMMARY

Current predictions suggest that thermal dissipation for high-performance microprocessors will approach 160 W, with regional surface heat fluxes that exceed 100 W/cm^2. One solution for effective thermal management of those microprocessors is the use of two-phase heat transfer devices. To dissipate the anticipated heat fluxes at prescribed operating temperatures, high-performance thermal management devices will be essential for the continued development of more powerful computers. Dissipation of high heat fluxes at low temperature differences is possible using thermal management devices that incorporate boiling and condensation.

In this investigation, vibration induced droplet generation from a liquid layer was examined as a means for achieving high heat flux evaporative cooling. Experiments were performed in which droplets were generated from a liquid layer using a submerged vibrating piezoelectric driver. During this investigation, the dependence of droplet generation on conditions related to parameters described during spray and driver characterization was determined. Those parameters include droplet mass flow rate, droplet size, driver frequency, driver voltage, and liquid layer thickness. The results showed that as the liquid layer thickness was increased, the frequencies at which droplet generation occurred decreased. Droplet mass flow rates were varied by adjustment of the liquid layer thickness, driver frequency, and driver voltage. After determining the dependence of the driver's displacement, velocity, and acceleration on frequency and voltage, the driver's characteristics were related to the occurrence of droplet generation. As a result, a frequency-dependent dimensionless parameter was developed for

determination of conditions necessary for droplet generation on the surface of the liquid layer. The dimensionless parameter is a combination of the Froude number and the driver acceleration. Results show that droplet generation occurs when the calculated dimensionless parameter is between distinct upper and lower bounds.

An analytical heat transfer model of a droplet cooling heat transfer cell was developed to simulate the performance of such a cell for thermal management applications. Using droplet flow rates determined as functions of driver voltage, driver frequency, liquid layer thickness, and interception distance, the heat transfer rate of a droplet cooling heat transfer cell was predicted for varied heat source temperatures and cell conditions. The heat transfer model was formulated in such a way as to accommodate a great number of parameter variations that can be used for the design of a simple heat transfer cell. The model was used to determine the effect of droplet cooling on the heat transfer rate from a heated surface, but it can also be used to determine the influence of other operating conditions that may be of interest for thermal management applications.

CHAPTER 1

INTRODUCTION

1.1 Background

As the semiconductor industry continues to make advances in the design of microchips, computation times continue to decrease, thereby enabling computers to increase computational speeds. Those design advances enable the chips to run at increasingly faster speeds, but with the drawback of increased heat production from smaller size components. Because of inherent internal electrical resistances in the materials used to build circuit pathways, heat generation is unavoidable. As the computing power of the industry's chips has increased, so have the heat fluxes and chip temperatures.

According to the International Technology Roadmap for Semiconductors, predicted thermal dissipation for high-performance microprocessors will approach 160 W within the next five years (Joshi, 2001). The resulting heat fluxes are anticipated to be well over 100 W/cm^2 in certain regions on the chip. To dissipate these heat fluxes, while still maintaining temperatures below prescribed limiting temperatures, more aggressive thermal management solutions will be essential for continued development of high-power computers. In 1999, the Semiconductor Industry Association identified thermal management as a key challenge during the next decade, for achieving projected performance goals of the semiconductor industry. Once employed only as a means to

prevent thermal failure, thermal management technology is now a necessary enabler for high-performance, high-power, and high-temperature electronics systems.

The need for more innovative thermal management solutions is driven by the proliferation of devices that incorporate the use of microprocessors in their designs. The growth of mobile computing, electronic hand-held devices, telecommunications systems, and automotive electronics systems are some of the applications that are driving the effort toward the miniaturization and design optimization of microprocessors.

In 1965, Gordon Moore observed an exponential growth in the number of transistors per integrated circuit and predicted that this trend would continue. As depicted in Figure 1.1, Moore's Law, the doubling of transistors placed in microprocessors every couple of years, has been maintained, and still holds true today.

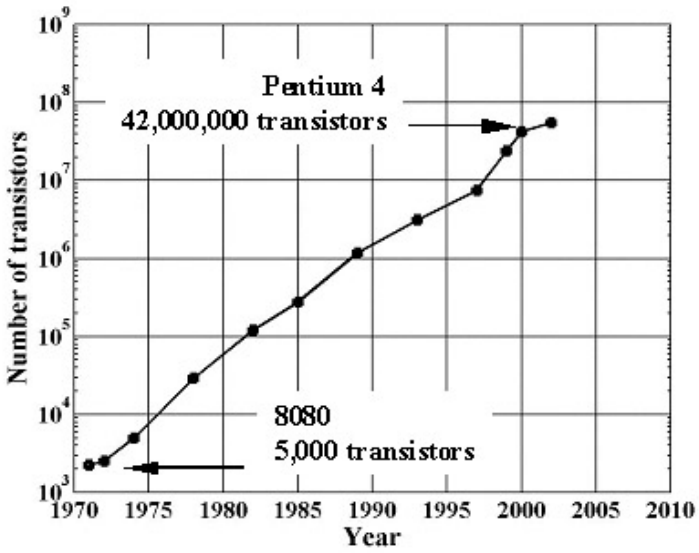

Figure 1.1: Moore's Law predictions of microprocessor transistor doubling (Wijetunga, 2002)

As the density of transistors continues to increase, power dissipation becomes a critical factor in the reliability of the device. Figure 1.2 indicates that microprocessor power requirements will approach 1,000 W by 2010, if current trends continue.

Miniaturization of microchip dies and increasing transistor densities produce higher heat fluxes, necessitating more sophisticated and higher performance thermal management solutions.

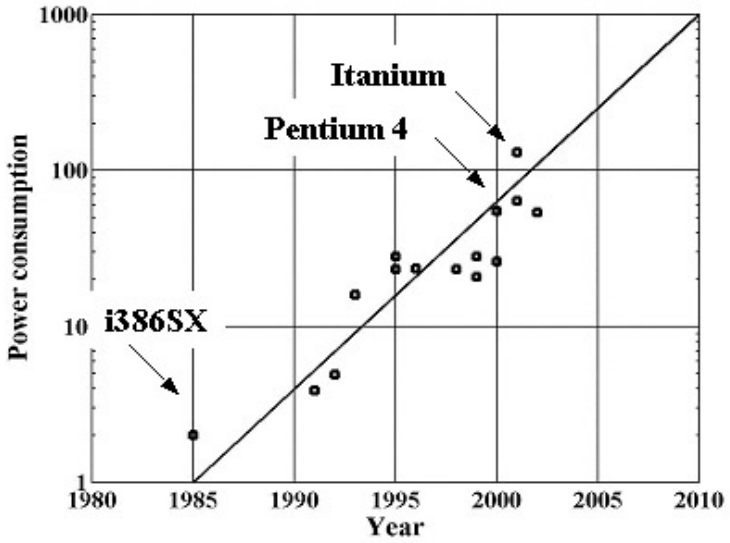

Figure 1.2: Microprocessor power requirements as a function of year (Wijetunga, 2002)

One solution for effective thermal management of high heat flux microprocessors is the use of two-phase heat transfer. Through boiling and condensation, two-phase heat transfer enables the dissipation of high heat fluxes at relatively low temperature differences. As shown in Figure 1.3, the heat transfer coefficients possible with cooling schemes that involve phase change are much greater than traditional forced convection heat transfer, which has been widely used for low-heat flux applications.

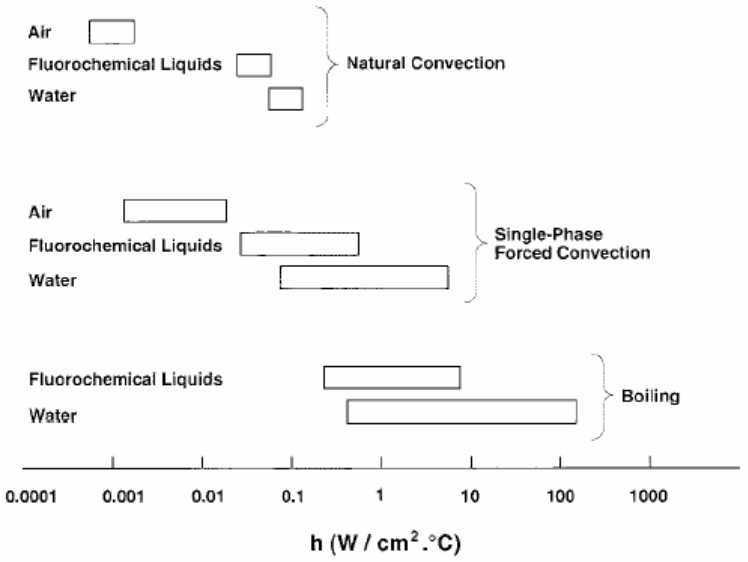

Figure 1.3: Convective and boiling heat transfer coefficients (Mudawar, 2001)

Evaporating liquid in a hot section and condensing vapor in a cold section of a heat transfer device, which is placed in contact with a microprocessor, has been proven to be an effective thermal management solution. These types of heat transfer devices, in the form of heat pipes, have been successfully used to provide high heat fluxes in a number of applications including the cooling of microprocessor packages.

Heat pipes are thermal devices that operate with the use of two-phase heat transfer and are often used to dissipate heat in various applications, including microelectronics. As shown in Figure 1.4, a simply configured heat pipe is a partially evacuated vessel with its internal walls lined with a capillary structure that is saturated with a working fluid. Since air in the heat pipe is evacuated and the heat pipe is charged with working fluid before it sealed, the internal pressure is determined by the vapor pressure of the working fluid.

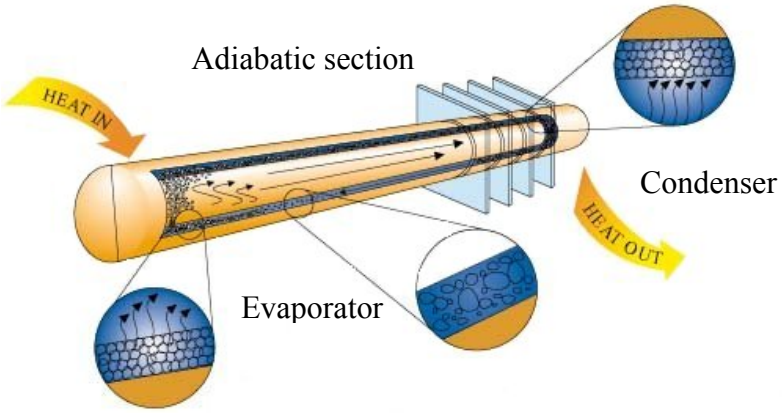

Figure 1.4: Simple heat pipe

When heat is transferred into the evaporator section, the fluid is vaporized, creating a pressure gradient in the pipe. This pressure gradient forces the vapor to flow along the pipe to the condenser section, where it changes phase, giving up its latent heat of vaporization. The working fluid is then pumped to the evaporator by the capillary forces developed in the capillary structure (Garner, 1996).

Heat pipes can be designed to operate in a broad range of temperatures, but have limitations that restrict their effectiveness for heat transfer. These limitations include viscous, sonic, capillary pumping, entrainment/flooding, and boiling limits, which are all dependent on the heat pipe operating temperature. Most limiting in the temperature range of electronics cooling applications is the capillary pumping limit (Faghri, 1995). This limitation is reached when nucleate boiling occurs in the capillary structure, creating vapor bubbles that block the flow of liquid from the condenser to the evaporator. Nucleate boiling initiation in the capillary structure is the result of locally higher heat fluxes in a particular area of the heat pipe.

The proposed research will study an alternative heat transfer device that relies upon the highly efficient phase change process but does not suffer from the issues that limit the operation of heat pipes. The alternate cooling scheme that will be examined in detail will be based on droplet generation from a liquid layer.

An alternative mechanism for delivering fluid to the evaporator section of a heat transfer device is liquid layer droplet generation, which avoids the limitations associated with capillary pumping. Vibration of a driver beneath a layer of liquid can cause droplet generation at the surface of the liquid layer. The droplets can be directed toward the heated surface of a microprocessor chip where they impinge on that surface. Heat is dissipated as the droplets contact the surface and change phase from liquid to vapor, cooling the surface. Since the phase-change heat transfer coefficient is much higher than that which occurs during single-phase forced convection, a more effective method of heat transfer for the same temperature difference results.

One design of a heat transfer cell based on droplet cooling, shown in Figure 1.5, has proven to be a viable solution for cooling surfaces that require high-heat flux dissipation rates. As shown by Heffington in 2000, heat transfer cells that use droplet cooling have been constructed and are able to achieve heat fluxes of greater than 100 W/cm^2, while the heated surface is maintained at temperatures less than 100°C. Therefore, preliminary research into the capability of simple heat transfer cells based on droplet generation technology has shown that they can meet the cooling requirements of future microprocessor designs.

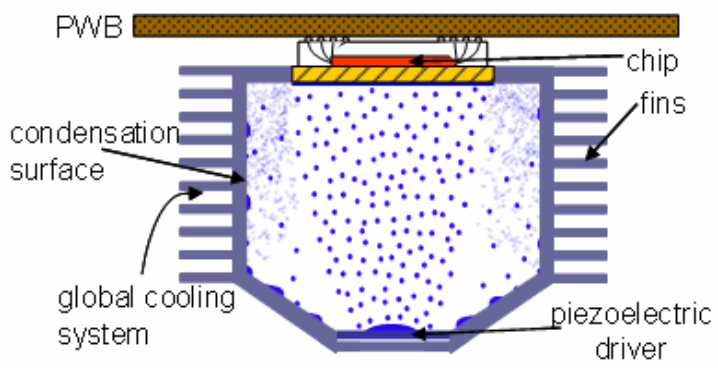

Figure 1.5: Schematic of a droplet cooling heat transfer cell (Heffington, 2000)

The purpose of this work was to determine the basic mechanisms that lead to droplet generation from a liquid layer and to identify the measurable physical parameters that are significant contributors to the phenomenon of droplet generation. The results were incorporated into a heat transfer cell model to predict heat transfer performance when a droplet generation-based cell is attached to a high heat flux source. Predictions of heat transfer performance were compared to the results of experimental work performed by Heffington. Description of the heat transfer cell and operating conditions are presented in Chapter 4.

1.2 Research Objectives

The hypothesis of this dissertation is: The measured droplet generation frequency range and driver displacement can be used to develop a method for determination of conditions necessary for droplet generation.

The motivation for this work comes from the need for a modeling tool that can be used to design heat transfer cells that are based on droplet cooling technology. The objectives of this research are to:

- Determine the parameters that influence the generation of droplets from the surface of a liquid layer.
- Develop a method to determine the conditions necessary for droplet generation.
- Develop an analytical model that can be used to predict the local and global heat transfer rates in a droplet cooling heat transfer cell.

To determine the ranges at which droplet generation occurs, experiments were performed to measure the piezoelectric driver's vibration frequency range and voltage needed to generate droplets for several liquid layer thicknesses. The velocity at the center of the piezoelectric driver was also measured to determine the displacement and acceleration as a function of frequency. Correlations were developed to determine the conditions necessary for the generation of droplets from the liquid layer using the driver and spray characterization results. This information was used as input to an analytical heat transfer model to predict the performance of a droplet cooling heat transfer cell.

CHAPTER 2

LITERATURE REVIEW

2.1 Spray Cooling

Cooling by means of small droplet sprays is of interest because the cooling capacity of liquid sprays often exceeds that for pool boiling or for liquid cooling by advection. Spray cooling effectiveness is higher because a thin layer of liquid can be maintained so that phase change occurs, and the thermal resistance of the liquid layer is minimized. When the liquid layer remains thin and the surface temperature is below the Leidenfrost temperature, a vapor blanket, which would insulate the surface, is not allowed to form. Instead, as vapor is formed in nucleation sites or other imperfections on the heated surface, it is more easily expelled from the surface without ever forming an insulating vapor. Those potential bubbles, if allowed to coalesce beneath the liquid layer result in an insulating vapor blanket, inhibit the heat transfer rate from the heated surface.

In 1969, Kopchikov et al. were able to dissipate 500 W/cm^2 from a surface with only 20ºC of excess temperature, using water sprays with droplets measuring 0.02 to 0.2 mm in diameter. Excess temperature is the difference between the surface temperature and saturation temperature of the liquid used to cool the surface. This achievement is significant because 500 W/cm^2 is more than four times greater than the heat flux possible at the same excess temperature for cooling by pool boiling of water at atmospheric pressure.

In an effort to determine the dependence of the critical heat flux on spray characteristics, Toda used spray nozzles with diameters ranging from 0.34 to 0.61 mm. His results, published in 1972, showed that the heat flux for a given droplet size, temperature, and velocity increased as the surface excess temperature increased. He also showed that the excess temperature at which critical heat flux occurred increased as the droplet size and velocity were increased. A spray-cooling curve, similar to the saturated pool-boiling curve was generated for wall-liquid temperature differences in excess of 200ºC. The cooling curve could be subdivided into three distinct regions: a low temperature region, a transitional temperature region, and a high temperature region. In the low temperature region, heat transfer was a result of evaporation of the liquid film at the liquid-vapor interface. In the high temperature region, heat transfer occurred through a film-boiling-like state, in which a vapor layer was formed between the liquid film and the heated surface, and evaporation was induced by convective heat transfer through the vapor layer in addition to radiation from the heated surface.

Toda's further mist cooling research, published two years later, resulted in the identification of spray droplet parameters that governed formation of a liquid film and formulation of equations quantifying heat transfer rates in the three regions of the spray-cooling curve. In the low temperature region, heat flux is greatly affected by the temperature, mass flow rate, and velocity of the subcooled droplets. In the transitional region, heat flux increases with mass flow rate and velocity, but is not appreciably affected by the subcooled droplet temperature.

Results of a heat transfer study that used mist cooling at low surface superheat were published by Bonacina et al. in 1979. Droplets measuring 90 μm in diameter with

velocities up to 2 m/s impinged on a heated surface, yielding a maximum heat flux of 215 W/cm^2. Assuming dropwise evaporation, a mathematical model was used to correlate the experimental results.

An investigation into nucleate boiling on a heated surface, sustained by water droplets impinging on a heated surface was conducted by Monde. Heat transfer was measured as a function of the volumetric flow rate and mean velocity of the droplets. Boiling curves were generated, and maximum heat fluxes of approximately 1,000 W/cm^2 were attained at 40ºC of surface superheat.

Shoji, et al., investigated mechanisms of cooling by subcooled droplets in the non-wetting regime for a wide range of droplet conditions. In this regime, the surface temperature is high enough that the droplets evaporate before actually contacting the surface. Water and ethanol were the liquids used in the experiments. During this experimental study, droplet diameters ranged from 0.88 to 2.54 mm, droplet velocities extended between 0.89 and 1.80 m/s, and the wall superheat temperatures were measured between 250 and 800°C. For the investigated conditions using water, the non-wetting regime began at a surface temperature of about 300°C. Due to the nature of the non-wetting conditions that existed during the experiments, the maximum heat transfer rates were severely restricted and were less than 10 W.

At Carnegie-Mellon University, Yao and Choi investigated the effects of liquid mass flux, droplet size and droplet velocity on heat transfer rates. The mono-size spray was created using a piezoelectric transducer to control the Rayleigh jets, which were used to create the droplets. An air supply stream was used to disperse the droplets over the heated surface, because the ejected droplets tended to travel in straight paths and

impacted only on fixed areas of the heater. The droplet diameters were held constant at 0.475 mm and velocities ranged from 4.02 to 5.84 m/s for surface temperatures of 100 to more than 400°C. The investigators found that when the liquid flux on the surface was kept low, the film boiling heat transfer rate was affected by droplet velocity and size. On the other hand, when the liquid flux was high, the droplet velocity and size had little affect on heat transfer rate. Liquid mass flux was determined to be the dominant parameter affecting the impacting spray heat transfer rate. The film boiling heat transfer of impacting sprays had a power-law dependency on the liquid mass flux with the power varying from unity to a fraction as the liquid mass flux increased.

Because the attainable heat flux is not governed solely by characteristics of the spray, it is also important to consider the condition of the heated surface. A study conducted at Purdue University in 1995 by Bernardin et al. found that surface roughness had a dramatic affect on the critical heat flux. In this study, water droplets with Weber numbers of 20 and 60 were sprayed onto three copper disks with different surface preparations. The critical heat fluxes obtained, in order from highest to lowest, were achieved for the particle-blasted, polished, and rough-sanded surfaces. The results indicated that the maximum critical heat flux occurred on the moderately rough, particle-blasted surface.

In a study by Pais et al., the effect of surface roughness on heat transfer was studied. With air-atomized nozzles using water, a thin liquid film was produced on the polished, heated surface. With surface roughnesses of less than 1 μm, heat fluxes in the range of 1,200 W/cm^2 were achieved. Based on results of the study, a new method for determining and designating the surface texture was proposed.

2.2 Droplet Cooling

While spray cooling and droplet cooling have many similar characteristics, they differ in one main attribute. Spray cooling is used to describe a heat transfer method in which the liquid droplets are propelled toward the heated surface by a carrier fluid, often pressurized air. Droplet cooling, on the other hand, is the term used to describe the heat transfer that results when the liquid is delivered to the heated surface by its own momentum. The vibration induced droplet atomization process studied in this thesis is classified as a droplet cooling technique.

Wachters et al. studied the heat transfer from a surface by the impingement of water droplets measuring 60 microns in diameter, traveling at a velocity of 5 m/s. Experiments were performed with surface temperatures up to 400°C. Results showed that the thermal properties and surface preparation of the heated surface, as well as the Weber number of the impacting droplets, affected the temperature of the heated surface.

In 1970, Pederson investigated droplet cooling using droplet diameters from 200 to 400 μm and droplet velocities from 2.44 to 10.06 m/s. He concluded that droplet velocity was the dominant parameter affecting the heat transfer rate. Pederson found that the surface temperature had little effect on the heat transfer rate in the non-wetting regime, the same finding later made by Shoji while conducting spray cooling experiments.

The evaporation of large water droplets (2.5 to 4.5 mm) on smooth surfaces of copper, brass, carbon steel, and stainless steel at temperature ranging from 80 to 450°C was investigated by Makino and Michiyoshi. High-speed photography was used to study the transient behavior of a water droplet on a heated surface initially at temperatures above the saturation temperature and finally at temperatures greater than the Leidenfrost

temperature. The measured data were used to calculate the time-averaged heat flux and the surface temperature for the heated surface placed in the path of the liquid droplets.

Xiong and Yuen investigated cooling of a hot stainless steel plate by small liquid droplets of water and hydrocarbon fuels. The study used droplet diameters that ranged from 0.07 to 1.8 mm and heater surface temperatures that ranged from 63 to 605°C. The critical heat flux for water was found to be 500W/cm^2 at a surface temperature of 155°C. Results showed that the maximum heat transfer rate is independent of droplet sizes for all tested hydrocarbon fuels and that the maximum heat transfer rate decreased slightly with increasing droplet sizes for water.

Kurokawa and Toda performed experiments using high-speed photography to study the impact of single droplets on glass. Using water, ethyl alcohol, and mercury, correlations were proposed for the maximum film diameter as functions of Weber number, Reynolds number, and droplet diameter. Droplet deformation and the subsequent formation of liquid film for droplet diameters between 1.3 and 2.3 mm and velocities between 2.1 and 2.3 m/s were analyzed. During impact, the heat transfer between the liquid film and the hot wall was dominant for the duration of evaporation of the droplet.

The maximum critical heat flux for a stream of monodispersed water droplets impacting a heated surface was studied by Halvorson et al. In this study, droplets having diameters between 2.3 and 3.8 mm, a velocity of 1.3 m/s, and frequencies of 2 and 15 drops per second impacted a heater surface at a temperature of 124°C. The maximum critical heat flux was 325 W/cm^2. The measurements showed that the critical heat flux increased with decreasing droplet diameter and increasing frequency, for a given mass

flux. The critical heat flux also increased with increasing mass flux, regardless of the droplet size or velocity.

Heat transfer from 2.58 mm diameter, monodispersed water droplets impinging on a heated surface was investigated by Sawyer et al. (1993). The velocity range of the droplets was 2.64 to 4.55 m/s, and a uniform mass flow rate of 0.140 g/s was maintained. The critical heat flux decreased significantly as droplet velocity increased.

Sawyer et al. (1997) continued investigating droplet cooling, using droplet diameters between 1.5 and 2.7 mm and velocities between 2.4 and 4.6 m/s with frequencies between 12 and 42 droplets per second. Maximum critical heat fluxes near 500 W/cm^2 were reached with surface superheats of 20°C, when the heat flux was based on the initial wetted area.

Using monodispersed droplets of diameters between 52 and 287 μm, and independent control of mass flow rate, droplet diameter, velocity, and frequency, Sheffield (1994) investigated heat fluxes from a heated surface. The maximum heat flux of 430 W/cm^2 resulted when the droplet diameter was 260 μm. For flow rates less than 0.05 g/s, the heat flux increased with decreasing droplet diameters and increasing velocities. For flow rates above 0.1 g/s the heat flux increased with increasing droplet diameters and decreasing velocities.

Continuing the droplet cooling investigation initiated by Sheffield, Denney (1996) used a drop-on-demand generator capable of low droplet generation frequencies. Low critical heat fluxes were obtained due to the formation of a liquid pool on the heater surface, which prevented the droplets from impacting the surface. Critical heat fluxes of up to 270 W/cm^2 were achieved.

Using the same device used by Sheffield, Sellers (2000) added an electrostatic deflector to control droplet spacing and velocity as they impacted a heated surface. Heat fluxes as high at 297 W/cm^2 at a surface temperature of 126°C, were obtained using droplet diameters between 97 and 392 μm that were produced at frequencies of 2.5 to 38 kHz. Results indicate a slight dependence of heat transfer on droplet size and velocity, while the droplet spacing was found to influence the heat flux by as much as 25 percent.

Heffington (2000) investigated the use of a vibrating piezoelectric diaphragm as a droplet generator within a heat transfer cell. During the development of this device, measurements showed that many parameters affect the heat transfer rates when a vibrating diaphragm is used to generate small liquid droplets. The ranges of frequencies of vibration that would create droplets were dependent on diaphragm attributes and liquid loading. Heat fluxes as high as 120 W/cm^2 were obtained at a heater surface temperature of approximately 95°C when the pressure of the heat transfer cell was reduced to 23.1 kPa. Results of the investigation showed that vibration-induced droplet atomization heat transfer cells provide an alternative means for cooling microelectronics. The purpose of Heffinton's work was not to characterize droplet generation, but to demonstrate the effectiveness of droplet generation for two-phase cooling. It is the purpose of the present investigation to determine the mechanisms that lead to droplet generation and to identify physical conditions necessary for the generation of droplets.

2.3 Vibration Induced Droplet Generation

To capitalize on the advantages of droplet cooling, small droplets of liquid must be generated in a reproducible and reliable fashion. The drops must then be propelled

toward the heated surface where they can remove heat from the surface as they evaporate. One way to generate droplets is to eject them from waves on a liquid layer by vibration of the layer at discrete frequencies. At certain frequencies, the waves on the liquid surface increase in amplitude and droplets are ejected from the wave crests.

Faraday (1831) performed qualitative experiments that showed that surface wave response was subharmonic to the forcing frequency. He discovered that the vibration period in the waves that formed on a thin liquid layer on a vibrating surface was twice the period of the driving vibration. The results of his work have been confirmed in subsequent Faraday wave investigations and experiments by other researchers. Later, Rayleigh (1896) showed that the surface tension of a liquid could be determined from the capillary wavelength observed on the surface of the vibrating liquid. He developed an equation relating the capillary wavelength, vibration frequency, and surface tension of the liquid. His work was later used by Lang (1962) to predict the mean diameters of droplets generated from the crests of capillary waves.

In 1927, Wood and Loomis described the atomization of a liquid by ultrasonic vibration. Using a quartz piezoelectric oscillator, atomization at the surface of an oil bath was generated at a driving frequency of 300 kHz. Later work by Sollner (1936), in which the physical nature of the atomization of a liquid was investigated, resulted in the hypothesis that cavitation was the mechanism for atomization by ultrasonic vibration. Droplet generation by cavitation was not the method by which droplets were produced in the present investigation.

In 1957, Sorokin published research work in which he found that a pattern of standing waves was generated on the surface of the liquid when the forcing vibration

amplitude exceeded a certain threshold value. When the amplitude of vibration was further increased, droplets formed at the wave crests and were ejected. In Sorokin's study, a vessel of water was vertically vibrated between 10 and 30 Hz to create the standing waves and droplets. Soon after, in 1959, Eisenmenger also investigated the mechanism of the parametric excitation of capillary waves and the conditions for the generation of droplets. His study was performed in the frequency range of 10 to 150 kHz. The results of Sorokin's work and Eisenmenger's work identified the ejection of droplets from capillary waves formed on the liquid surface. The frequency range used in the present research investigation falls between the ranges studied by these two researchers. The results of their work indicated that a minimum, forcing vibration amplitude would be necessary for the onset of droplet generation in the present investigation. For frequencies of 10 Hz to 30 Hz, droplet generation began when the forcing amplitude was 7 to 8 times the amplitude needed for wave generation. For frequencies of 10 kHz to 1.5 MHz, droplet generation began when the forcing amplitude was 4 times the amplitude needed for the generation of waves.

Building on the work of Rayleigh (1896), Lang (1962) ascertained that there was a relationship between the average diameter of the ejected droplets (D_b) and the capillary wavelength (λ). This relationship, $D_b = 0.34 \cdot \lambda$, was observed for working fluids including water, oil, and molten waxes at forced vibration frequencies of 10 kHz to 800 kHz. Lang postulated that atomization involved the rupture of capillary waves and subsequent ejection of surface particles from the wave peaks. In the present study, droplets were also generated by the detachment of liquid from the crests of waves, thus a relationship of droplet diameter to wavelength was expected to exist. The applicability of

Lang's relationship to the present investigation is discussed in the results section of Chapter 3.

Through their theoretical investigation, Peskin and Raco (1963) provided insight into the nature of atomization of liquid by means of vibration. They studied the mechanism of finite amplitude excitation of capillary waves on the surface of a liquid layer and determined the influence of the bottom surface of the liquid layer on the droplet characteristics. A dependence of the average droplet diameter on the amplitude of forced vibration and liquid layer thickness was derived,

$$\frac{D_b}{\pi d} = \left[\left(\frac{2\sigma}{\rho \omega^2 d^3} \right) 2 \tanh \left(\frac{\pi d}{D_b} \right) \left(\frac{t}{d} \right) \right]^{\frac{1}{3}}$$

In the present investigation, the frequency range in which droplet generation occurred was dependent on the liquid layer thickness and forced vibration amplitude, but the dependence of droplet diameter on liquid layer thickness was not observed. Because the ratio of the liquid layer thickness to the driver displacement (t/d) was in the range of 50 to 150 in this investigation, according to Peskin and Raco's equation, the liquid layer thickness would not measurably affect the average droplet diameter. According to their equation, the effect of the liquid layer thickness on droplet diameter is significant for ratios less than unity.

As Lang had already shown, Pohlmann and Stamm postulated in 1965, a relationship between droplet diameter and capillary wavelength. Motion pictures were used to observe the production of individual droplets during the atomization of the liquid layer. These motion pictures verified the proposed physical breaking away of droplets

from the crests of waves on the liquid surface. In the present investigation, the same method for droplet generation was observed.

Virnig et al. (1988) investigated wave motion in a rectangular container that was partially filled with water and vertically oscillated at frequencies less than 5 Hz. Their investigation did not include the generation of droplets but only the generation of waves. For several water depths (4.27 to 11.43 cm), the dependence of wave amplitude on both excitation frequency and excitation amplitude was found to be in good agreement with previously studied nonlinear theory predictions. Results of the experiments indicated the existence of a critical water depth, below which the frequency dependence of wave amplitude is qualitatively different from the frequency dependence for depths greater than this critical value. When the water level in the container was above this critical depth, the wave amplitude decreased with increasing frequency. When the water level in the container was below this critical depth, the wave amplitude increased with increasing frequency. The critical depth was predicted by analysis of three-dimensional nonlinear waves under vertical excitations to be 7.70 cm. The results of their experiments indicated that the critical depth was between 6.60 and 7.47 cm.

The waves produced in Virnig et al.'s investigation were gravity waves, which were predominantly restored by the force of gravity. The waves produced in the present investigation were capillary waves, which were predominantly restored by surface tension force. Although the liquid layer thicknesses of the Virnig et al. investigation (4.27 to 11.43 cm) and of the present investigation (1.3 to 6.1 mm) were dramatically different, the indication of an observed dependence of wave amplitude on liquid depth, driving frequency, and driving displacement was important. Because droplets detach

from waves on the liquid surface, conditions that affect wave formation also indirectly have an effect on droplet generation. In the present investigation, as the liquid layer thickness decreased, the frequency range in which droplet generation occurred increased.

In 1994, Kumar and Tuckerman investigated the linear stability of Faraday waves. They studied the stability boundaries of the interface between two fluids that were vibrated in a vertically oriented vessel at frequencies that lead to the generation of standing waves. They found that, for a given driving frequency, the instability occurs only for certain combinations of wavelength and driving amplitude. While Kumar and Tuckerman's investigation was analytical, Bechhoeffer et al. (1995) experimentally determined the linear stability of Faraday waves. Threshold accelerations and wavelengths necessary to excite surface waves in a vertically vibrated fluid container were measured and found to be in agreement with theoretical predictions. Based on their results, the investigator's expectation for the present investigation was that the driver acceleration would be an important factor for droplet generation.

As Bechhoeffer et al. had also done, Goodridge et al. (1996) performed experiments in which a container, partially filled with liquid, was vertically oscillated to generate droplets from the liquid surface, and the critical amplitudes for droplet ejection were measured. For low-frequency forcing (<60 Hz), gravity waves dominated droplet formation and for high-frequency forcing, capillary waves dominated. The critical acceleration to produce droplets was found to be dependent on the forcing frequency and liquid surface tension. Using the same apparatus, Goodridge et al. (1997) investigated the effects of viscosity on the ejection of droplets. The scaling law used to describe the critical acceleration needed to produce droplets was extended to include viscous effects.

In the present research, droplets were produced by the shedding of liquid from the crests of capillary surface waves. Goodridge et al.'s determination of a critical dimensionless acceleration for the production of droplets provided insight and a possible direction for determination of a dimensionless acceleration for the droplet generation configuration used in the present investigation.

Cerda and Tirapegui (1998) analytically investigated the effect of viscosity on the stability of a liquid layer. They confirmed that the response was subharmonic for low-viscosity fluids, which is a conclusion that is in agreement with the results of Faraday's experiment. For high viscosity fluids, the response could be harmonic, resulting in different mechanisms for producing instabilities.

In 2000, James investigated drop atomization that is a result of vibration of a single water drop placed on a piezoelectrically actuated flexible diaphragm. This experimental investigation was performed for frequencies between 600 to 1200 Hz. An analytical model of the experiments was formulated to describe droplet ejection. Additionally, an analytical investigation of vertical oscillation of a liquid layer was performed. Results indicated that threshold values of a dimensionless frequency and dimensionless amplitude are necessary for droplet ejection. Dimensionless parameters were developed that described drop dynamics during atomization. Despite the differences between atomization of a single drop and droplet generation from a liquid layer, James' investigation was another that identified the existence of a threshold displacement for droplet generation.

In 2002, Vukasinovic investigated the dynamics of the vibration induced droplet atomization process. Using water, he studied the membrane-drop interaction, instability

modes, and surface dynamics of the drop. In 2004, he also characterized the droplet spray that resulted from atomization of the original, larger liquid drop. Atomization of the drop occurred as a result of amplification of capillary waves that formed on the free surface of the drop. Investigation of the free surface dynamics of the drop also revealed three primary transitions before atomization. Atomization begins with axisymmetric standing waves that transition into azimuthal waves, which evolve at a sub harmonic of the driving frequency. The azimuthal waves then transition into a lattice mode just prior to a disordered pre-ejection state. In this research, the observation of a lattice arrangement of surface waves was also observed on the surface of the liquid layer. The lattice arrangement was visible at frequencies just below the lowest droplet generation frequency and just above the highest droplet generation frequency.

CHAPTER 3

METHODOLOGY

3.1 Driver-Droplet Generation Correlation

In this research, small droplets of water are generated by a vibrating driver that is submerged in a liquid pool. By applying appropriate voltages and frequencies of a sinusoidal input to the driver, waves are generated on the liquid surface. Small droplets are ejected from the wave crests and they travel upward, away from the liquid surface. Figure 3.1 shows a schematic of the configuration used to generate the droplet sprays.

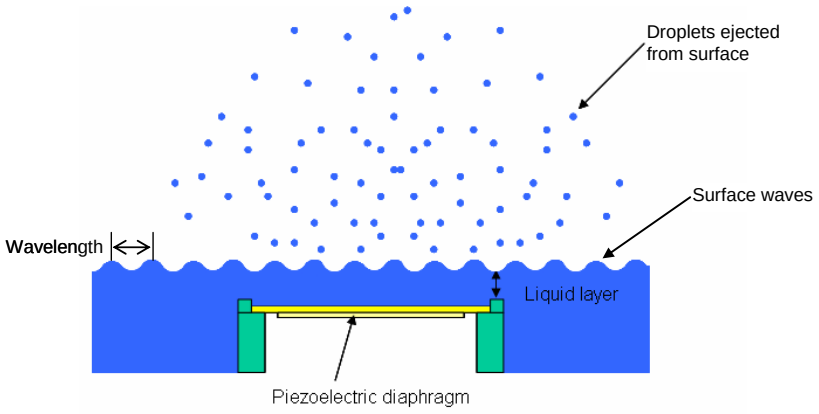

Figure 3.1: Schematic of droplet generation test setup

Droplet generation from the surface of the liquid layer is caused by the vibration of the driver, which is secured at the bottom of the liquid pool. Characteristics of driver vibration influence the ranges at which droplets will be produced. By using the driver's displacement and acceleration, as functions of frequency and voltage, relationships can be identified between the observed droplet generation and driver characteristics.

Insight into the vibration characteristics of the driver necessary to generate droplets can be derived from the work of several researchers. Notable work in the area of generation of water and ethanol droplets was performed by Goodridge et al. (1996). Their investigation focused on the creation and characterization of droplet generation from capillary waves on the free surface of a liquid that were caused by vertical oscillation of a partially filled liquid container.

Information about Goodridge et al.'s work is provided as background knowledge for analysis methods that were used in this research. To characterize the transition to droplet-ejecting waves, the threshold driving acceleration was measured as a function of forcing frequency. In their investigation, an electrodynamic shaker was used to provide excitation of the liquid and container. A threshold condition was determined by supplying sufficient acceleration to produce droplets and then the acceleration was lowered until droplet generation ceased. Using an accelerometer, which was attached to the armature of the shaker, the acceleration of the liquid and container was measured. Based on results of his experiments, it was determined that the threshold acceleration for the generation of droplets was dependent on the frequency of the vertical excitation and the surface tension of the fluid. Equation 3.1 is the observed dependence of threshold acceleration, a_t, as a function of angular vibration frequency, ω, according to results published by Goodridge et al.

$$a_t \sim \omega^{4/3} \tag{3.1}$$

where

$$\omega = 2\pi \cdot f \tag{3.2}$$

A dimensionally consistent form, which combined the dependent parameters of frequency and surface tension, was determined by Goodridge et al. and is shown in Equation 3.3. The constant was empirically determined from the experimental data.

$$a_t = 0.239\omega^{4/3}(\sigma/\rho)^{1/3} \qquad 3.3$$

Goodridge et al. used Equation 3.3 to predict the threshold acceleration necessary for droplet generation from a vertically oscillating, partially filled liquid container.

Goodridge et al.'s later investigation (1997) into the effects of viscosity on droplet generation yielded two dimensionless quantities that they used to describe the threshold acceleration necessary for droplet generation. These quantities of dimensionless acceleration, a^*, and dimensionless angular frequency, ω^*, are expressed in Equations 3.4 and 3.5.

$$a^* = \frac{a\nu^4}{(\sigma/\rho)^3} \qquad 3.4$$

$$\omega^* = \frac{\omega\nu^3}{(\sigma/\rho)^2} \qquad 3.5$$

The resulting dimensionless acceleration, graphed as a function of dimensionless angular frequency in Figure 3.2, represents the threshold values for which droplet generation will occur from vertical oscillation of a partially filled liquid container. The circular markers in the figure represent the dimensionless acceleration and dimensionless angular frequency determined for the experimental data. In the lower-viscosity region ($\omega^* < 10^{-6}$) and the higher-viscosity region ($\omega^* > 10^{-3}$), the theoretical threshold values are below the experimentally determined threshold values. Conditions for which the calculated dimensionless acceleration and dimensionless angular frequency appear above the line indicate the generation of droplets. Conditions for which the calculated dimensionless

acceleration and dimensionless angular frequency are below the solid line shown in Figure 3.2 indicate conditions at which droplet generation does not occur.

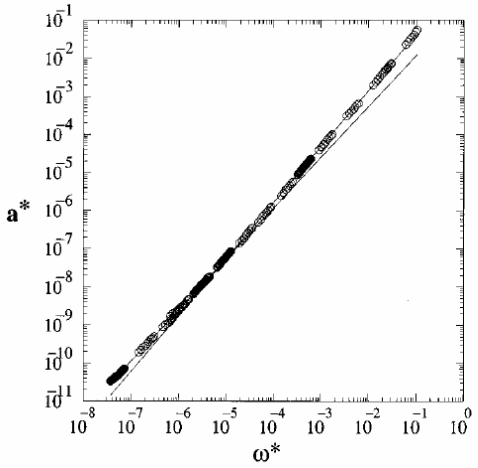

Figure 3.2: Dimensionless acceleration as a function of dimensionless angular frequency (Goodridge et al., 1997)

In their investigation, Goodridge et al. determined the threshold accelerations for low-viscosity liquids, where surface tension effects dominate, to be expressed as

$$a_t = 0.261\omega^{4/3}(\sigma/\rho)^{1/3} \qquad 3.6$$

and threshold accelerations for high-viscosity liquids to be expressed as

$$a_t = 1.306\nu^{1/2}\omega^{3/2} \qquad 3.7$$

where the constants were empirically determined.

As in Goodridge et al.'s work, the present investigation reported in this dissertation involves the generation of droplets from the surface of a vibrating liquid layer. Although there are similarities between the mechanisms for droplet generation in the work of Goodridge et al.'s and in the present study, distinctly different methods for excitation of the liquid were implemented. Due to the different methods of excitation used to generate droplets, Equations 3.3 to 3.7 were not used for analysis of this

investigation's experimental results. Key differences between the experimental investigations are as follows.

Goodridge et al.:

- The entire body of liquid and container were vertically oscillated
- The liquid depth was held constant for all experiments
- Multiple liquids were used so that the effects of surface tension and viscosity could be determined
- Frequency range, 20 to 80 Hz
- Liquid layer thickness, 10.0 cm

Current study:

- The liquid layer above the driver was vibrated in an open pool and in a pool with constrained boundaries
- The liquid depth was varied to determine its effect on droplet generation
- Distilled water was the sole liquid used
- Frequency range, 360 to 575 Hz
- Liquid layer thickness, 1.28 to 6.1 mm

The differences, itemized above, have implications for the expected results and the experimental methods used to generate droplets. The differences would affect the droplet diameters, required forced displacements, and surface wave amplitudes. In relationship to droplet generation, the longer wavelengths of gravity waves produce larger droplets than those produced from shorter wavelength capillary waves.

In the present investigation, a piezoelectric diaphragm, clamped around its perimeter, was used to vibrate the liquid layer. Therefore, the acceleration and

displacement of the lower surface of the liquid layer were not uniform. The distribution of acceleration and displacement over the surface of the vibrating driver was nearly paraboloid in shape, with the maximums occurring at the center of the driver. Goodridge et al. used an electrodynamic shaker to oscillate a solid, piston-like driver, which created uniform displacement and acceleration of the liquid layer. The nearly paraboloid shape of the velocity distribution on the surface of the driver is shown in Figures 3.10 to 3.12.

The thickness of the liquid layer was varied in the present investigation, which led to variations in the induced capillary wave speeds that are generated on the free surface of the liquid. This wave behavior is discussed later in Section 3.4.2. In Goodridge et al.'s experiments, where the liquid layer was of a constant thickness, the calculated parameters used to define a threshold for droplet generation were not functions of the thickness of the liquid layer thickness. Droplet generation from a liquid layer thickness similar to that used in Goodridge et al.'s investigation (10.0 cm) could not be reproduced in the present investigation because the necessary displacement could not be produced by the piezoelectric driver.

Differences between the configurations used in the present investigation and the configuration used by Goodridge, et al. are seen in the boundary conditions applied to the momentum equations for a Newtonian fluid with constant density and constant viscosity. These equations could be solved to determine the velocity distributions in the liquid body above the driver. The following momentum equations were simplified assuming the pressure field throughout the fluid was uniform and no body forces in the r and θ directions, resulting in the equations below.

$$\rho\left(\frac{\partial v_r}{\partial t}+v_r\frac{\partial v_r}{\partial r}+\frac{v_\theta}{r}\frac{\partial v_r}{\partial \theta}-\frac{v_\theta^2}{r}+v_z\frac{\partial v_r}{\partial z}\right)=\mu\left[\frac{\partial}{\partial r}\left(\frac{1}{r}\frac{\partial}{\partial r}(rv_r)\right)+\frac{1}{r^2}\frac{\partial^2 v_r}{\partial \theta^2}+\frac{\partial^2 v_r}{\partial z^2}-\frac{2}{r^2}\frac{\partial v_\theta}{\partial \theta}\right]$$

$$\rho\left(\frac{\partial v_\theta}{\partial t}+v_r\frac{\partial v_\theta}{\partial r}+\frac{v_\theta}{r}\frac{\partial v_\theta}{\partial \theta}+\frac{v_\theta v_r}{r}+v_z\frac{\partial v_\theta}{\partial z}\right)=\mu\left[\frac{\partial}{\partial r}\left(\frac{1}{r}\frac{\partial}{\partial r}(rv_\theta)\right)+\frac{1}{r^2}\frac{\partial^2 v_\theta}{\partial \theta^2}+\frac{\partial^2 v_\theta}{\partial z^2}+\frac{2}{r^2}\frac{\partial v_r}{\partial \theta}\right]$$

$$\rho\left(\frac{\partial v_z}{\partial t}+v_r\frac{\partial v_z}{\partial r}+\frac{v_\theta}{r}\frac{\partial v_z}{\partial \theta}+v_z\frac{\partial v_z}{\partial z}\right)=\mu\left[\frac{1}{r}\frac{\partial}{\partial r}\left(r\frac{\partial v_z}{\partial r}\right)+\frac{1}{r^2}\frac{\partial^2 v_z}{\partial \theta^2}+\frac{\partial^2 v_z}{\partial z^2}\right]-\frac{\partial p}{\partial z}+\rho g_z$$

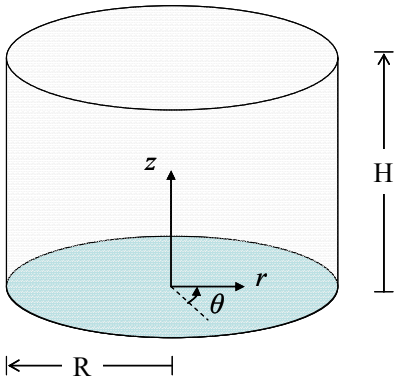

Figure 3.3: Schematic of liquid body

Figure 3.3 is the representative liquid body to which the following boundary conditions are applicable and from which droplets would be generated at its liquid-gas interface (z = H) in the present investigation and in Goodridge et al.'s investigations. For Goodridge et al.'s investigation, in which a container of liquid was vertically oscillated, the following initial and boundary conditions would be applicable.

$v_r(r,\theta,z,0)=v_\theta(r,\theta,z,0)=v_z(r,\theta,z,0)=0$ Initial conditions

$v_r(r,\theta,0,t)=0$

$\mu\left.\frac{\partial v_r}{\partial z}\right|_{r,\theta,H,t}=\mu_{air}\left.\frac{\partial v_{r,air}}{\partial z}\right|_{r,\theta,H,t}$ Radial boundary conditions

$v_\theta(r,\theta,0,t)=0$

$v_\theta(R,\theta,z,t)=0$ Polar boundary conditions

$$v_z(R,\theta,z,t) = V_{\max}\sin(\omega t)$$

$$\left.\frac{\partial v_z}{\partial \theta}\right|_{0,\theta,z,t} = 0 \qquad \text{Axial boundary conditions}$$

The radial velocity of the liquid, v_r, is zero at the bottom of the container, due to the no-slip condition. At the liquid-gas interface on the surface of the liquid body, the shear stress in the liquid equals the shear stress in the air. At the bottom and at the sidewalls of the container, the polar velocity of the liquid, v_θ, is zero due to the no-slip condition. At the sidewalls of the container, the axial velocity of the liquid, v_z, equals the velocity of the container due to the no-slip condition. $V_{\max}$ is the maximum velocity of the container during oscillation. Along the axial centerline of the liquid body, the axial velocity is independent of the polar angle.

In the present investigation, for experiments performed in an open pool, the initial and boundary conditions for the momentum equations follow.

$$v_r(r,\theta,z,0) = v_\theta(r,\theta,z,0) = v_z(r,\theta,z,0) = 0 \quad \text{Initial conditions}$$

$$\left.\frac{\partial v_r}{\partial \theta}\right|_{0,\theta,z,t} = 0$$

$$\left.\mu\frac{\partial v_r}{\partial z}\right|_{r,\theta,H,t} = \mu_{air}\left.\frac{\partial v_{r,air}}{\partial z}\right|_{r,\theta,H,t} \qquad \text{Radial boundary conditions}$$

$$v_\theta(r,\theta,0,t) = 0$$

$$\left.\mu\frac{\partial v_\theta}{\partial z}\right|_{r,\theta,H,t} = \mu_{air}\left.\frac{\partial v_{\theta,air}}{\partial z}\right|_{r,\theta,H,t} \qquad \text{Polar boundary conditions}$$

$$v_z(r,\theta,0,t) = V_{\max}\left(1-\left(\frac{r}{R}\right)^2\right)\sin(\omega t)$$

$$\left.\frac{\partial v_z}{\partial \theta}\right|_{0,\theta,z,t} = 0 \qquad \text{Axial boundary conditions}$$

Along the axial centerline of the liquid body, the radial and the axial velocities are independent of the polar angle. At the liquid-gas interface on the surface of the liquid body, the radial and polar shear stresses in the liquid equal the shear stresses in the air. Due to the no-slip condition, the polar velocity of the liquid in contact with the driver surface is zero, and the axial velocity of the liquid in contact with the driver equals the velocity of the vibrating driver. As the driver vibrates, its displacement profile is nearly paraboloid in shape.

For the present investigation, experiments were also performed in a pool constrained by a solid circular boundary. For a configuration in which the inner diameter solid boundary is equal to the diameter of the driver, the following initial and the boundary conditions for the momentum equations apply.

$$v_r(r,\theta,z,0) = v_\theta(r,\theta,z,0) = v_z(r,\theta,z,0) = 0 \quad \text{Initial conditions}$$

$$\left.\frac{\partial v_r}{\partial \theta}\right|_{0,\theta,z,t} = 0$$

$$\mu \left.\frac{\partial v_r}{\partial z}\right|_{r,\theta,H,t} = \mu_{air} \left.\frac{\partial v_{r,air}}{\partial z}\right|_{r,\theta,H,t} \quad \text{Radial boundary conditions}$$

$$v_\theta(R,\theta,z,t) = 0$$

$$v_\theta(r,\theta,0,t) = 0 \quad \text{Polar boundary conditions}$$

$$v_z(R,\theta,z,t) = 0$$

$$v_z(r,\theta,0,t) = V_{\max}\left(1 - \left(\frac{r}{R}\right)^2\right)\sin(\omega t) \quad \text{Axial boundary conditions}$$

The radial velocity at the center of the liquid body is independent of the polar angle. At the liquid-gas interface on the surface of the liquid body, the radial shear stress in the liquid equal the shear stress in the air. The polar velocities of the liquid in contact with the constraining boundary and in contact with the driver are zero, due to the no-slip

condition. The axial velocity of the liquid in contact with the constraining boundary is also zero, due to the no-slip boundary condition. The axial velocity of the liquid in contact with the driver equals the velocity of the vibration driver. The circular rings used in this investigation were not the same diameter as the driver. The velocity field results for this constrained pool and for the open pool would represent the two extremes between which, would be the expected velocity field results for the constrained pool configurations used in this investigation.

For all three configurations, the initial conditions and liquid-gas interface boundary conditions are the same. However, the boundary conditions at the solid-liquid interfaces are different, which means the solutions for the motion of the liquid layer differ. The velocity of the fluid in all directions is initially zero, and the shear stress at the liquid surface equals the shear stress in the air. Solution of the momentum equations is not made in this dissertation, but differences in the boundary conditions indicate that a different solution exists for the time-dependent velocity fields within the liquid body. Differences in the velocity fields at the liquid surface would indicate variations in surface wave motion, and thus different droplet generation characteristics.

3.2 Driver Characterization

The driver used in the present investigation is a piezoelectric diaphragm, which consists of two parts; a piezoelectric element and a thin metal plate onto which the piezoelectric element is bonded, as shown in Figure 3.4. The piezoelectric element is a sintered body of poly-crystals that distorts when a voltage is applied to it. The specific piezoelectric element used throughout this investigation was made of PZT (Lead Zirconate Titanate) and the metal plate was made of an iron nickel alloy. The metal

plate was 31.75 mm in diameter and 0.10 mm thick. The diameter and thickness of the piezoelectric element used in the experiments reported in this dissertation measured 19.7 mm and 0.22 mm, respectively.

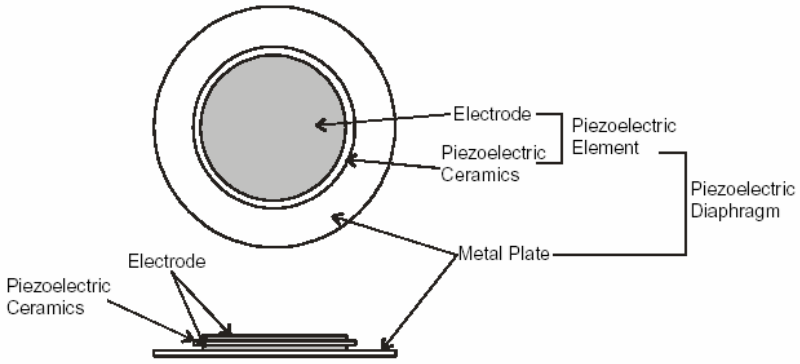

Figure 3.4: Schematic of piezoelectric diaphragm and components

Deflection of the piezoelectric diaphragm is the result of shear stresses exerted by the piezoelectric element on the metal plate when a voltage is applied. When DC voltage is applied, the piezoelectric element distorts by radial expansion causing the metal plate to bend as shown in Figure 3.5(a). By reversing the polarity of the DC voltage the piezoelectric element contracts, causing the metal plate to bend in the opposite direction as shown in Figure 3.5(b). When an AC voltage is applied across the electrodes, the diaphragm alternates bending in both directions at the frequency of the applied voltage and the repeated bending of the diaphragm motion produces vibration.

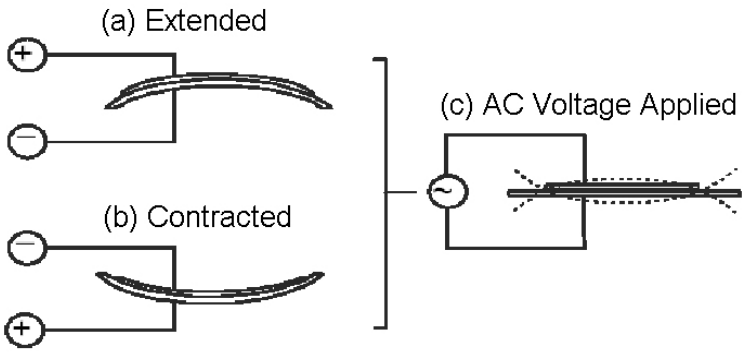

Figure 3.5: Schematic of piezoelectric diaphragm deflection

Knowledge of the displacement and acceleration of the driver is essential for the analysis of droplet generation from a liquid layer. As evidenced by results of previous research experiments that involve droplet generation, from Faraday to Goodridge, the forcing amplitudes, accelerations, and frequencies are crucial for droplet generation. Unlike previous research investigations into droplet generation from a liquid layer by vertical oscillation of a rigid plate, the droplet generation in this research was caused by vibration of a flexible membrane.

To determine the driver displacement and acceleration, a laser vibrometer was used to measure the velocity at the center of the dry driver for the range of frequencies and driver voltages used during the experiments. Using the velocity measurements, displacement and acceleration at the center of the driver were calculated. Velocity measurements at different azimuthal locations on the surface of the driver were used to verify the axisymmetry of the driver vibration.

3.2.1 Apparatus and Procedures

The laser vibrometer used to measure the velocity of the driver was a Polytec PSV-200 scanning vibrometer. Laser Doppler vibrometry (LDV) is a non-contact vibration measurement technique using the Doppler Effect. Laser vibrometers can be used to make measurements of many of types of surfaces without influencing them by mass loading. The PSV-200 uses a low-power Helium-Neon laser, and is a two-beam interferometric device that detects the phase difference between an internal reference and a measurement beam. The measurement beam is focused on the target and scattered back to the interferometer. Using the heterodyne principle, detection of the vibration direction is possible by demodulation of the frequency-modulated carrier signal.

The Polytec PSV-200 consisted of a scanning head, vibrometer controller, remote focus control, personal computer system, video control box, pan/tilt head, and tripod. Positioning and focusing of the laser, by the scanning head, is controlled using the proprietary software installed on the personal computer system. This system was also used to control the signal generator that powered the driver. Data acquisition was also performed using the proprietary software provided on the computer system.

The driver, mounted in its enclosure, was secured to a tripod and positioned approximately 1.5 meters from the scanning head of the vibrometer. The laser light spot from the scanning head was positioned on the surface of the driver. The exact position of the laser was then adjusted to the center of the driver face using the computer software. After positioning the laser spot at the center of the driver, the focal point of the laser light beam was adjusted until maximum signal strength was indicated in the software control program. The signal strength is a measurement of the amount of laser light reflected

from the driver face back to the receiver, which is housed within the scanning head. Because the driver face is a highly reflective nickel-alloy, the signal strength was indicated as maximum during all experiments.

3.2.1.1 Electrical Power Measurement

The voltage across the driver was measured and the power calculated for each experiment. The driver was powered with an AC sine waveform, using a signal generator. A step-up transformer was used to increase the voltage from the signal generator to meet the desired power requirements of the driver. To calculate the current through the driver, the voltage was measured across a resistor that was placed in series with the driver, as shown in Figure 3.6. Using the oscilloscope, the voltage drops across the driver (V_{pp2}) and the driver-resistor combination (V_{pp1}), and the phase between the voltages signals were measured. A schematic of the electrical circuit used to power and monitor the driver is presented in Figure 3.6.

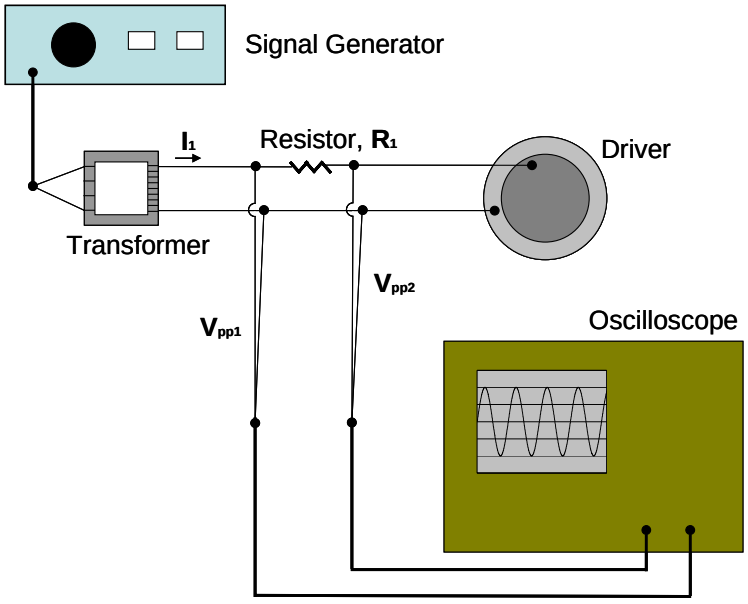

Figure 3.6: Schematic of power/monitoring circuit of driver

The first step in calculating the power required to operate the driver was to monitor the voltage drops across the driver-resistor combination (V_{pp1}) and the driver (V_{pp2}). The difference between the two voltage drops yielded the voltage drop across the resistor (R_1). The phase angle (θ) between V_{pp1} and V_{pp2} was recorded and the resistor power ($P_{RMS,1}$) was calculated.

$$P_{RMS,1} = \frac{(V_{pp1} - V_{pp2})^2}{R_1} \cos(\theta \frac{\pi}{180}) \quad 3.8$$

The current through the resistor (I_1), which is the same as through the driver, was then calculated.

$$I_1 = \frac{P_{RMS,1}}{(V_{pp1} - V_{pp2})} \quad 3.9$$

Finally, the power dissipated by the driver ($P_{RMS,driver}$)was calculated.

$$P_{RMS,driver} = (I_1 V_{pp2}) \frac{\sqrt{2}}{2} \quad 3.10$$

The voltages, V_{pp1} and V_{pp2}, were recorded for calculation of the power required to operate the driver, and for use in relating droplet generation conditions to the displacement and acceleration of the driver. The displacement and acceleration is dependent on the frequency and voltage applied to the driver (V_{pp2}). The frequencies and voltages were tabulated and referenced to determine driver velocities, displacements, and accelerations to relate driver and droplet generation characteristics.

3.2.1.2 Driver Velocity Measurement

To measure the velocity at center the driver, the frequency and voltage supplied by the signal generator to the driver-resistor combination (V_{pp1}) were adjusted to the

desired values. The time-dependent velocity at the specified voltage and frequency were recorded, along with driver voltage (V_{pp2}), to a data file for each test condition. The sampling rate and test durations were set and held constant for all tests at 256 kHz and 8 milliseconds.

To create the contour plots used to verify the axisymmetry of driver vibration, the scanning features of the laser vibrometer system were used. A grid was generated that covered the surface of the driver using the video camera that was built into the laser vibrometer. The frequency and voltage of the signal generator were set and the scanning head of the laser vibrometer was moved through the points of the prescribed grid and the maximum velocity was recorded at each point. This procedure was used to create the contour plots presented in Figures 3.10 to 3.12 of Section 3.2.2.

The maximum velocity at the center of the driver was determined from the time-dependent velocity measurements for the range of test conditions indicated in Table 3.1. Using the velocity measurements, the maximum displacements and maximum accelerations were determined.

Table 3.1: Driver test conditions for measurements made with laser vibrometer

Waveform	*Frequency (Hz)*	V_{pp1} *(V)*
Sine	300-1000	15 – 50

The driver velocity, v, varies with time according to Equation 3.11.

$$v(t) = V_{\max} \sin(2\pi ft) \qquad 3.11$$

The displacement of the driver, d, is

$$d(t) = \int v(t)dt = -\frac{V_{\max}}{2\pi f}\cos(2\pi ft) \qquad 3.12$$

The driver acceleration, *a*, is

$$a(t) = \frac{dv}{dt} = 2\pi f V_{\max}\cos(2\pi ft) \qquad 3.13$$

Thus, the maximum displacement and maximum acceleration at the center of the driver are scalar multiples of the measured maximum velocity at the center of the driver as shown in Equations 3.14 and 3.15.

$$d_{\max} = \frac{V_{\max}}{2\pi f} \qquad 3.14$$

$$a_{\max} = 2\pi f V_{\max} \qquad 3.15$$

The maximum velocity per volt is graphed as a function of frequency for the driver in Figure 3.7. The maximum displacement and maximum acceleration per volt are graphed as functions of frequency in Figures 3.8 and 3.9. The shapes of the graphs in Figures 3.7 to 3.9 are similar because the maximum displacement and maximum acceleration are scalar multiples of the maximum velocity. The data reported in Table 3.2, are the driver voltages (V_{pp2}) applied during measurement of the velocity at the center of the driver. The driver-resistor voltage (V_{pp1}), was held constant at each frequency and the driver voltage was recording during velocity measurement.

3.2.2 Results

Graphs of the maximum velocity, displacement, and acceleration per volt as functions of frequency are presented in Figures 3.7-3.9. Each graph represents the relationship of the independent variable (velocity, acceleration, or displacement) per unit input voltage in the frequency domain. The range of frequencies in which droplets were

generated in this investigation was 360 to 575 Hz. Reported in Table 3.2, are the driver voltages (V_{pp2}) that were recorded at each frequency for constant driver-resistor combination voltages (V_{pp1}).

Table 3.2: Driver voltages (V_{pp2}) for constant V_{pp1}, during driver characterization

		V_{pp2} (V)				
Frequency (Hz)	**V_{pp1} (V) →**	**30**	**35**	**40**	**45**	**50**
300		29.8	34.8	39.8	44.6	49.2
320		29.8	34.7	39.7	44.5	49.2
340		29.8	34.6	39.6	44.4	49.2
360		29.8	34.6	39.6	44.4	49.2
380		29.7	34.6	39.6	44.4	49.2
400		29.7	34.6	39.5	44.4	49.2
420		29.7	34.6	39.4	44.4	49.2
440		29.7	34.6	39.4	44.4	49.2
460		29.6	34.6	39.4	44.4	49.2
480		29.6	34.5	39.4	44.3	49.0
500		29.6	34.4	39.4	44.2	48.8
520		29.6	34.3	39.3	44.1	48.8
540		29.5	34.2	39.2	44.0	48.8
560		29.5	34.2	39.2	44.0	48.7
580		29.5	34.2	39.2	44.0	48.6
600		29.5	34.2	39.1	43.8	48.5
620		29.4	34.2	39.0	43.6	48.4
640		29.4	34.1	38.9	43.6	48.3
660		29.3	34.0	38.8	43.6	48.2
680		29.2	34.0	38.7	43.4	48.0
700		29.1	34.0	38.6	43.2	47.8
720		28.9	33.6	38.2	42.7	47.3
740		28.7	33.2	37.8	42.2	46.8
760		28.3	32.6	36.4	39.4	43.6
780		26.6	29.2	32.4	36.4	40.6
800		25.0	29.6	34.4	39.0	43.4
820		26.8	31.8	36.2	41.4	46.0
840		26.9	31.4	36.0	40.8	45.2
860		27.9	32.5	37.1	42.0	46.5
880		28.9	33.6	38.2	43.2	47.8
900		29.1	33.8	38.5	43.3	48.1
920		29.2	34.0	38.8	43.4	48.4
940		29.2	34.0	38.8	43.4	48.3
960		29.2	34.0	38.8	43.4	48.2
980		29.2	34.0	38.8	43.4	48.1
1000		29.1	34.0	38.8	43.4	48.0

A graph of the maximum velocity per volt, measured at the center of the driver, as a function of frequency is shown in Figure 3.7. At a specific frequency, the velocity is determined by multiplying the velocity per volt by the measured driver voltage. The range of frequencies in which droplets were generated in this investigation was 360 to 575 Hz.

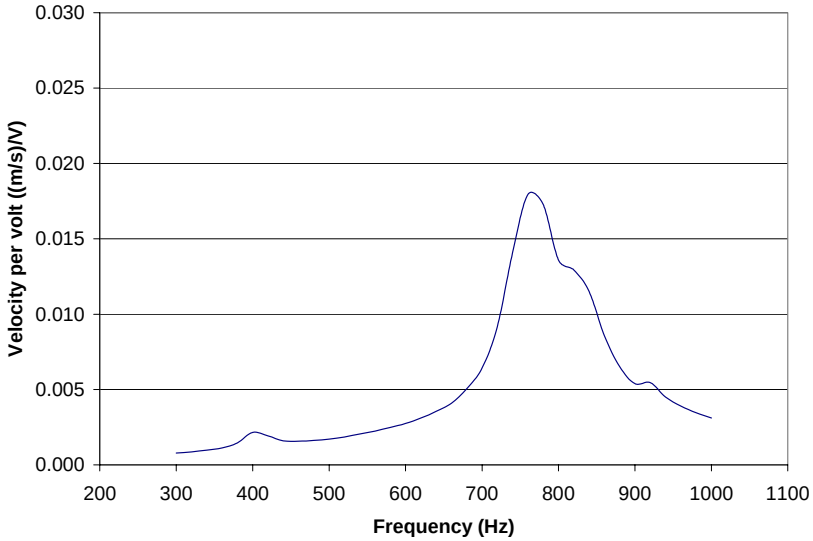

Figure 3.7: Maximum velocity per volt as a function of frequency

A graph of the maximum displacement per volt as a function of frequency is shown in Figure 3.8. The displacement at a specific frequency is determined by multiplying the displacement per volt by the measured driver voltage.

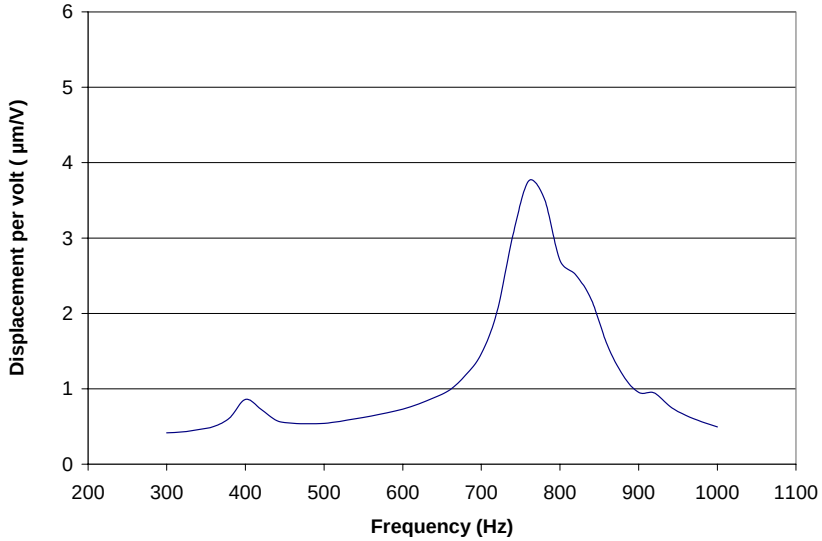

Figure 3.8: Maximum displacement per volt as a function of frequency

A graph of the maximum acceleration per volt as a function of frequency is shown in Figure 3.9. The acceleration at a specific frequency is determined by multiplying the acceleration per volt by the measured driver voltage.

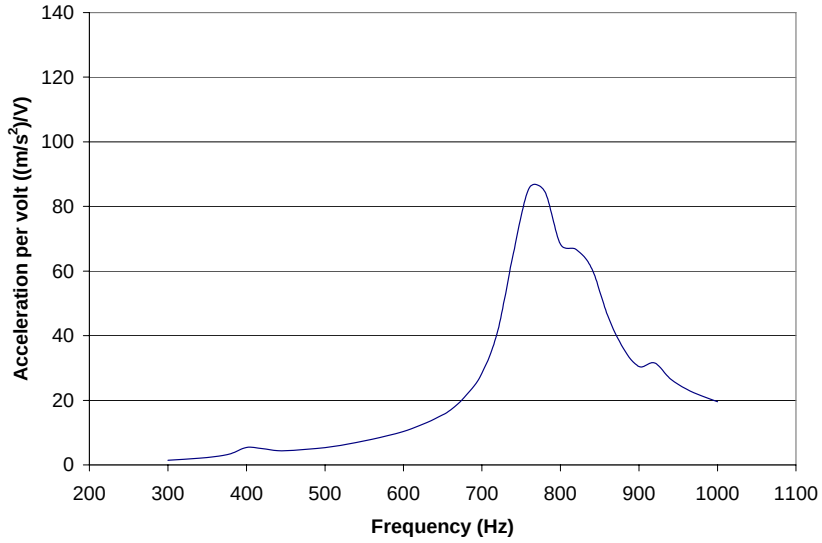

Figure 3.9: Maximum acceleration per volt as a function of frequency

The displacements and accelerations at the center of the driver were used for evaluation of the conditions necessary for droplet generation. The range of frequencies in which droplet generation was produced in this investigation was 360 to 575 Hz. From the graphs shown in Figures 3.7 to 3.9, the highest velocity per volt, displacement per volt, and acceleration per volt for the conditions tested in this investigation were 0.005 (m/s)/V, 1.18 μm/V, and 21.57 $(m/s^2)/V$.

Figures 3.10 to 3.12 are contour plots of the velocities at selected azimuthal points on the surface of the driver for different frequencies. These plots show the axisymmetry of the velocity distribution over the surface of the driver during vibration. These contour plots were made using the scanning capability of the laser vibrometer. A rectangular grid consisting of 542 points, covering the surface of the driver, was programmed to produce contour plots of the local, vertical velocity of the driver. Using the laser vibrometer, the peak velocity at each point was recorded, and the contour plots were generated. The contour plots confirmed that the maximum velocity of the driver was at its center. The velocity scales used in each of the contour plots were different, so the heights indicated in the side views cannot be compared. These plots were made at frequencies that fall within the range of frequencies in which droplet generation occurred during this investigation.

Figure 3.10: Overhead and side views of contour plot of driver velocity at 400 Hz and V_{pp1} = 15 V

Figure 3.11: Overhead and side views of contour plot of driver velocity at 400 Hz and V_{pp1} = 40 V

Figure 3.12: Overhead and side views of contour plot of driver velocity at 500 Hz and V_{pp1} = 40 V

3.3 Spray Characterization

Characterization of the sprays created by droplet generation on the surface of a liquid layer is essential for the calculation of performance of a heat transfer cell that incorporates droplet cooling. Because droplet cooling heat transfer rates are dependent upon properties of the liquid droplets, it is important that droplet sizes and flow rates are

known for each droplet generation condition. The procedures used to collect spray-characterizing data, are described in the next section.

3.3.1 Apparatus and Procedures

An enclosure to secure the driver, shown in Figure 3.13, was fabricated to maintain the depth of the driver relative to the surface of the pool, to keep the electrical terminals on the backside of the driver from coming in contact with water, and to clamp the edges of the driver in a reproducible fashion. The enclosure was fabricated from stainless steel to prevent oxidation when it was submerged in water.

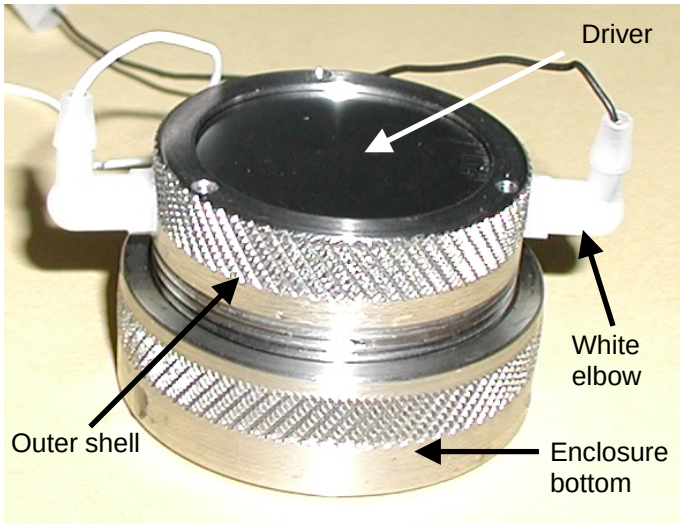

Figure 3.13: Photograph of driver secured in enclosure

The driver is secured in the enclosure by sliding it into the outer shell of the enclosure. A securing collar is then slid into the outer shell, sandwiching the driver between the collar and a lip in the outer shell. The lip and front edge of the securing collar securely clamp the outer 0.79 mm of the perimeter of the driver. The electrical leads, connected on the back of the driver, are then fed through aligned holes in the securing collar and the outer shell of the enclosure. The bottom of the enclosure is then

screwed into place and torqued to 0.56 N-m. This torque adequately secures the driver and provides a watertight seal without deforming the metal plate of the driver. The two white elbows, shown in Figure 3.13, on the perimeter of the outer shell of the enclosure are passageways that allow passage of the electrical leads through the enclosure. They protrude above the surface level of the liquid pool in which the enclosure is placed during experiments. The passageways also provide for atmospheric pressure equalization on the front and back surfaces of the driver. During Heffington's (2000) development of heat transfer cells, it was found that atmospheric pressure equalization was needed in order to reduce the influence of the closed volume that existed behind the vibrating driver. Inside a closed heat transfer cell, the pressure on the liquid side of the cell increased as droplets evaporated at the heated surface. Without equalization of the increased pressure that was caused by the evaporation of water droplets, the pressure differential on the front and back of the driver loaded the driver enough to significantly decrease its displacement.

After connecting the electrical leads to the signal generator, the driver and its enclosure were placed in a pool, which is filled with water to the prescribed level for the experiment. The liquid pool enclosure is square, was made of 6.4 mm thick Plexiglas sheets, and measures 620 x 620 x 145 mm. Placement of the driver and enclosure in the liquid pool is shown in Figure 3.14. To investigate the influence of constrained pool boundaries on droplet generation, two circular rings with inside diameters of 38.1 mm and 50.8 mm were centered over the driver to constrain the liquid pool.

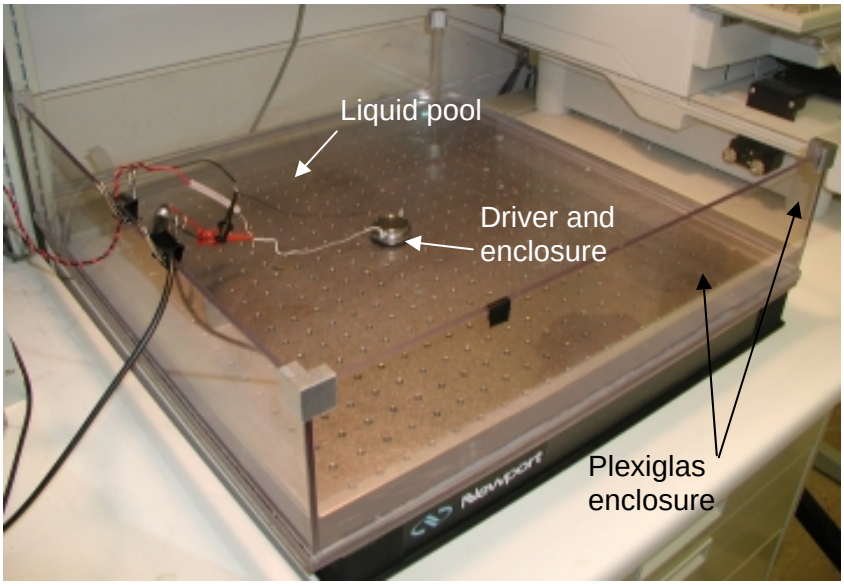

Figure 3.14: Photograph of driver in enclosure in liquid pool

3.3.1.1 Frequency Range Measurement

To determine the frequencies at which droplet generation from the liquid layer occur, the height of the pool was varied, thereby changing the thickness of the liquid layer on the driver. Based on findings by Virnig et al. (1988), it was expected that the frequencies at which droplets would be produced would vary with the liquid layer thickness and driver displacement in the present investigation. As shown in Section 3.2.2, the driver displacement is dependent on the frequency and applied voltage. Once the driver and enclosure were placed in the pool, the depth of the pool was measured and the liquid layer thickness was determined. The signal generator was then adjusted until the desired voltage was measured on the oscilloscope. The frequency of the electrical signal from the signal generator to the driver was then increased from a minimum value of 300 Hz until waves could be observed on the surface of the liquid layer. The frequency was then further slowly increased until droplets began to be ejected from the surface. The

frequency was slowly increased until droplet generation from the surface ceased. The frequency range of droplet generation was then defined by the frequencies at which droplet generation began and ended for that particular liquid layer thickness and driver voltage.

The procedure above was followed for an open pool and for pools with constrained boundaries. Constrained pools were produced by enclosing the liquid surface above the driver using PVC pipe sections. Pipe sections with inner diameters of 38.1 mm and 50.8 mm were used. The rings were centered above the driver and elevated above 88the pool bottom, allowing the water level inside the ring to remain the same as the water level in the rest of the pool.

3.3.1.2 Droplet Diameter Measurement

The diameters of the droplets ejected from the surface of the liquid layer were measured using high-speed photography. According to the results of Lang's work (1962), it was expected that the average droplet diameter would decrease as the driver frequency increased. After setting the prescribed conditions, still images of the sprays were recorded using a high-speed digital camera. The camera was positioned and its aperture was adjusted so that the depth of field included only the space bounded by the near and far edges of the driver. In Figure 3.15, is a schematic (not to scale) of the position of the camera relative to the driver, for optimum depth of field adjustment. The photographic setup was adjusted so that the depth of field included only the space above the driver, so that the droplets that were in focus in the still images were the only ones included in the size measurements. Establishment of the camera depth of field was important for this procedure, because all of the generated droplets did not travel perpendicular to the pool

surface. Figure 3.16 is an example of a digital still image that was used for droplet measurement. If the depth of field had encompassed a larger area, droplets moving toward or away from the camera would appear larger or smaller than they actually appear in the digital image.

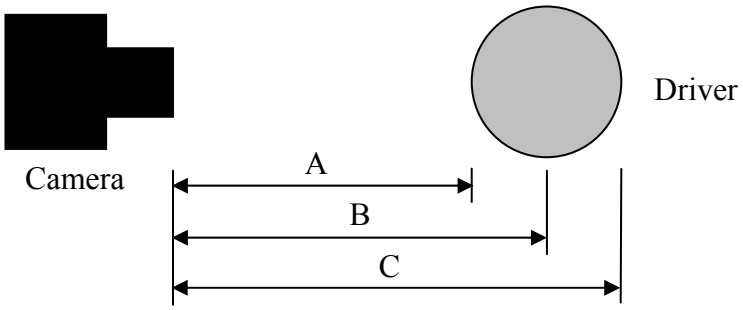

Figure 3.15: Schematic of overhead view of photographic setup for depth of field, A-near distance, B-focus distance, C-far distance

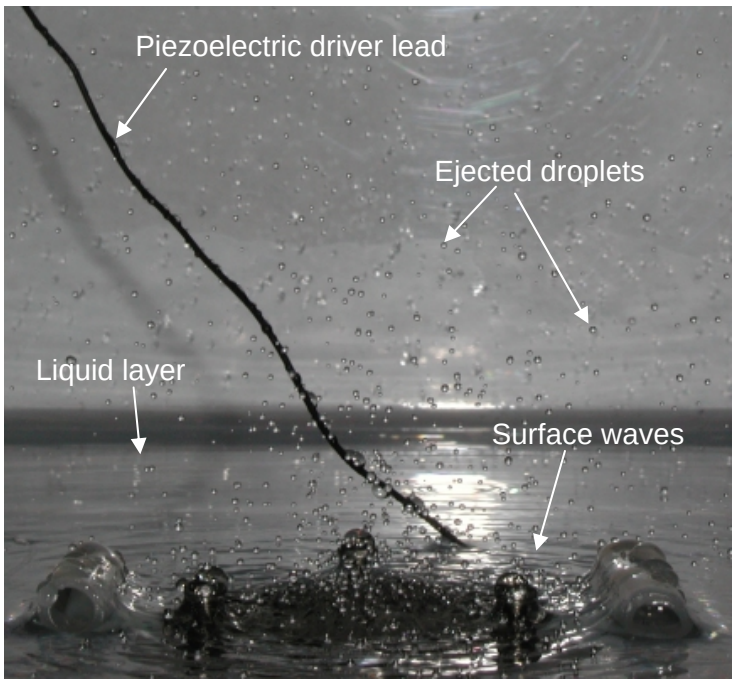

Figure 3.16: Photograph of spray generated at 500 Hz from 2.4 mm liquid layer

To calculate the diameters of the droplets from the still images, aluminum cylinders were included in the field of view of the driver. The diameters of those cylinders were measured and their dimensions were recorded. Once the still images were

obtained, imaging software was used to determine the diameter of the cylinders in pixels. The cylinder diameter, measured in pixels and in millimeters, was used to calculate a ratio of pixels per millimeter. The resulting ratio was used to convert the diameters of the in-focus droplets from pixels to millimeters. In-focus droplets were determined by visual inspection of the droplets in the digital image. All in-focus droplets were measured to determine the average droplet diameter. The number of droplets in each digital image ranged from 50 to 200, depending on the test conditions. The aluminum cylinders were recorded in each still image so that conversion ratios were calculated for each image. Because the position of the camera was the same for each recorded experiment, the ratio calculated for each digital image and used to determine the sizes of individual droplets was 17 pixels per millimeter.

3.3.1.3 Droplet Flow Rate Measurement

Measurements of droplet mass flow rates were determined as a function of height above the liquid layer using a vertical stage onto which an open-cell sponge was attached. The sponge was circular in cross-section with a 69.2 mm diameter, resulting in an interception area of 37.61 cm^2. The interception area of the sponge was large and absorbent enough so that all droplets ejected to the height of the sponge were absorbed. The stage, shown in Figure 3.17, was adjusted to prescribed heights above the driver so that it intercepted droplets as they were ejected from the liquid surface. The resolution for adjustment of the vertical position of the sponge was 0.79 mm per revolution of the crank handle.

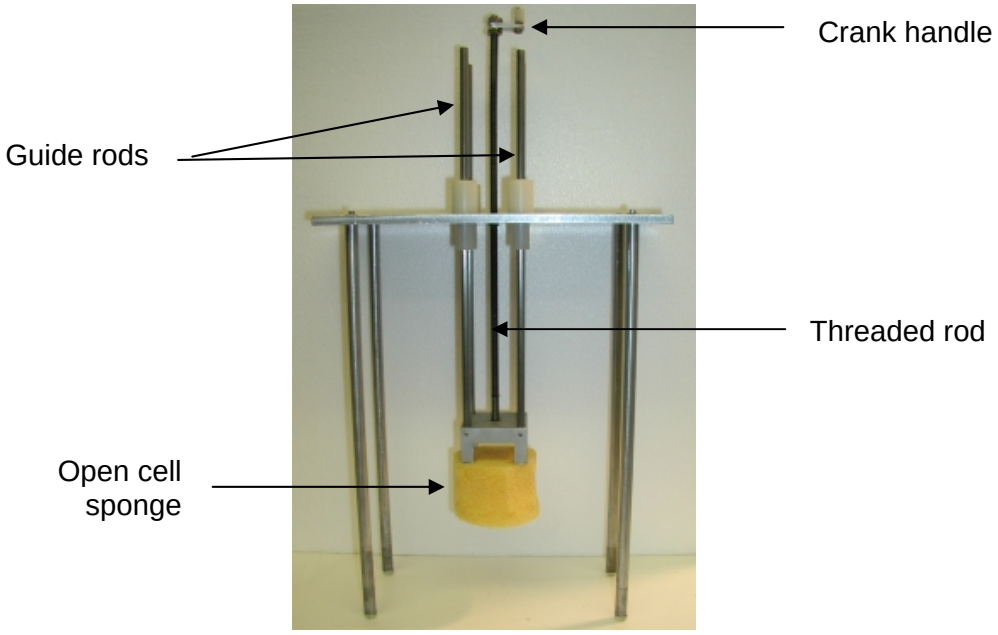

Figure 3.17: Photograph of vertical stage and open-cell sponge

The first step in determining the flow rate of droplets was to measure the initial mass of the sponge. The vertical stage and sponge were then placed over the driver, and the signal generator was activated for a prescribed duration of 5 to 15 seconds depending on the droplet generation strength. Shorter durations were used for high atomization rates and longer durations for lower atomization rates. The sponge was then removed from the pool and its mass was measured. The mass flow rate was calculated by dividing the change in mass of the sponge by the duration of the test. Finally, the average droplet diameter, measured in the digital image for the same droplet generation condition, was used to calculate the droplet flow rate.

3.3.2 Results

For the open and constrained pools, as the liquid layer thickness was increased, the frequencies at which droplet generation occurred decreased. In addition, the range of frequencies at which droplet generation occurred decreased as the liquid layer thickness

increased. These results indicated that not only was there a dependence of droplet generation on the frequency of driver vibration, but also a dependence on the thickness of the liquid layer. Additionally, in this investigation the generation of droplets was dependent on the driver voltage, due to the dependence of the driver displacement and acceleration on voltage. A dependence of wave amplitude on liquid layer thickness was indicated in the results of Virnig et al.'s work in 1988. For the frequency range that Virnig et al. investigated (2.5 to 5 Hz), they observed that for constant liquid layer thickness and excitation amplitude that the wave amplitude decreased as the driver frequency increased. The wave amplitude was not measured in the present investigation, however because droplets are ejected from the wave crests, Virnig et al.'s results indicated that droplet generation would be indirectly affected. For the frequencies used in the present investigation (360 to 575 Hz), the frequency range in which droplet generation occurred decreased as liquid layer thickness increased as shown in Figures 3.18 and 3.21.

3.3.2.1 Open Pool Frequency Ranges

A graph of the maximum and minimum frequencies at which droplet generation occurred as a function of liquid layer thickness, in an open pool for a constant driver voltage of 50 V is shown in Figure 3.18.

Figure 3.19 includes points that indicate the conditions that existed for maximum droplet generation that lie between the upper and lower bounds of the frequency range for droplet generation. Determination of maximum droplet generation was made by observation of the droplet ejection density as droplet generation varied with driver frequency.

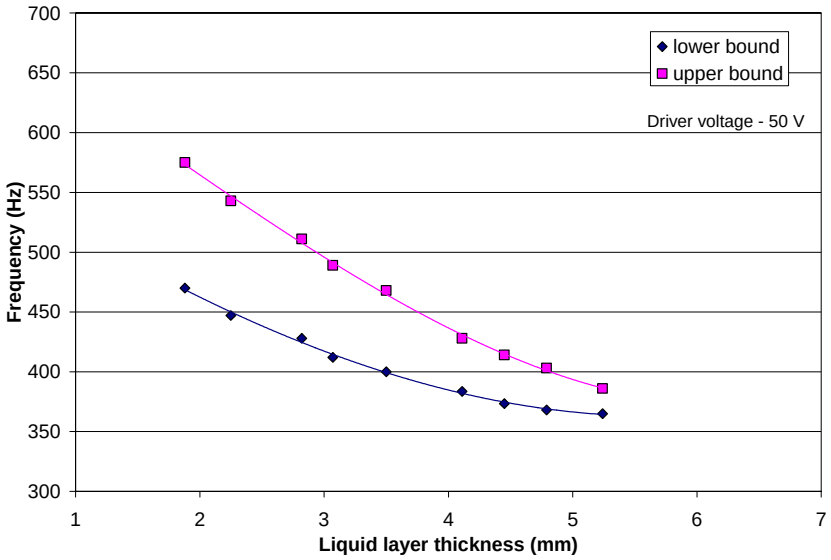

Figure 3.18: Droplet generation frequency range as a function of liquid layer thickness in an open pool

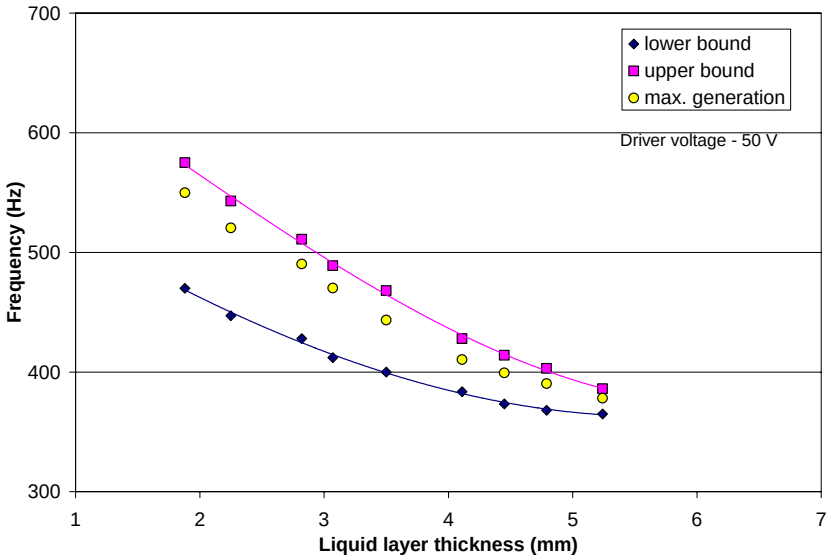

Figure 3.19: Droplet generation frequency range as a function of liquid layer thickness in an open pool, with indicated maximum generation frequencies

The lower bound data points indicate the lowest frequencies at which droplet generation occurred. The upper bound data points indicate the highest frequencies at which droplet generation occurred. Determination of the bounding frequencies was made

based on the observation of constant droplet generation from the standing waves on the liquid surface.

The upper and lower droplet generation frequency bounds are explained in consideration of findings made by Lierke et al. (1967) and Rozenberg (1973). Before droplets are generated, capillary waves must be present on the liquid surface. As shown by Lierke et al., there is a minimum vibration amplitude that must be present for the initiation of waves on a liquid surface. The relationship between this critical amplitude for wave formation and the vibration frequency is given in Equation 3.16.

$$d_c = 2\frac{\mu}{\rho}\left(\frac{\rho}{f\pi\sigma}\right)^{1/3} \qquad 3.16$$

In the same study, Lierke et al. also determined that the droplet generation inception amplitude was 3 to 6 times the critical amplitude for wave formation. In Figure 3.20, is a graph of the ratio of maximum driver displacement to critical amplitude for wave formation as a function of driving frequency in water. The driver displacement was the maximum driver displacement for a driver voltage of 50 V for the range of frequencies in which droplet generation was produced in this study. The critical amplitude for wave formation was calculated using Equation 3.16 for water at ambient pressure and temperature. As is shown, the critical amplitude for wave formation is inversely proportional to the cube root of frequency of vibration. Within the frequency range for which droplets were generated in this investigation, the maximum displacement of the driver ranged from approximately 5 to 10 times the critical amplitude for wave formation on the liquid layer. The results were in agreement with the findings of Sorokin (1957) and Eisenmenger (1959) who found that the amplitude required for droplet ejection was 4 to 8 times the amplitude required for the generation of surface waves.

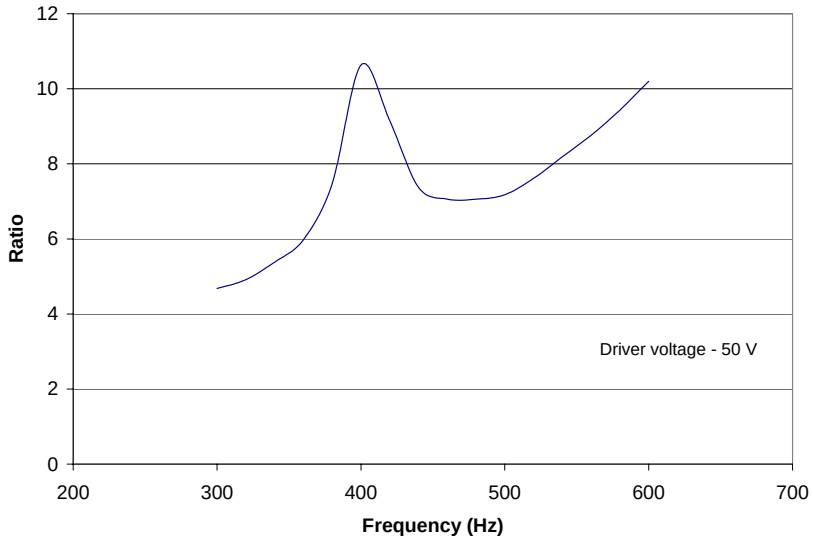

Figure 3.20: Ratio of maximum driver displacement to critical amplitude for wave formation as function of frequency in water

During droplet generation, as the driver displacement increases, the amplitude of the excited surface capillary waves eventually reaches a maximum limiting value at which the capillary wave motion becomes stable and periodic (Rozenberg, 1973). When the wave motion stabilizes, droplet generation ceases, which is due to the surface tension of the liquid. In an open pool, for each liquid layer thickness, the upper bound frequency for droplet generation corresponds to a condition at which the liquid surface waves become stable and periodic due to the surface tension forces acting on them.

As the driver frequency is increased, the surface wave wavelength and average droplet diameter produced at that frequency decrease. When producing droplets with smaller diameters, more force is required to overcome the increasing liquid surface tension that acts to keep the droplet part of the liquid layer. Droplet generation ceases when the volume of liquid at the crest of the wave lacks the required energy to overcome the surface tension exerted on it by the rest of the liquid.

3.3.2.2 Constrained Pool Frequency Ranges

The effect of constraining the liquid layer surface within the 38.1 mm ring was to decrease the highest frequencies at which droplet generation occurred, also decreasing the frequency range in which droplet generation occurred. There was no significant difference between the frequency ranges measured in the open pool and those measured in the pool constrained by the 50.8 mm ring. A graph of the maximum and minimum frequencies at which droplet generation occurred as a function of liquid layer thickness, using the 38.1 mm ring, for a constant driver voltage of 50 V is shown in Figure 3.21.

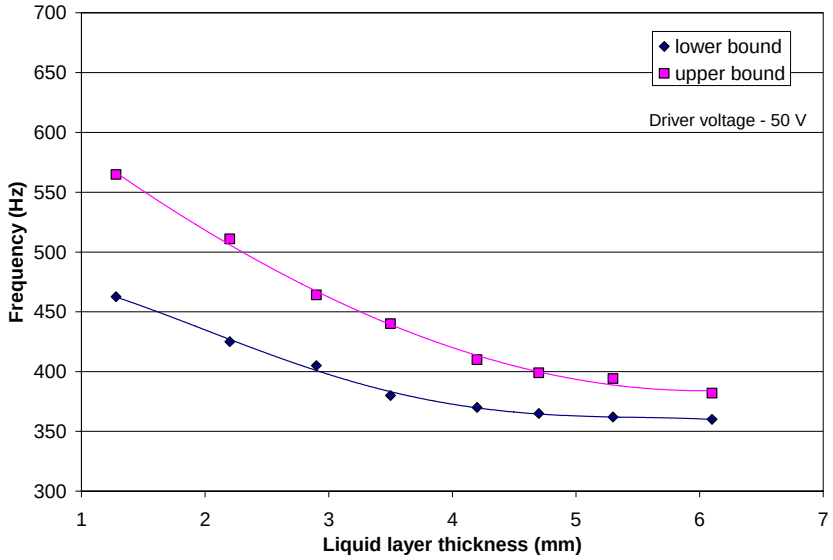

Figure 3.21: Droplet generation frequency range as a function of liquid layer thickness in a 38.1 mm constrained pool

As surface waves were produced by the vibrating driver, they traveled away from the driver. In an open pool, the waves disperse radially and are attenuated by the dissipative process of viscous shear. The pool boundaries are far enough from the driver that the wave energy reflected back toward the driver, by the pool boundaries, is

negligible. Thus, there is no influence of the pool boundaries on droplet generation in an open pool.

When using the 38.1 mm ring, the pool boundary was spaced 3.97 mm from the edge of the driver, and surface waves were reflected back toward the driver. When the dispersing surface waves and the reflected surface waves meet, and are of similar magnitude, they interact to form standing waves (Hughes et al., 1999). Combined with Rozenberg's assertion that capillary wave motion stabilizes at some maximum limiting amplitude, the standing waves produced by the interaction of dispersing and reflecting waves assist in stabilization of surface waves, causing droplet generation to cease. In the 38.1 mm constrained pool, the upper bound frequency is due to wave stabilization caused by surface tension and reflection of surface waves from the solid boundary back toward the driver. The effect of the 38.1 mm constrained boundary was to decrease the upper bound frequency for droplet generation.

When using the 50.8 mm ring to constrain the pool, the pool boundary was spaced 10.32 mm from the edge of the driver. Similar to the case of using the 38.1 mm ring, when using the 50.8 mm ring, the surface waves were reflected from the ring back toward the driver. Due to the dissipation of wave energy by viscous shear, the reflected surface waves do not interact with the dispersing waves from the driver to produce standing waves. Thus, the effect of the reflected waves on wave motion and droplet generation is negligible, and stabilization of the waves is primarily due to the surface tension force acting on them. Consequently, the frequency range in which droplet generation occurred when using the 50.8 mm ring was the same as for the open pool.

3.3.2.3 Average Droplet Diameters

Average droplet diameters, measured from the photographic images, are reported in Table 3.3, and displayed in Figure 3.22 with average droplet diameters calculated using Equation 3.17. The resulting average droplet diameters were approximately the same for the open and constrained pools (38.1 mm and 50.8 mm). Because the droplets are ejected from the crests of surface waves, which are dependent on driver frequency, the results were expected. At higher frequencies, the average diameters of generated droplets follow a decreasing trend with increasing frequency of vibration as developed by Lang (1962), which relates the average diameter of droplets generated from capillary waves to liquid properties and driving frequency. Lang developed this equation, following work done by Rayleigh (1896) in which he determined a relationship between capillary wavelength and forcing frequency.

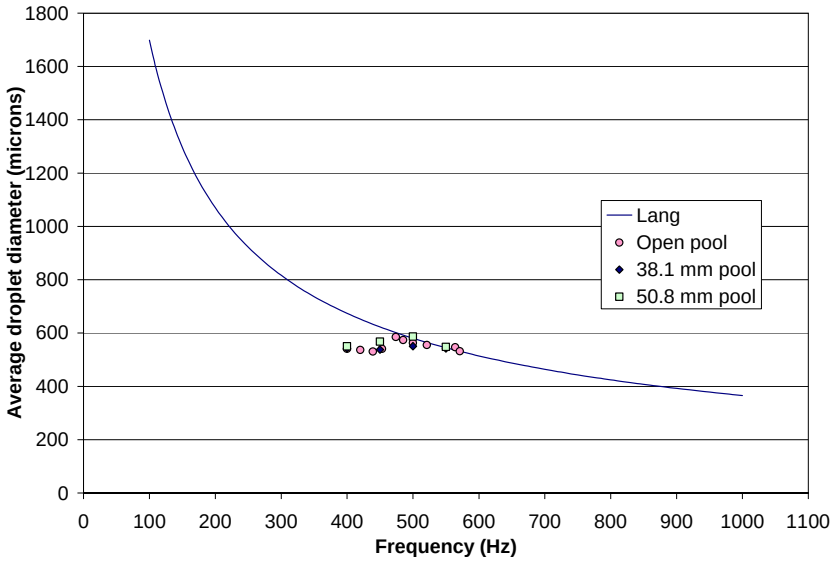

Figure 3.22: Average droplet diameter (D_b) as a function of frequency in water, from Table 3.3 and Equation 3.17

$$D_b = 0.34\lambda = 0.34\left(\frac{8\pi\sigma}{f^2\rho}\right)^{1/3} \quad 3.17$$

According to Equation 3.17, developed by Lang, the average droplet diameter should steadily decrease with increasing driver frequency. Accordingly, for the range of frequencies reported in Table 3.3, the average droplet diameter predicted using Equation 3.17 should have ranged from 674 to 533 μm. The average droplet diameter measured in this study ranged from 587 to 532 μm. Droplets generated at frequencies below 460 Hz did not follow the trend as shown in Figure 3.22. Results show that droplets generated at frequencies above 460 Hz follow the trend predicted using Equation 3.17. Departure of the average droplet diameters from the predicted trend may be due to limits on the applicability the equation at such low frequencies. Lang et al. developed Equation 3.17 from experiments conducted at frequencies of 10 kHz to 800 kHz. Its applicability to frequencies as low as those used in this research has not been previously proven.

Table 3.3: Measured average droplet diameters

Driver frequency (Hz)	**Average droplet diameter (μm)**	**Smallest droplet diameter (μm)**	**Largest droplet diameter (μm)**	**Pool boundary constraint**
400	541	472	825	Open
420	537	530	825	Open
439	531	347	694	Open
453	541	295	766	Open
474	585	353	707	Open
485	574	413	707	Open
500	563	353	707	Open
521	555	413	648	Open
564	547	353	825	Open
571	532	289	694	Open
400	543	455	793	38.1 mm
450	538	322	682	38.1 mm
500	551	347	697	38.1 mm
550	542	307	701	38.1 mm

Table 3.3 continued

400	534	467	807	50.8 mm
450	543	341	741	50.8 mm
500	560	402	684	50.8 mm
550	548	325	783	50.8 mm

3.3.2.4 Droplet Mass Flow Rates

Droplet mass flow rates were dependent on the driver frequency, driver voltage, liquid layer thickness, and interception distance above the liquid layer surface. In Figure 3.23, is a graph of the measured droplet mass flow rate as a function of driver frequency in an open pool. During the experiments, the driver voltage was held constant at 50 V, which dictated the driver displacement and acceleration, and the mass flow rates were measured at three interception distances for five liquid layer thicknesses. The interception distance above the liquid layer surface was varied by changing the position of the sponge, relative to the liquid layer surface.

As the liquid layer thickness decreases, the driver frequency must be increased to sustain droplet generation, and droplet mass flow rate increases. The driver displacement is not constant because it is dependent on the driver voltage and frequency. The frequency dependence of the driver displacement is shown in Figure 3.8. The droplet mass flow rates measured for five liquid layer thicknesses, t, are shown in Figure 3.23. It is shown that the flow rate increases as the interception distance is decreased. For each liquid layer thickness, the droplet mass flow rate was measured at three interception distances, and at multiple frequencies.

The difference between the droplet mass flow rates at the interception distances of 42 mm and 22 mm is greater than the difference between the droplet mass flow rates at

the interception distances of 62 mm to 42 mm. In Figure 3.23, are the droplet mass flow rates measured for five liquid layer thicknesses. As shown in Figure 3.18, droplet generation occurs within an indicated frequency range for a given liquid layer thickness. For each liquid layer thickness shown (2.03, 2.48, 2.87, 3.61, and 4.51 mm), droplet mass flow rates were measured at distances of 62 mm, 42 mm, and 22 mm from the liquid surface. Thus, in Figure 3.23, the symbols beneath each designated liquid layer thickness represent the droplet mass flow rates measured at each interception distance. Gaps exist between the sets of mass flow rate data for each liquid layer thickness because the flow rates were measured only for portions of the full frequency ranges in which droplet generation occurred. For example, the frequency range in which droplet generation occurred for the liquid layer thickness of 3.61 mm was 390 to 460 Hz, as shown in Figure 3.18. The droplet mass flow rates for the same liquid layer thickness were only measured in the range of 400 to 425 Hz. Measurement of droplet mass flow rates over the full frequency range for each liquid layer thickness was not made because near the boundaries of the frequency range in which droplet generation occurred, the number of and ejection heights of generated droplets were too low to be measured using the apparatus depicted in Figure 3.17.

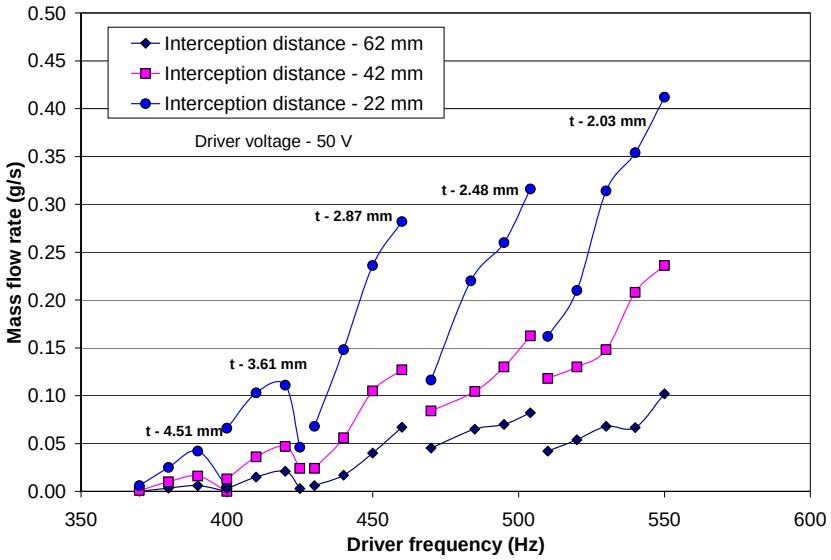

Figure 3.23: Droplet mass flow rate as a function of driver frequency for constant driver voltage and liquid layer thickness, t, in an open pool

Because not all of the generated droplets travel the same distance from the liquid layer surface, the measured mass flow rates decrease as the interception distance increases. The mass flow rate variation for liquid layer thicknesses of 4.51 and 3.61 mm is due to the variation in the intensity of droplet generation with frequency for each of the liquid layer thickness. A decrease in mass flow rate is not recorded for the thinner liquid layer thicknesses (2.87, 2.48, and 2.03 mm) because the drop in droplet generation was so great that the mass flow rate was not measurable, even at the shortest interception distance of 22 mm. Throughout the droplet generation frequency range, a number of combinations of liquid layer thickness, interception distance, and driver frequency can be used to produce a specified droplet mass flow rate. For instance, a droplet mass flow rate of approximately 0.10 g/s can be produced by combinations of liquid layer thickness, interception distance, and driver frequency of (3.61 mm, 22 mm, 410 Hz), (2.87 mm, 42 mm, 450 Hz), (2.48 mm, 42 mm, 485 Hz), and (2.03 mm, 62 mm, 550 Hz).

The maximum droplet mass flow rates produced when using the circular rings to enclose the pool were not significantly different from those produced in the open pool. In Figures 3.24 and 3.25, are the droplet mass flow rates measured for four liquid layer thicknesses, t, in 38.1 mm and 50.8 mm constrained pool. For each liquid layer thickness, the droplet mass flow rate was measured at three interception distances, for multiple frequencies. The 38.1 mm pool boundary had the effect of reducing the upper bound of the frequency range for droplet generation. The average droplet diameters and mass flow rates were not significantly affected, as shown in Figures 3.22 and 3.24. The constrained boundaries reflect waves back toward the driver, assisting in stabilizing the wave motion, which affects the frequency ranges for droplet generation. The average droplet diameters and mass flow rates are similar to those produced in an open pool because the pool boundaries do not affect surface wavelengths caused by the driver vibration nor the mechanisms of ejection of droplets from the wave crests.

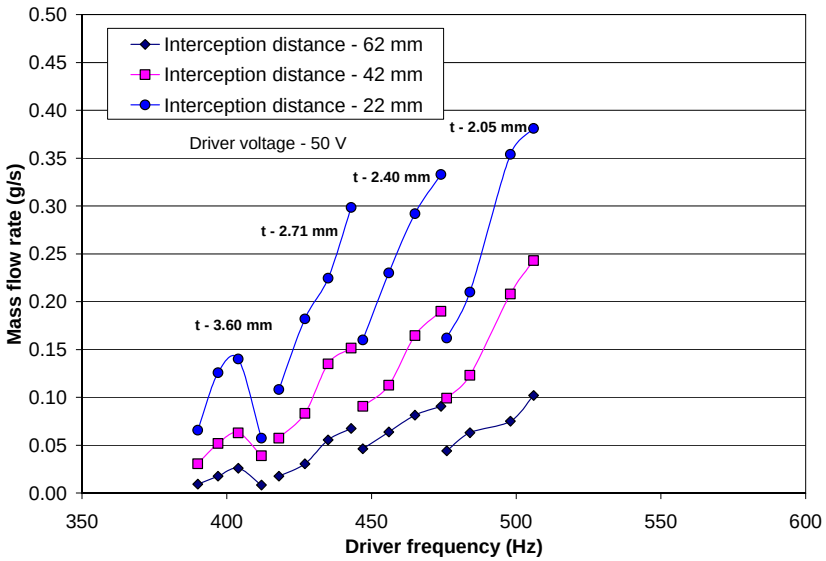

Figure 3.24: Droplet mass flow rate as a function of driver frequency for constant driver voltage and liquid layer thickness, t, in a 38.1 mm constrained pool

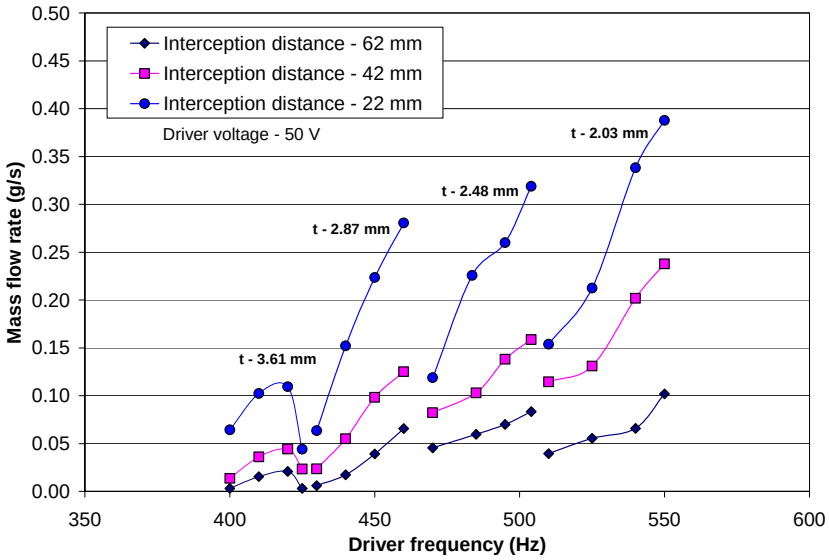

Figure 3.25: Droplet mass flow rate as a function of driver frequency for constant driver voltage and liquid layer thickness, t, in a 50.8 mm constrained pool

By application of appropriate driver frequency, driver voltage, liquid layer thickness, and interception distance, a wide range of droplet mass flow rates are possible. For a fixed driver voltage, the maximum possible droplet mass flow rate increases as the liquid layer thickness decreases. To continue generating droplets as the liquid layer thickness is decreased, the driver frequency (displacement and acceleration) must be increased. For a constant liquid layer thickness and driver frequency, the driver voltage is increased or decreased to increase or decrease droplet generation and thus the droplet mass flow rate.

Droplet mass flow rate as a function of driver frequency for multiple driver voltages in an open and a 38.1 mm constrained pool are presented in Figures 3.26 and 3.27. Results show that for a constant driver frequency and liquid layer thickness, droplet mass flow rate increases with driver voltage. This is expected since the driver displacement and acceleration increase with voltage. At the highest frequencies for which droplet generation occurs, higher driver voltages than when at the lowest

frequencies are necessary to maintain droplet generation. At frequencies near the lower bound, droplet generation can continue at lower driver voltages. These results indicate that the frequency range for which droplet generation occurs decreases as driver voltage (displacement and acceleration) decreases. Thus, the droplet generation frequency range for a constant liquid layer thickness becomes narrower as the driver displacement is decreased.

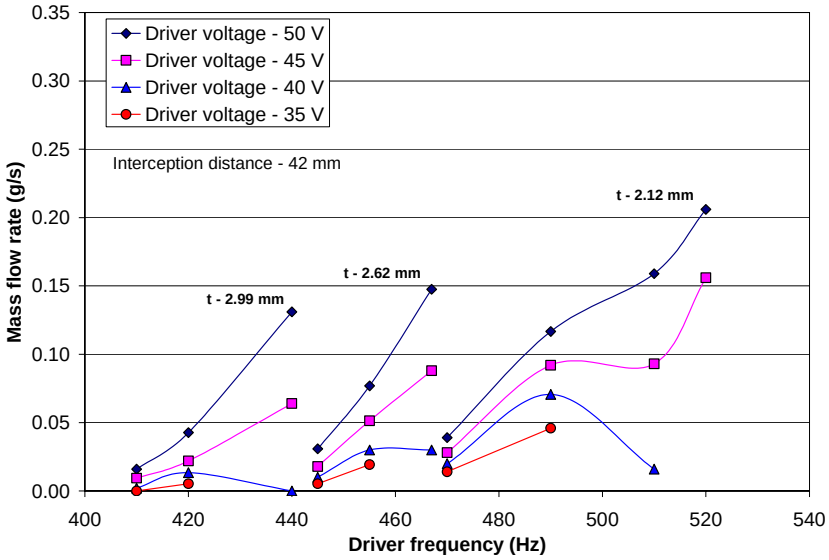

Figure 3.26: Droplet mass flow rate as a function of driver frequency for constant interception distance and liquid layer thickness, t, in an open pool

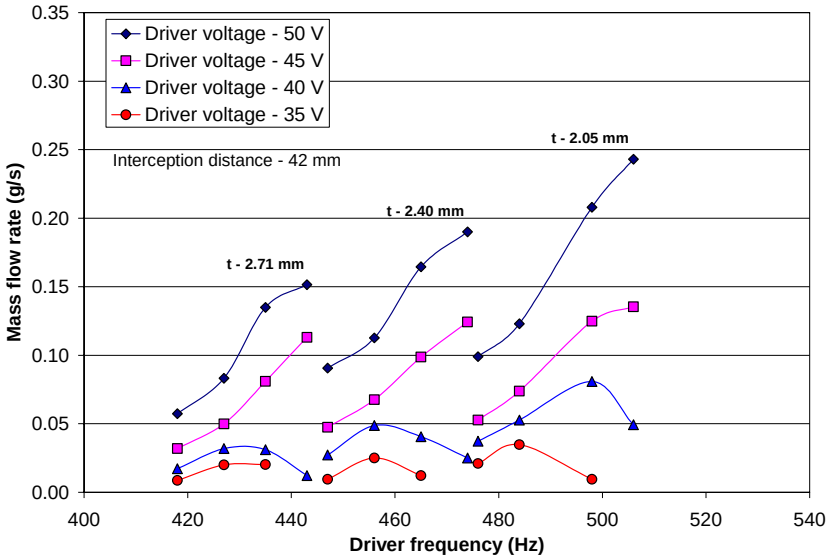

Figure 3.27: Droplet mass flow rate as a function of driver frequency for constant interception distance and liquid layer thickness, t, in a 38.1 mm constrained pool

The measured droplet mass flow rate is dependent on the liquid layer thickness, driver voltage, driver frequency, and interception distance. For constant driver voltage and frequency, the droplet mass flow rate increases as the liquid layer thickness decreases, and increases as the interception distance decreases. At a constant driver frequency, droplet generation can be varied by adjustment of the driver voltage that changes the driver's displacement. Deviation from the driver frequency at which maximum generation is produced results in a decrease in the droplet mass flow rate. In Figures 3.23 through 3.25, the droplet mass flow rate ends abruptly because when the frequency was increased, droplet production decreased to a level that it could not be measured at the prescribed interception distance. Droplets continued to be produced within the frequency ranges presented in Figures 3.18 and 3.21, but did not travel far enough from the liquid layer surface to impinge on the sponge.

3.4 Droplet Generation Analysis

Using the driver and spray characterization results from Sections 3.2 and 3.3, the following procedure was used to analyze the data. For each experimental condition at which droplet generation occurs, the following information is known from the results of the spray and driver characterizations.

- Driver frequency
- Driver voltage
- Liquid layer thickness
- Driver maximum amplitude
- Driver maximum acceleration

In addition to the parameters identified by Goodridge et al., liquid layer thickness is a parameter that was considered to influence the conditions necessary for droplet generation. Therefore, in this investigation, the parameters considered to affect droplet generation were driver frequency, driver acceleration, driver displacement, and liquid layer thickness.

Two approaches were taken in an effort to determine the functional dependencies among the acceleration necessary to generate droplets, the liquid layer thickness, and the driver frequency. Due to poor functional dependences, the results of the first approach were unsatisfactory and could not be used to determine the range of conditions that led to droplet generation. Results of the second approach were successful and yielded a dimensionless parameter that can be used to determine the range of conditions that lead to droplet generation. Results using the second approach are presented for droplet generation in the open and 38.1 mm constrained pool. Because the 50.8 mm constrained

pool did not affect the droplet generation frequency range, the results for this configuration are the same as for the open pool.

3.4.1 First Approach

Determination of the dependence of the acceleration necessary to produce droplets on frequency was determined by graphing the acceleration as a function frequency, shown in Figure 3.28, for the upper and lower bounds of the frequency range in which droplets were generated (Figure 3.18). Figure 3.29 is a graph of the acceleration as a function of liquid layer thickness for the same conditions. Both graphs are of data collected for droplet generation in an open pool for a driver voltage of 50 V.

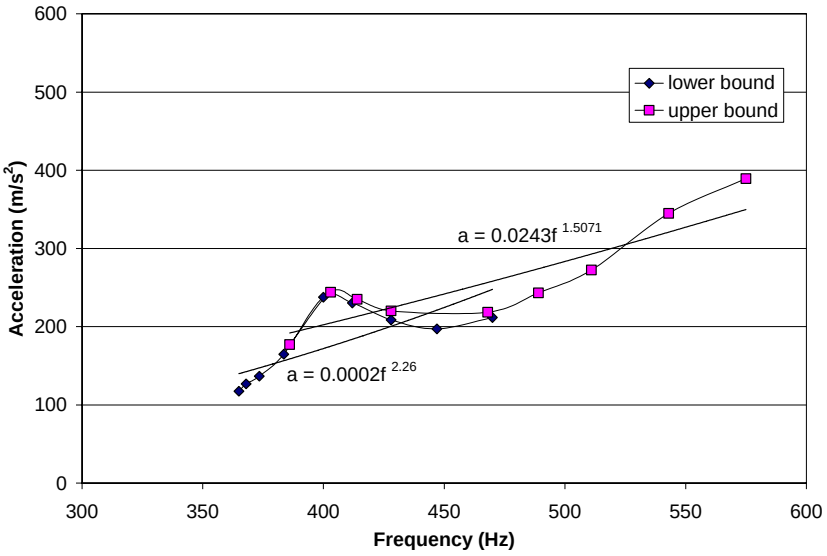

Figure 3.28: Acceleration necessary for droplet generation as a function of frequency in an open pool

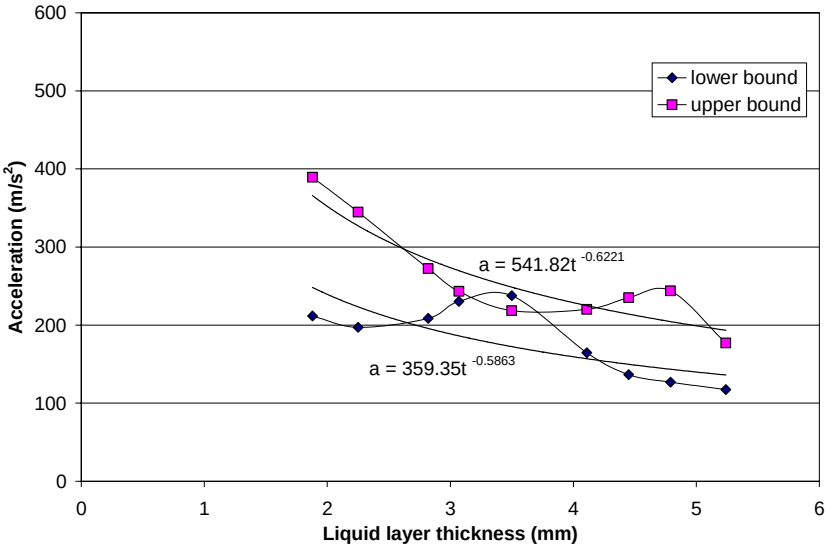

Figure 3.29: Acceleration necessary for droplet generation as a function of liquid layer thickness in an open pool

The dependence of acceleration on frequency and liquid layer thickness were determined by fitting regression lines through the upper bound and the lower bound data. As previously stated, the results of this approach were unsatisfactory due to poor functional dependences. As shown in Figure 3.29, the lines connecting the upper bound data points and lower bound data points intersect. The equations describing the regression lines are included in the figures. The values of the exponents on the dependent variables, frequency, and liquid layer thickness, in the regression equations were used to determine the relationship in Equation 3.18. The symbol a is the maximum driver acceleration, f is the driver frequency, and t is the liquid layer thickness.

$$a \sim f^{1.78} t^{-0.57} \qquad 3.18$$

A dimensionally consistent form, shown in Equation 3.19, was developed that describes the acceleration necessary for droplet generation as functions of frequency, liquid layer thickness, and liquid properties.

$$a \sim f^{16/9} t^{-2/3} (\sigma / \rho)^{1/9} \qquad 3.19$$

The values of the exponents on the dependent variables in Equation 3.18 were converted to fractions to formulate Equations 3.19 and 3.20, which are dimensionally consistent.

$$a = (318.5E^{-}6) f^{16/9} t^{-2/3} (\sigma / \rho)^{1/9} \qquad 3.20$$

Equation 3.20 was developed by fitting the form to the experimental upper and lower bound data. This equation is similar to the one developed by Goodridge et al. for low viscosity fluids, $a = 0.239\omega^{4/3}(\sigma/\rho)^{1/3}$ (Equation 3.3). The difference between Equations 3.3 and 3.20 is the inclusion of the liquid layer thickness in Equation 3.20. Liquid layer thickness was not included in Goodridge et al.'s acceleration equation because it was constant for their experiments. Because both acceleration equations must be dimensionally consistent, the exponents on the frequency and fluid properties are different in each equation. The calculated constant of Equation 3.20 is dimensionless.

Assuming water as the working fluid, the acceleration required for droplet generation can be calculated using Equations 3.3 and 3.20. Equation 3.3 (Goodridge et al.) was developed based on results of experiments in which the liquid layer thickness was constant at 10.0 cm. Calculation of the acceleration using Equation 3.20 (Pyrtle), for the common liquid layer thickness of 10.0 cm, yields considerably lower values than values calculated using Equation 3.3. At a frequency of 100 Hz, Equations 3.3 and 3.20 yield values of 53.7 m/s^2 and 1.8 m/s^2, respectively. The differences between the calculated accelerations is great because calculation of acceleration using Equation 3.20 for a liquid layer thickness of 10 cm is well above the maximum liquid layer thickness (5.24 mm) for which data was collected to develop Equation 3.20. At a frequency of 100 Hz and a liquid layer thickness of 4 mm, Equation 3.20 yields an acceleration of 15.8

m/s^2. Because Equation 3.3 was developed for the results of experiments in which the liquid layer thickness was held constant, the liquid layer thickness is not included in the equation. Due to differences in the experimental conditions of Goodridge et al. and the present investigation, the calculated droplet generation acceleration differed, as indicated by the variables in Equations 3.3 and 3.20.

Figure 3.30 is a graph of acceleration as a function of frequency for the upper and lower bounds of acceleration for droplet generation in an open pool for each liquid layer thickness. The solid markers are the same acceleration data as shown in Figure 3.28, while the open markers represent acceleration data calculated using Equation 3.20. The lines in the graph represent regression lines fit through the calculated acceleration data at the upper and lower bounds of the frequency ranges in which droplet generation occurred. The desired result was that the lines represent upper and lower bounds of acceleration necessary for droplet generation.

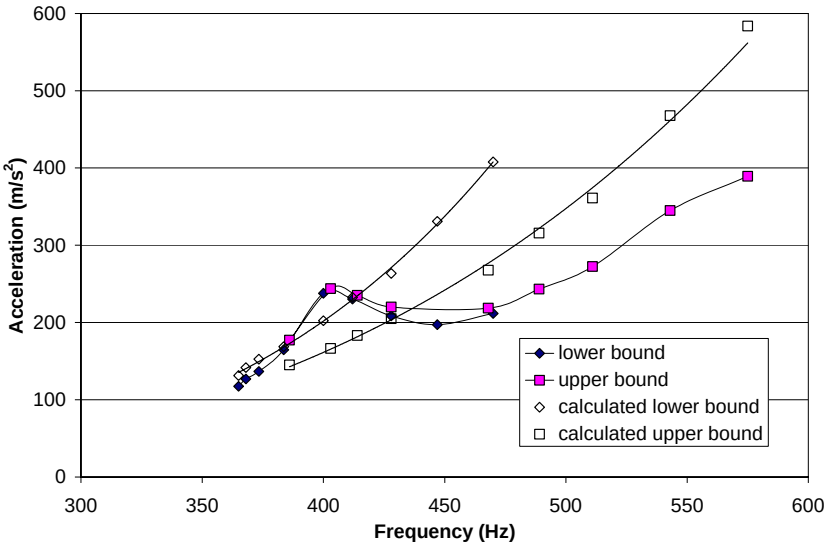

Figure 3.30: Acceleration necessary for droplet generation as a function of frequency for Equation 3.20

The results in Figure 3.30 indicate that the first approach taken to determine the bounds for the acceleration necessary for droplet generation as a function of frequency is not adequate. Due to poor functional dependence, the solid points that represent actual acceleration values in the graph do not fall on or between the lines produced using Equation 3.20. Thus, Equation 3.20 does not provide an adequate means for determination of conditions necessary for droplet generation within the observed frequency bounds. This approach resulted in an acceleration equation that was dependent on frequency and liquid layer thickness, but did not indicate boundaries for a range of conditions that lead to droplet generation. Results of the study done by Goodridge et al. were not consistent with the results of the present study. In their study, Goodridge et al. identified a frequency dependent minimum acceleration necessary for droplet generation. In the present study, droplet generation occurred for a range of combinations of acceleration, displacement, and liquid layer thickness conditions. Thus, the approach Goodridge et al. used to identify conditions necessary for droplet generation could not be used to identify droplet generation conditions for the experiments performed in the present investigation.

3.4.2 Second Approach

Another approach taken to determine the range of conditions necessary for droplet generation was based on the determination of a non-dimensionalized acceleration. Non-dimensionalization of the acceleration, with consideration of the wave behavior on the liquid free surface, proved to be the approach needed to determine conditions for droplet generation.

As previously stated, the presence of surface waves, whether they are gravity or capillary waves, is necessary for droplet generation. The speed of the wave, which is the speed of propagation of a disturbance on its surface, depends on its wave number. The wave speed is related to the wave number as

$$u_w = \frac{\omega}{k} = \sqrt{\left(\frac{g}{k} + \frac{\sigma k}{\rho}\right)\tanh(kt)} \qquad 3.21$$

$$\omega^2 = \left(gk + \frac{\sigma k^3}{\rho}\right)\tanh(kt) \qquad 3.22$$

Where u_w is the wave speed, ω is the angular frequency of the wave, k is the wave number, g is gravitation acceleration, σ is the liquid surface tension, ρ is the liquid density, and t is the liquid layer thickness. Equation 3.22, which is the dispersion equation for surface waves, was developed from potential flow theory by solving Laplace's equations with appropriate boundary conditions (Dean and Dalrymple, 1991). The equation is applicable to conditions for which the wave amplitude is small relative to the wavelength and liquid depth. It describes waves that occur on the surface, not accounting for the generation of droplets. From the crests of these surface waves, droplets are generated as part of the wave crest detaches and travels away from the liquid surface. The wave number is related to the wavelength, shown in Figure 3.31, by Equation 3.23.

$$k = \frac{2\pi}{\lambda} \qquad 3.23$$

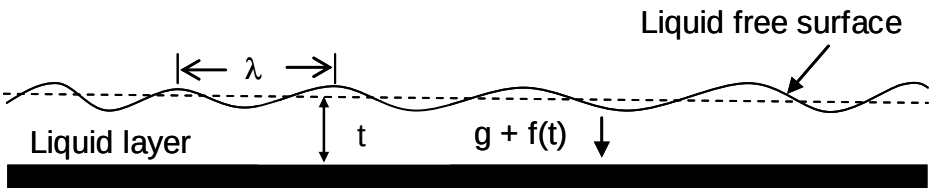

Figure 3.31: Schematic of vertically oscillating vibration of liquid layer

The wave speed was determined to be an important parameter for non-dimensionalization of the acceleration that is necessary for droplet generation. The wave speed is useful because, as shown in Equation 3.21, it embodies effects of local acceleration, changes in liquid layer depth, and wavelength; all of which vary at different droplet generation conditions. In this study, because the maximum acceleration at the center of the driver ranges from seven to fifty times the acceleration of gravity during droplet generation, the gravity term in Equation 3.22 is replaced by the driver acceleration for calculation of the wave speed. The wavelength of the generated capillary waves is calculated using the relationship developed by Rayleigh (1896), shown in Equation 3.24.

$$\lambda = \left(\frac{8\pi\sigma}{f^2 \rho} \right)^{1/3} \qquad 3.24$$

Using a linear stability analysis, James (2000) non-dimensionalized the forms of the continuity and Navier-Stokes equations that govern the flow of a vertically oscillating liquid layer, shown schematically in Figure 3.31. The following parameters resulted from the non-dimensionalization she performed, which were scaled on the liquid layer thickness and a scaling velocity.

$$\mathrm{Re} = \frac{\rho U_s t}{\mu} \tag{3.25}$$

$$We = \frac{\rho U_s^2 t}{\sigma} \tag{3.26}$$

$$Bo = \frac{gt}{U_s^2} \tag{3.27}$$

$$A = \frac{t^2 a \rho}{\sigma} \tag{3.28}$$

$$\Omega = \frac{t\omega}{U_s} \tag{3.29}$$

These dimensionless parameters are Reynolds number (Re), Weber number (*We*), Bond number (*Bo*), dimensionless amplitude (*A*), and dimensionless frequency (Ω). The symbol *t* represents the liquid thickness depicted in Figure 3.31, and U_s is a scaling velocity. The Reynolds number is the ratio of the inertial to viscous forces of the liquid. The Weber number is a ratio of the inertial and surface tension forces of the liquid. The Bond number is a ratio of gravitational and inertial forces of the liquid, which is the reciprocal of the Froude number. The Froude number is an important dimensionless parameter for use in this study because it is the ratio of the inertial force on an element of liquid to the weight of that element.

The acceleration necessary for droplet generation is non-dimensionalized as shown in Equation 3.30, where *a** is the dimensionless acceleration, *a* is the driver acceleration, *t* is the liquid layer thickness, *f* is the driver frequency, and *d* is the driver displacement.

$$a^* = \frac{at}{(fd)^2} \tag{3.30}$$

The resulting graph of dimensionless acceleration as a function of frequency is shown in Figure 3.32. The graphed experimental data points, now in dimensionless form, provide marginally better clarity of the upper and lower bounds of the frequency range necessary for droplet generation, compared to when the acceleration was plotted in dimensional form in Figure 3.29. The bounds correspond to the conditions present at the upper and lower boundary frequencies at which droplet generation occurred for the liquid layer thicknesses in an open pool. However, there is still considerable scatter in the bounding data points, which should represent distinct droplet generation boundaries. The regression lines that represent the upper and lower bounds for the conditions necessary for droplet generation poorly fit the data points.

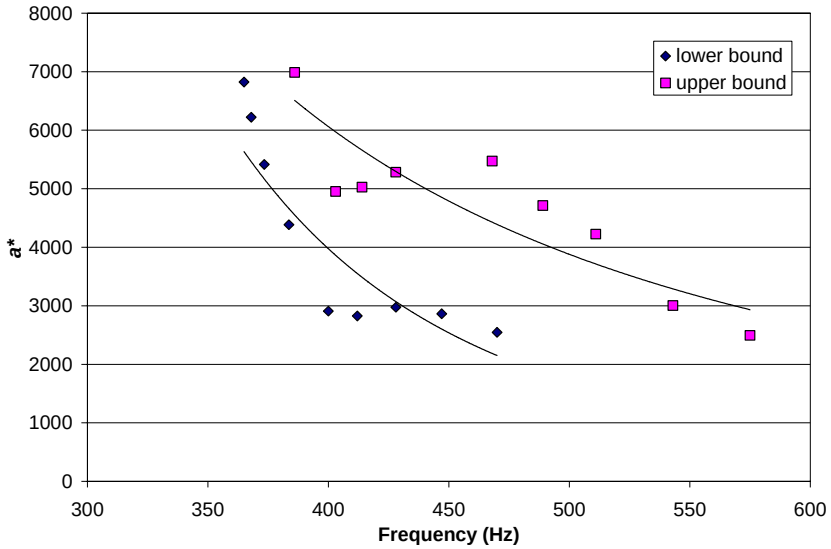

Figure 3.32: Dimensionless acceleration (a^*) as a function of frequency in an open pool

In its present form, the dimensionless acceleration does not embody the effects of changes in the Froude number, defined as the ratio of acceleration and inertial forces. In this investigation, *Fr* is defined using the calculated wave speed, the acceleration of the driver, and the liquid layer thickness. The acceleration and inertial forces are caused by

the local acceleration provided by the driver and the generation of waves on the liquid surface. In Equation 3.31, the dimensionless acceleration is redefined so that it includes the ratio of those forces through the Froude number.

$$a^{**} = \frac{at}{(fd)^2 Fr} \tag{3.31}$$

where

$$Fr = \frac{u_w^2}{at} \tag{3.32}$$

Thus the dimensionless acceleration becomes

$$a^{**} = \left(\frac{at}{fdu_w} \right)^2 \tag{3.33}$$

a^{**} is a new dimensionless parameter, developed in this investigation. It is a ratio of the vibrating driver's force to the inertial force of the surface capillary waves. Figure 3.33 is a graph of the redefined dimensionless acceleration, a^{**}, as a function of frequency for the same experimental data graphed in Figures 3.30 and 3.32. These results more clearly define the bounds of dimensionless acceleration as a function of frequency that are necessary for droplet generation from the liquid surface. The power regression lines that are drawn through the dimensionless acceleration points represent the conditions at the upper and lower boundaries of the frequency ranges for which droplet generation occurs. Figure 3.34 includes dimensionless acceleration values calculated for data collected at intermediate frequencies between the upper and lower bounds in which droplet generation occurred.

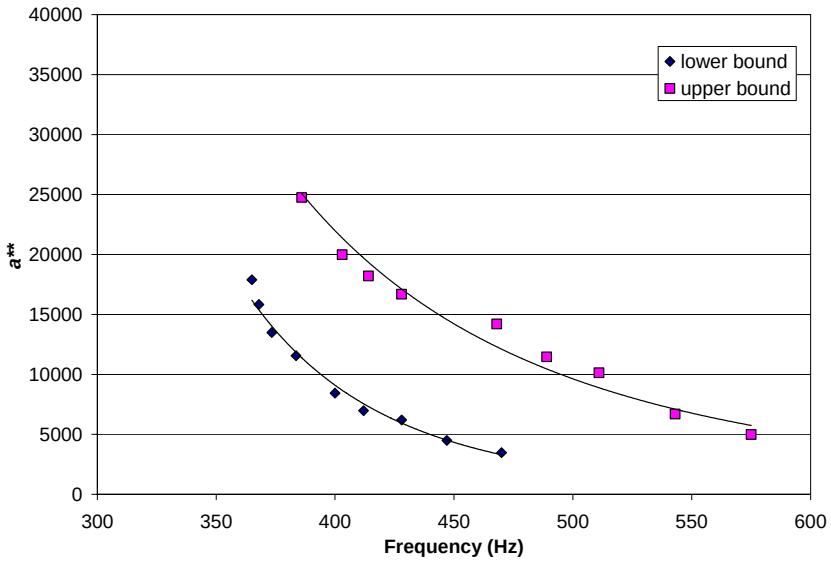

Figure 3.33: Bounds of dimensionless acceleration (a^{**}) as a function of frequency in an open pool

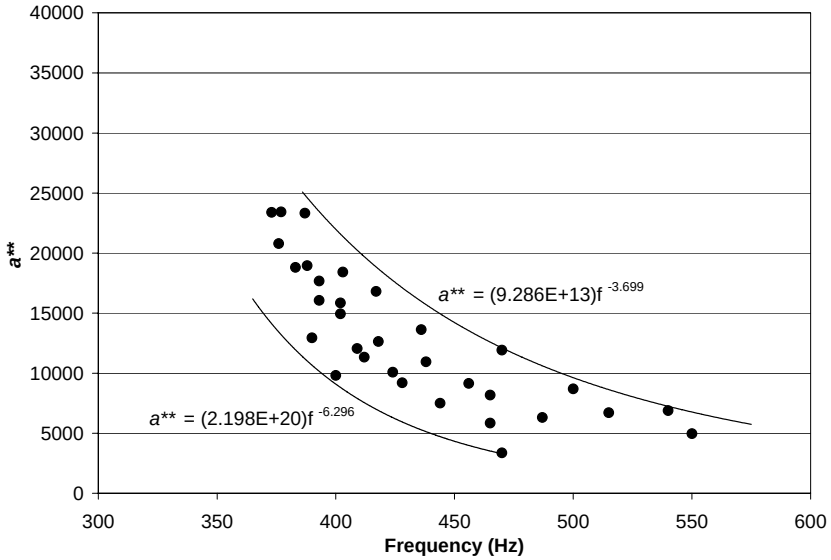

Figure 3.34: Dimensionless acceleration (a^{**}) as a function of frequency at intermediate frequencies in an open pool

The dimensionless acceleration data graphed in Figure 3.34 represent the range of conditions for which droplet generation occurs in an open pool, using the driver described and characterized in Section 3.2. The data points are dimensionless acceleration values calculated for droplet generation that occurred within the frequency range defined by the

upper and lower frequency bounds. Using the power regression curves that were drawn through the data points that represent the upper and lower bounds for droplet generation at a driver voltage of 50 V, Equations 3.34 and 3.35 can be used to determine conditions necessary for droplet generation. At lower driving voltages, the displacement and acceleration of the driver are smaller, decreasing the magnitude of a^{**}. For droplet generation at a constant driver frequency and liquid layer thickness, the driver voltage can be varied as long as a^{**} is within the bounds indicated in Figure 3.33.

Calculated dimensionless acceleration values that lie between the upper and lower bounds, shown in Figure 3.33, indicate conditions at which droplet generation occurs in an open pool. Equations 3.34 and 3.35 respectively represent the lower and upper bounds determined for water in an open pool and for a 50.8 mm constrained pool. The liquid layer thicknesses for which the equations were developed were from 1.88 to 5.24 mm. The piezoelectric driver was 31.75 mm in diameter and 0.10 mm thick.

$$a^{**} = 2.198 \times 10^{20} f^{-6.296} \qquad 3.34$$

$$a^{**} = 9.286 \times 10^{13} f^{-3.699} \qquad 3.35$$

The dimensionless acceleration, a^{**}, is defined in Equation 3.33, and the frequency of the driver is measured in units of Hz.

The dimensionless acceleration, a^{**}, results for the 38.1 mm constrained pool are presented in Figure 3.35. The upper and lower bounds that are defined by the dimensionless acceleration values are different from the results for the open pool. The difference is due to the difference in the droplet generation frequency ranges, shown in Figures 3.18 and 3.21.

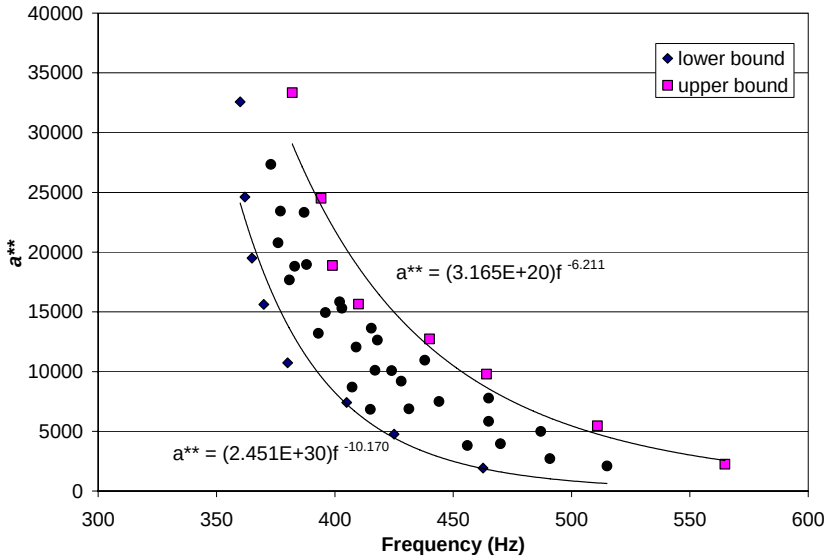

Figure 3.35: Bounds of dimensionless acceleration (a^{**}) as a function of frequency in a 38.1 mm constrained pool

Calculated dimensionless acceleration values that lie between the upper and lower bounds, shown in Figure 3.35, represent conditions at which droplet generation occurred in a 38.1 mm constrained pool. Equations 3.36 and 3.37 respectively represent the lower and upper bounds determined for a 38.1 mm constrained pool of water for liquid layer thicknesses between 1.28 and 6.1 mm. The same piezoelectric driver as was used in the open pool was used for the constrained pool.

$$a^{**} = 2.451 \times 10^{30} f^{-10.170} \qquad 3.36$$

$$a^{**} = 3.165 \times 10^{20} f^{-6.211} \qquad 3.37$$

Equation 3.33 was used to calculate the dimensionless acceleration values for all data points presented in Figures 3.34 and 3.35. Power regressions were then calculated for the upper boundary data points and the lower boundary data points. Those regressions were defined by Equations 3.34 and 3.35, and Equations 3.36 and 3.37. Equations 3.34 and 3.35 define the lower and upper bounds of droplet generation

conditions in an open pool. Equations 3.36 and 3.37 define the lower and upper bounds of droplet generation conditions in a 38.1 mm constrained pool. The differences between the pairs of equations exist due to the differences in the frequency ranges in which droplet generation occurred, shown in Figures 3.18 and 3.21. The differences in the slopes of the upper and lower bounds indicated different frequency-liquid layer thickness relationships. Consequently, those differences resulted in variation of the frequency dependent dimensionless acceleration equations that define the droplet generation boundaries.

Results show that the dimensionless acceleration can be calculated to define the upper and lower boundaries for the range of conditions in which droplet generation occurs in an open and in a constrained pool. Combinations of liquid layer thickness and driver frequency, displacement, and acceleration can be used to calculate dimensionless acceleration values. Those values that lie between the lower and upper bounds, indicated in Equations 3.34 and 3.35 for the open pool and in Equations 3.36 and 3.37 for the 38.1 mm constrained pool, represent conditions for which droplet generation occurs. Using the driver characterization, the appropriate driver frequency and voltage can be selected to produce the desired displacement and acceleration needed to generate droplets from a specific liquid layer thickness.

CHAPTER 4

HEAT TRANSFER CELL MODEL

4.1 Formulation

The purpose for formulating the heat transfer model was to predict the performance of a heat transfer cell that used droplet cooling as a means for heat dissipation. Using the results presented in the previous chapter, a steady state model was used to estimate heat transfer performance, assuming that droplet generation could be achieved inside a closed heat transfer cell. The experimental data that were described for the 38.1 mm constrained pool were used in the heat transfer model. These data include the droplet mass flow rate and droplet generation as functions of driver voltage and frequency. The results from the 38.1 mm constrained pool were chosen instead of the results from the open pool because the constrained pool better represents the physical configuration of the heat transfer cell.

The model is an analytical one that is formulated to simulate heat transfer in a heat transfer cell in which droplets are generated from a liquid layer by a driver mounted in the bottom of the cell. A schematic of the modeled heat transfer cell is shown in Figure 4.1. The cell is a closed system so that no mass leaves the cell and only heat passes through its boundaries. As droplets are generated from the liquid layer in the bottom of the cell, they travel upward toward the top of the cell where the heat source is attached. The droplets impinge on the inner surface of the top of the cell. As the droplets evaporate on the hot surface, heat is removed from the heat source. The resulting

vaporized water then condenses on the inside perimeter surface of the cell. At the cooler surface around the inside of the cell, the vapor condenses and the liquid falls into the liquid layer over the driver. The driver creates droplets that leave the liquid surface and the cycle continues.

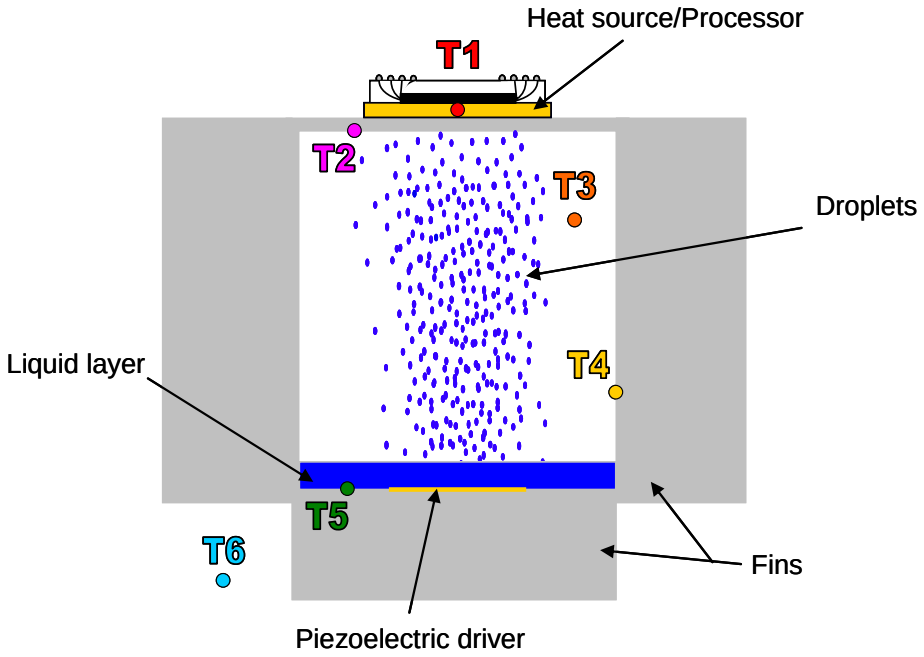

Figure 4.1: Schematic of modeled heat transfer cell

In the modeled heat transfer cell, key temperatures are used to evaluate heat transfer rates, thermal resistances, fluid properties, and temperatures of other cell components. Those key temperatures are labeled as T1 through T6 in Figure 4.1. The temperature T1 is the heat source temperature, T2 is the temperature of the inner surface on which droplets impinge, and T3 is the saturation temperature of the fluid within the cell. The temperature at T4 is the temperature of the inner surface on which condensation occurs, T5 is the temperature of the inner surface at the bottom of the liquid layer, and T6 is the ambient temperature. Heat transfer within the cell walls was modeled assuming

one-dimensional, steady-state conduction. Two-dimensional, steady-state conduction was modeled in the top surface of the cell where the heat source was attached to the cell and in the fins connected to the perimeter of the heat transfer cell.

The simulated heat source at the top surface of the cell is assumed to be a microprocessor, so the heat fluxes and temperatures selected for model simulation are compatible with expected values typically experienced during the operation of modern microelectronic designs. Orientation of the heat source to the cell is shown in Figure 4.2.

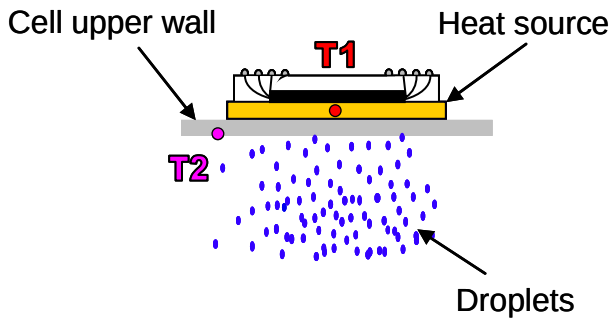

Figure 4.2: Heat source orientation to upper wall of heat transfer cell

As heat is conducted from the heat source through the upper surface of the cell wall, into the heat transfer cell, it spreads horizontally. Heat spreading thermal resistances can be used whenever heat is conducted from one region to another with a different cross sectional area. Since the model assumes one-dimensional conduction, a spreading resistance can accommodate two-dimensional effects, which is a function of the thermal properties and geometry of the upper surface of the cell. In the case of heat sink applications, the spreading resistance is used in the cell to approximate the effects of two-dimensional conduction. This results in a higher local temperature at the location where the heat source is placed. In cases where the surface area of the heat source is approximately equal to the area of surface to which it is attached, the contribution of the

spreading resistance to the source temperature is not significant. However, for the case of a small microprocessor attached to a much larger droplet cooling heat transfer cell, the thermal resistance of the upper surface of the cell can be modeled with an appropriate spreading resistance. The relationship used to describe the added two-dimensional thermal resistance is given by Equation 4.1 (Lee, 1998).

$$R_S = \left(\frac{A_S^{1/2} - A_H^{1/2}}{k_S \left(\pi A_S A_H\right)^{1/2}} \right) \left(\frac{\varphi k_S A_S R_0 + \tanh\left(\varphi t_S\right)}{1 + \varphi k_S A_S R_0 \tanh\left(\varphi t_S\right)} \right) \qquad 4.1$$

where φ is defined as

$$\varphi = \left(\frac{\pi^{3/2}}{A_S^{1/2}} \right) + A_H^{-1/2} \qquad 4.2$$

In Equations 4.1 and 4.2, R_S is the thermal resistance, A_S is the area of the sink area, A_H is the heat source area, k_S is the thermal conductivity of the sink, R_0 is the average thermal resistance of the sink, and t_S is the sink thickness. The correlation assumes that the heat source is centrally mounted on the sink, and that the heat sink has a uniform surface temperature. The spreading model addresses neither the shape of the heat source nor that of the sink, but it was found to yield results with an accuracy of approximately 5 percent over a wide range of applications with many combinations of different source/sink shapes, as long as the aspect ratio of the shapes involved did not exceed 2.5.

Selection of a correlation to simulate the phase change heat transfer rate from the upper surface to impinging droplets proved to be a difficult task. After an exhaustive review of droplet and spray cooling literature, no experimental or theoretical work was found that addressed the physical situation encountered in the present model. In the modeled heat transfer cell, droplets impinge on the bottom of a heated surface that provides no means for escape of the vapor. From a heat transfer perspective, this

orientation is undesirable for achieving maximum heat removal from the surface. In this orientation, as the impinging droplets evaporate, the vapor tends to stay near the heated surface, held there by the vapor's buoyancy. Thus, very little research has focused on evaluation of convective heat transfer rates or coefficients from inverted heated surfaces when cooled by impinging droplets. Due to the lack of heat transfer correlations for this orientation, alternate phase change relationships were used to simulate the mechanism of heat transfer from the upper surface of the cell.

Two cooling models were selected for use in the heat transfer model to simulate heat transfer from the heated inner surface of the heat transfer cell. They included an ideal droplet evaporation model, in which the heat transfer coefficient is dependent only on the liquid properties and flow rate, and Ohtake's (2003) mist cooling correlation. Descriptions of and the rationale for selection of each model follows.

The ideal model for evaporative cooling heat transfer assumed that the droplets generated on the liquid layer removed heat at a rate according to Equation 4.3. The magnitude of the heat transfer coefficient is determined by the liquid properties and the mass flow rate of the droplets. This heat flux relationship was selected because it represents the maximum cooling rate for a given mass flow rate of droplets that strike the heated surface (Ohtake and Koizumi, 2003).

$$q'' = h(\Delta T) = \frac{\dot{m} h_{fg} + \dot{m} c_p (T_s - T_{sat})}{A_s} \qquad 4.3$$

The heat flux, q'', is a surface-average quantity, h is the convective heat transfer coefficient, ΔT is the temperature difference between the heated surface and the impinging droplets, $\dot{m}$ is the liquid mass flow rate of the droplets, h_{fg} is the latent heat of vaporization of the liquid, c_p is the specific heat at constant pressure, T_s is the surface

temperature, T_{sat} is the saturation temperature of the liquid, and A_s is the heater surface area.

From mist cooling heat transfer experiments that involved air-assisted water sprays, Ohtake and Koizumi determined the individual contribution of the liquid mass flux of water to the heat transfer rate achieved during mist cooling. In the investigation, air-assisted mist cooling was used to cool an upward-facing copper heater surface. Three correlations of the mist cooling rate for non-boiling, droplet evaporation, and liquid film evaporation were developed for droplet mass flow rates between 0.08 and 2.22 g/s and air flow rates between 0.67 and 2.0 l/s. In the study, the copper heater surface area was 1.767 cm^2 and its surface temperature ranged from 50 to 130°C. The heat transfer rates ranged from 3 to 600 W/cm^2 for the non-boiling, droplet evaporation, and liquid film evaporation heat transfer modes. After evaluating the heat transfer rates of the air-assisted mist cooling and the contribution due to air-only cooling, the difference was attributed to the phase change of the liquid mass flux. The heat transfer coefficient for mist cooling by droplet evaporation was determined to be

$$h_{mist} = 35G^{0.259}\Delta T_W^{1.3} \qquad 4.4$$

where h_{mist} is the heat transfer coefficient in $W/(m^2°C)$, G is the liquid mass flux in $l/(m^2min)$, and ΔT_W is the temperature difference between the heated surface and liquid in °C. This correlation was chosen because the tested range of liquid mass flow rates, heater area, heater temperature, and heat transfer rates, were comparable to those simulated in this study's heat transfer cell model.

After evaporation of the droplets at the heater surface, the vaporized liquid condenses on the cool inside perimeter wall of the cell. The latent heat of vaporization is

released into the wall as vapor contacts the wall that is below the saturation temperature of the vapor. Heat is transferred to the wall and the vapor condenses back to liquid phase. Condensation of the vapor on the perimeter wall was modeled using a laminar film condensation correlation for the heat transfer coefficient for a vertical wall. The average heat transfer coefficient for condensation correlation developed, by Sadasivan and Lienhard (1987) is

$$h_{avg} = 0.943\left(\frac{g\rho_l(\rho_l - \rho_v)k_l^3 h'_{fg}}{\mu_l(T_{sat} - T_s)L} \right)^{1/4} \qquad 4.5$$

where L is the characteristic length of the condensing surface. The latent heat of vaporization is modified for inclusion of thermal advection effects, and takes the following form.

$$h'_{fg} = h_{fg} + 0.68c_{p,l}(T_{sat} - T_s) \qquad 4.6$$

After the heat is transferred to the outer surface wall of the cell, it is conducted along fins that are attached to the outside of the cell where the heat is eventually convected to the ambient environment. The fins are modeled as rectangular, uniform cross-section fins.

As previously stated, this heat transfer cell model assumes one-dimensional, steady-state heat transfer. Use of an equivalent thermal resistance circuit allows calculation of temperatures, heat fluxes, or other parameters of interest, given necessary information about the cell and the characteristics of the droplet generation discussed in the previous chapter. By solving the system of equations that result from the simulation of evaporation, condensation, conduction, convection, and other cell conditions in the heat transfer model, the thermal performance of the cell can be evaluated.

In Figure 4.3 is the equivalent thermal circuit that describes the modeled heat transfer cell. The nodes between the resistors are the nodal temperatures, $T1$ through $T6$, depicted in Figure 4.1. The thermal resistances, $R1$ through $R11$, are defined as:

$$R1 = \frac{t_{cell}}{k_{cell} A_{top}} \tag{4.7}$$

where $R1$ is the conductive thermal resistance through the cell wall at the top of the cell, where t_{cell} is the thickness of the cell wall, k_{cell} is the thermal conductivity of the cell wall material, and A_{top} is the area at the top of the cell.

$$R2 = R_S \tag{4.8}$$

In Equation 4.8, $R2$ is the thermal resistance caused by two-dimensional spreading in the cell wall at the top of the cell, where R_S is defined in Equation 4.1.

$$R3 = \frac{1}{h_{boil} A_{top}} = \frac{T2 - T3}{q_{top}} \tag{4.9}$$

In Equation 4.9, $R3$ is the convective thermal resistance from the surface of the cell wall at the top of the cell to the fluid of the inner volume of the cell, h_{boil} is the boiling heat transfer coefficient, and q_{top} is the heat transfer rate through at the top of the cell. The heat transfer coefficient, h_{boil}, is calculated using Equation 4.3 when using the ideal evaporation model or using Equation 4.4 when using Ohtake's mist cooling model.

$$R4 = \frac{1}{h_{condense} A_{wall}} = \frac{T3 - T4}{q_{wall}} \tag{4.10}$$

The convective condensation thermal resistance from the fluid of the inner volume of the cell to the circular perimeter of the cell is $R4$, $h_{condense}$ is the condensation heat transfer coefficient, A_{wall} is the area of the circular perimeter wall, and q_{wall} is the heat transfer rate through circular perimeter wall of the cell. The heat transfer coefficient, $h_{condense}$, is

calculated using Equation 4.5, where $h_{condense}$ is equal to h_{avg}.

$$R5 = \frac{t_{ll}}{k_{ll} A_{bottom}} = \frac{T3 - T5}{q_{bottom}} \tag{4.11}$$

In Equation 4.11, $R5$ is the conductive thermal resistance through the liquid layer at the bottom of the cell, t_{ll} is the thickness of the liquid layer, k_{ll} is the thermal conductivity of the water, A_{bottom} is the area at the bottom of the cell, and q_{bottom} is the heat transfer rate through the bottom of the cell. Condensation of vapor on the liquid layer surface was assumed not to occur. All condensation was assumed to occur on the cell perimeter wall.

$$R6 = \frac{t_{cell}}{k_{cell} A_{bottom}} \tag{4.12}$$

In Equation 4.12, $R6$ is the conductive thermal resistance through the cell wall at the bottom of the cell.

$$R7 = \frac{\ln(r_2 / r_1)}{2\pi k_{cell} H_{wall}} \tag{4.13}$$

In Equation 4.13, $R7$ is the conductive thermal resistance through the cell wall at the circular perimeter of the cell, r_1 is the inner radius of the cell, r_2 is the outer radius of the cell, and H_{wall} is the height of the circular perimeter wall of the cell.

$$R8 = \frac{1}{h_{amb} A_{bottom,base}} \tag{4.14}$$

In Equation 4.14, $R8$ is the convective thermal resistance from the un-finned outer surface of the bottom of the cell, h_{amb} is the ambient convective heat transfer coefficient, and $A_{bottom,base}$ is the un-finned area outside the bottom of the cell.

$$R9 = \frac{1}{h_{amb} A_{side,base}} \tag{4.15}$$

In Equation 4.15, $R9$ is the convective thermal resistance from the un-finned outer surface of the side of the cell and $A_{side,base}$ is the un-finned area outside the side of the cell.

$$R10 = \frac{\theta_{b,bottom}}{q_{bottom,fin}} \frac{1}{N_{fins,bottom}} \tag{4.16}$$

In Equation 4.16, $R10$ is the thermal resistance of the fins, $\theta_{b,bottom}$ is the temperature difference between the temperature at the base of the bottom fins and ambient temperature, $q_{bottom,fin}$ is the heat transfer rate through one fin on the bottom of the cell, and $N_{fins,bottom}$ is the number of fins on the bottom of the cell.

$$R11 = \frac{\theta_{b,side}}{q_{side,fin}} \frac{1}{N_{fins,side}} \tag{4.17}$$

In Equation 4.17, $R11$ is the thermal resistance of the fins, $\theta_{b,side}$ is the temperature difference between the temperature at the base of the side fins and ambient temperature, $q_{side,fin}$ is the heat transfer rate through one fin on the side of the cell, and $N_{fins,side}$ is the number of fins on the side of the cell.

Equation 4.18 is used to calculate heat transfer through individual fins on the side and bottom of the cell. It is the expression for heat transfer from fins of uniform cross-section with a tip condition of convection heat transfer (Incropera and DeWitt, 1990).

$$q = M \frac{\sinh(mL) + (h/mk)\cosh(mL)}{\cosh(mL) + (h/mk)\sinh(mL)} \tag{4.18}$$

$$M = \theta_b \sqrt{hPkA_c} \tag{4.19}$$

$$m = \sqrt{hP/kA_c} \tag{4.20}$$

In Equations 4.18 to 4.20, L is the fin length, k is the thermal conductivity of the fin material, h is the heat transfer coefficient at the fin surface, P is the fin perimeter length, A_c

is the cross-sectional area of the fin, and θ_b is the difference between the fin base temperature and ambient temperature.

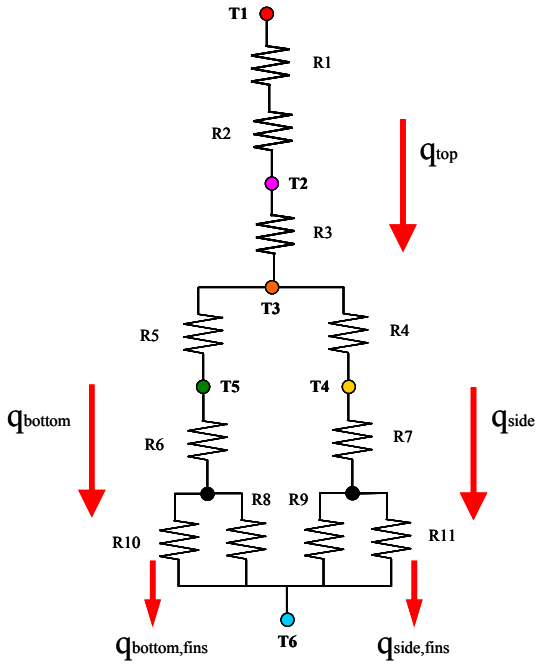

Figure 4.3: Thermal resistance diagram for heat transfer cell model

Heat transfer from the heat source into the inner volume of the cell is represented as q_{top}. In the thermal resistance diagram, it is the heat that flows from T1 to T3. Heat leaves the cell through the side and bottom of the cell and is represented as q_{side} and q_{bottom}. The heat, q_{bottom}, flows from T3 to T6 via the thermal resistances R5, R6, R8, and R10. The heat, q_{side}, flows from T3 to T6 via the thermal resistances R4, R7, R9, and R11. Each of the resistances are solved using cell operating characteristics and conditions that are entered into the heat transfer model to find heat transfer rates and temperatures. All of the properties of water and the cell material are determined as functions of temperature in the model.

The preceding series of algebraic equations were solved using the Windows-based application, Engineering Equation Solver (EES) Academic Version 6.840-3D. EES is an equation-solving program that is capable of solving large sets of non-linear algebraic and differential equations and has the flexibility to execute customized program subroutines. It also contains built-in functions for thermodynamic properties of many substances, including water, steam, air, and refrigerants.

4.2 Results

Verification of the heat transfer cell model was performed by modeling a droplet heat transfer cell that has previously been studied by Heffington at the Georgia Institute of Technology in experimental investigations. This heat transfer cell was made of aluminum and used water as the working fluid. A piezoelectric driver was used to generate droplets from a liquid layer. Using the heat transfer cell to cool an attached heat source, cell heat transfer rates of 123 to 175 W were achieved at heat source temperatures of 110 to 142ºC. A photograph of the heat transfer cell, without its cover, is shown in Figure 4.4.

Using characteristics of the actual heat transfer cell, the heat transfer model was configured to simulate steady state operation of the actual cell. The heat transfer rates calculated by the heat transfer model were then compared to the heat transfer rates measured experimentally. Dimensions and attributes of the actual cell that were simulated in the heat transfer model are listed in Table 4.1.

Figure 4.4: Photograph of actual heat transfer cell (Heffington)

Table 4.1: Actual heat transfer cell dimensions and attributes

Parameter	**Values**
Inside diameter	44.3 mm
Inside height	29.7 mm
Overall cell diameter	71.25 mm
Overall cell height	55 mm
Cell wall thickness	1.5 mm
Heat source area	1 cm^2
Fin length	10.5 mm
Fin thickness	1.2 mm
Number of fins	60
Cell material	Aluminum
Working fluid	Water

The driver voltage, driver frequency, and liquid layer thickness were not known for the provided conditions at which the cell heat transfer rate was measured as a function of the heater temperature. Despite the absence of that information, the heat transfer model could be used to simulate operation of the actual heat transfer cell because those driver and liquid layer parameters drive the droplet mass flow rate, which enables heat transfer from the heated surface. Comparable conditions for droplet generation were simulated using the droplet mass flow rate data collected for the 38.1 mm constrained

pool as a function of driver frequency, driver voltage, liquid layer thickness, and interception distance.

The actual heat transfer cell did not have fins on its bottom, so the heat transfer model was configured so that bottom fins would not be simulated. Though there were no fins on the bottom of the cell, the cell's side fins extended approximately 10 mm past the bottom of the cell. Because this is an irregular fin configuration and the amount of heat transferred through these sections would be much less than the heat transferred through the fin sections attached directly to the cell wall, these fin sections were not accounted for in the heat transfer cell model.

Figure 4.5 is a graph of Heffington's experimentally measured cell heat transfer rate as a function of heat source temperature. Included in the graph, are heat transfer rates calculated using the heat transfer model. These cell heat transfer rate calculations were made using Ohtake's mist cooling correlation for heat removal from the upper surface of the cell, Equation 4.4. The heat transfer model was executed for three driver-liquid layer conditions for which droplet mass flow rates were reported in the previous chapter. The heat transfer rates predicted by the model were slightly higher than those measured experimentally and the slopes of the heat transfer rate as a function of heat source temperature were similar. For the tested conditions, droplet mass flow rate decreased with liquid layer thickness. Because driver voltage also affects droplet generation, the heat transfer rate calculations can be matched to the measured heat transfer results by decreasing the driver voltage.

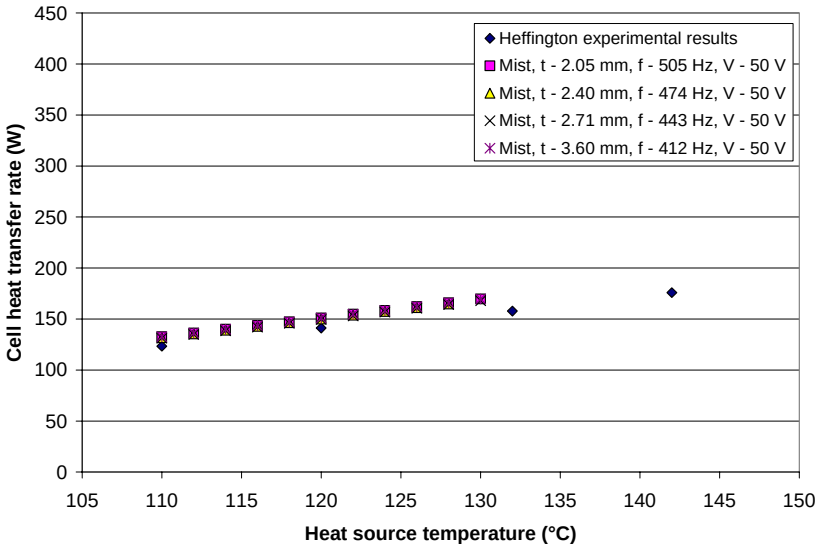

Figure 4.5: Actual and predicted (mist cooling) heat transfer results as a function of heat source temperature

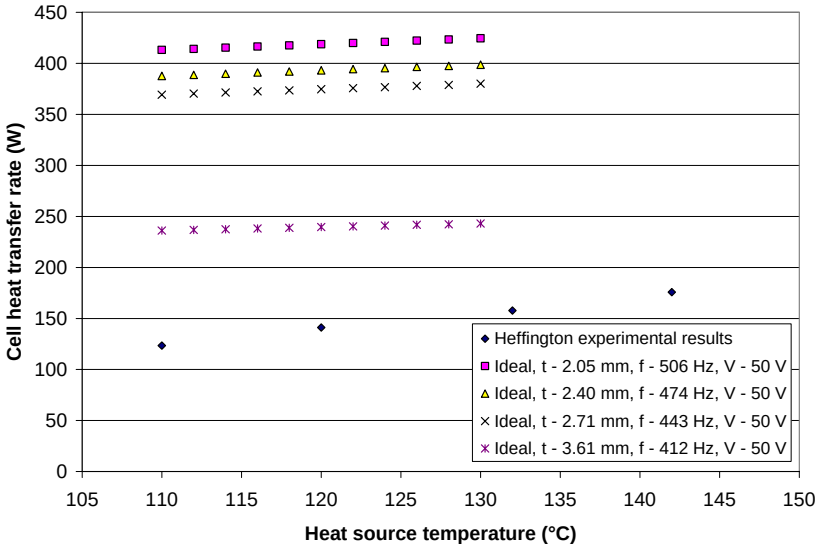

Figure 4.6: Actual and predicted (ideal evaporation) heat transfer results as a function of heat source temperature

Figure 4.6 is a graph of Heffington's experimentally measured heat transfer rates and cell heat transfer rate calculations made using the ideal evaporative cooling model for heat removal from the upper surface of the cell, Equation 4.3. The cell heat transfer rates predicted using the heat transfer model with ideal evaporative cooling were considerably higher than when using the mist cooling correlation. These results indicate the maximum

heat transfer rates possible based on latent heat and sensible heat supplied by droplets. The assumption of ideal evaporative cooling in the heat transfer model also yielded heat transfer rate predictions that were much higher than heat transfer rates measured for the actual cell.

Heat transfer rates predicted using the heat transfer model with the mist cooling correlation agreed well with the heat transfer rate measurements made on the actual cell. Based on results presented in Figure 4.5, the heat transfer model's ability to simulate an actual droplet cooling heat transfer cell was verified. Without other actual droplet cooling heat transfer cells results available for comparison, verification of the model's heat transfer results is limited to the comparison that has been presented.

The following analysis is a study of the effect of driver voltage, driver frequency, liquid layer thickness, and other cell attributes on the cell heat transfer rate. Except where indicated, the configuration of the simulated heat transfer cell is the same as was used to compare model results to actual heat transfer cell results. The simulated heat transfer cell attributes are reported in Table 4.1. In each study, the mist cooling correlation is used for simulation of heat removal from the upper surface of the cell.

In the heat transfer model, many variables are calculated and used to evaluate the cell's thermal performance. Those variables include surface temperatures, heat transfer rates and fluxes, thermal resistances, mass flow rates, heat transfer coefficients, fluid properties, and cell dimensions. Heat transfer rates are calculated at the top of the cell where heat enters the cell volume, at the cell wall where heat leaves the cell volume, and at the cell bottom where heat also leaves the volume. Heat transfer through fins attached

to the cell walls and through the cell bottom out to the ambient environment, is also calculated.

Figure 4.7 is a graph of cell heat transfer rate as a function of driver frequency. For heat source temperatures of 110, 120, and 130ºC, four liquid layer thicknesses were evaluated for their effects on the cell heat transfer rates. In each case, the driver voltage was 50 V. The highest cell heat transfer rates were achieved when the liquid layer thickness was 2.05 mm and the heat source temperature was 130ºC. The variation of the cell heat transfer rate with driver frequency, driver voltage, and liquid layer thickness was due to the variation of droplet generation for each of the driver-liquid layer combinations. The trends of the cell heat transfer rate and droplet mass flow rate as a function of frequency, for each liquid layer thickness, are similar. The similarity is due to the dependence of the calculated heat transfer rate on the droplet mass flow rate.

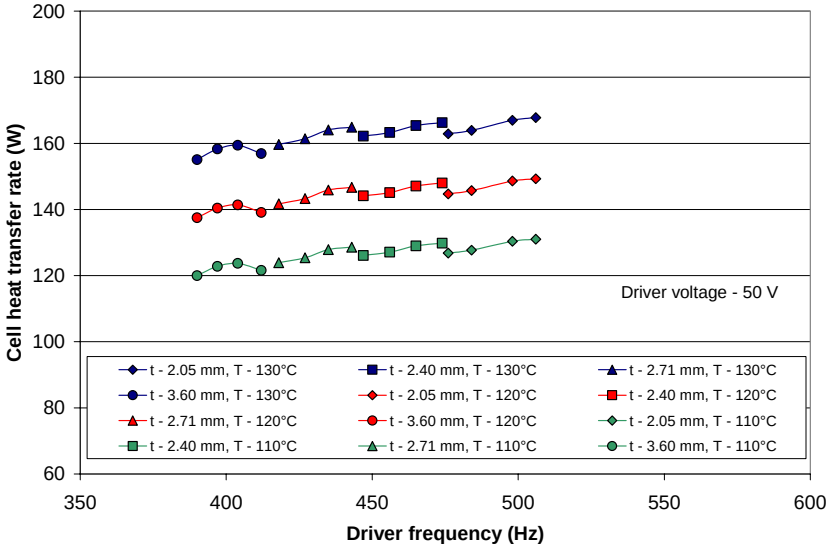

Figure 4.7: Cell heat transfer rate as a function of driver frequency for different heat source temperatures and liquid layer thicknesses

Figure 4.8 is a graph of the cell heat transfer rate as a function of the inner height of the cell. As the inner height of the cell was increased from its initial height of 29.7 mm, the inner surface onto which the vapor condenses and the fin area increased. Increases in these surface areas increase the ability of the heat transfer cell to remove heat from a heat source that is at a prescribed temperature. Conversely, as the height of the cell increases, the mass flow rate of droplets impinging on the heated upper cell wall decreases. Thus, two opposing effects on the cell heat transfer rate result as the cell height is increased. The graph indicates that as the as the cell inner height increases the cell heat transfer rate increases. This result indicates that the heat transfer rate decrease resulting from the decreased droplet mass flow rate is much less than the heat transfer rate increase that results from the increases in condensation and fin area. The changes in the condensation and fin areas decreased the cell thermal resistance more than the changes in the droplet mass flow rate increased the cell thermal resistance.

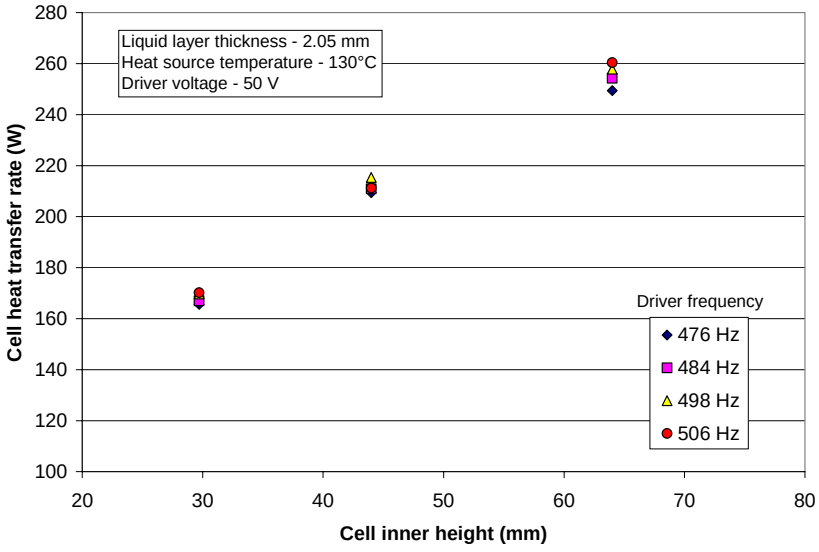

Figure 4.8: Cell heat transfer rate as a function of cell inner height

The effect of driver voltage (displacement) on the cell heat transfer rate was studied and results are reported in Figure 4.9. In this study, the inner cell height was modeled at 44 mm, with a liquid layer thickness of 2.05 mm for a heat source temperature of 130ºC. For constant driver frequencies, the driver voltage was varied between 35 and 50 V to determine the effect of driver voltage on the cell heat transfer rate. Overlapping of the heat transfer rate curves, for constant driver frequencies, is due to changes in droplet mass flow rate, as shown in Figure 3.27. For a given liquid layer thickness, droplet generation decreases as the driver voltage (displacement) decreases. Thus, the cell heat transfer rates at the higher frequencies for a given liquid layer thickness are lower when the driver voltage is decreased. At the driver frequency of 506 Hz, the cell heat transfer rate is zero below a driver voltage of 40 V because generated droplets do not travel far enough from the surface of the liquid layer to reach the heated upper surface.

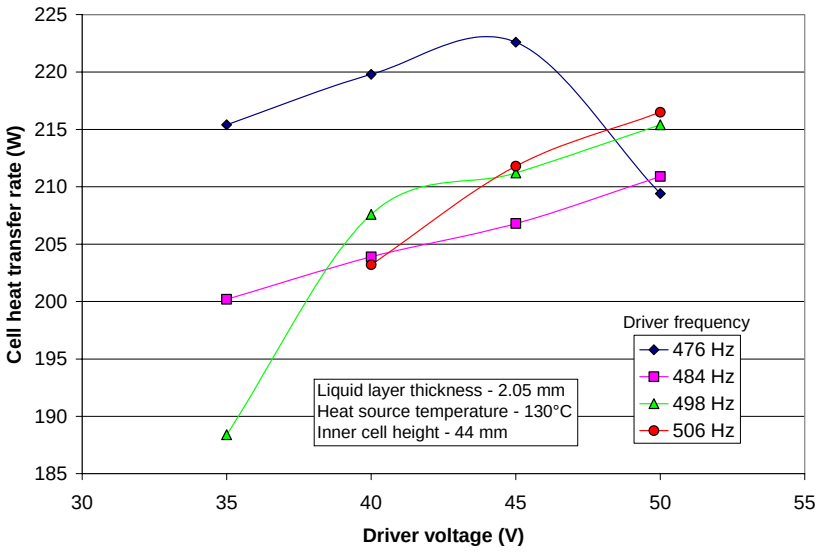

Figure 4.9: Cell heat transfer rate as a function of driver voltage

To determine the effect of using a higher thermal conductivity material on the cell heat transfer rate, the cell material was simulated as copper and compared to results using aluminum. The heat transfer rates, presented in Figure 4.10, were calculated for heat source temperatures between 110 and 130ºC and parameters from Table 4.1. Due to the higher thermal conductivity of copper, conductive thermal resistances throughout the cell were reduced, enabling higher heat transfer rates at each temperature. The cell heat transfer rate increases approximately 7 percent when copper, instead of aluminum, is used as the cell material.

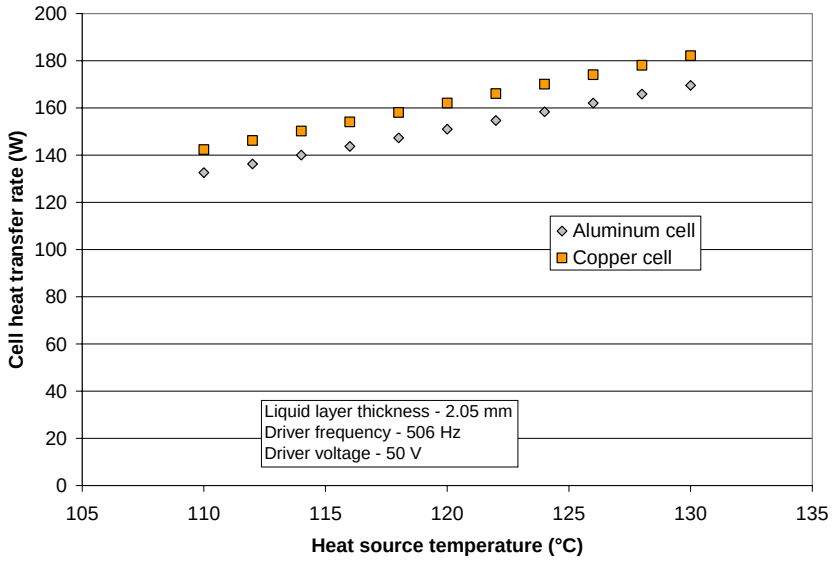

Figure 4.10: Cell heat transfer rate as a function of heat source temperature for aluminum and copper cells

CHAPTER 5

CONCLUSIONS

The objectives of this investigation were to determine the parameters that influence the generation of droplets from the surface of a liquid layer, develop a method to determine the conditions necessary for droplet generation, and to develop an analytical model that can be used to predict the local and global heat transfer rates in a droplet cooling heat transfer cell.

The dependence of droplet generation on the driver displacement, acceleration, and frequency, and liquid layer thickness were determined by experimental investigation. During the investigation, three pool boundary conditions were evaluated. The three configurations were an open pool, a 38.1 mm constrained pool, and a 50.8 mm constrained pool. Trends observed included the observance that the driver frequency necessary to generate droplets increased as the liquid layer thickness decreased. It was determined that the frequency range for droplet generation also increased as the liquid layer thickness decreased. The effect of using a 38.1 mm diameter ring to constrain the pool was to decrease the frequency range in which droplet generation occurred. When using a 50.8 mm diameter ring to constrain the pool, there was no measurable effect when compared to the results obtained when using the open pool. The influence of waves that were reflected from the pool wall boundary was to stabilize wave motion, if the boundary was positioned close enough to the driver so that the reflected waves had enough amplitude to interfere with the waves produced by driver displacement.

At higher frequencies, the measured average droplet diameters followed the trend proposed by Lang, relating average droplet diameter to vibration frequency. Below 460 Hz, the measured average droplet diameters were nearly constant with frequency and 13 to 20% smaller than the diameters predicted using Lang's correlation. The resulting droplet diameter measurements were the same for the three pool boundary conditions.

The droplet mass flow rates measured in this investigation were quite broad. It was expected that because all of the droplets generated were produced in a frequency span of approximately 215 Hz, and within a very specific frequency range for each liquid layer thickness, that the flow rates would have been just as specific and limited. To the contrary, it was determined that the droplet mass flow rate could be tuned to meet nearly any requirement within its maximum droplet generation capabilities. Because droplet generation is dependent on three variables (liquid layer thickness, driver displacement, and driver acceleration), which are all quite easily adjusted, using a submerged piezoelectric driver for droplet generation would be appropriate in applications that require variable droplet mass flow rates. The negative associated with the ease of adjustment of the droplet mass flow rate is in the quantification of the flow rates and associated conditions for development of models to predict performance. The droplet mass flow rate measured for one liquid layer thickness at a given frequency could nearly double by varying the frequency 20 Hz.

Measurement of the driver's displacement and acceleration was key to relating the observed driver frequency, driver voltage, and liquid layer thickness conditions to droplet generation. Knowledge of the driver's displacement and acceleration were necessary for the development of a method for determining the conditions for which droplet generation

occurs. The waves from which the droplets are generated are dependent on the displacement and acceleration of the driver.

The dimensionless acceleration, developed in this study, is a useful tool for those who seek to use piezoelectric drivers for droplet generation from a liquid layer. The dimensionless acceleration is applicable for open and constrained pools. With knowledge of the acceleration and displacement of the selected driver, the investigator can use the dimensionless acceleration to determine the range of conditions for which droplet generation will occur, assuming water liquid layer thicknesses are comparable to those used in this investigation. Until other liquids are investigated for droplet generation from a liquid layer by a vibrating piezoelectric driver, it should be assumed that the dimensionless acceleration parameter is only valid for droplet generation in water.

Though a single diameter driver was used for this investigation, the analysis should work using drivers of similar diameters. The results of this analysis should be valid as the dimensionless parameter that was developed is not directly dependent on physical attributes of the driver, such as diameter, thickness, and disk material. The frequency dependent acceleration and displacement of the driver are the important characteristics. To verify the generality of dimensionless acceleration of the dimensionless expression developed in this study, investigation of droplet generation from a liquid layer can be performed with different diameter piezoelectric drivers.

An expected difference when using different diameter drivers is in the droplet mass flow rate. When using a smaller diameter driver, with a similar accelerations and displacements to the driver used in this study, the measured droplet mass flow rate should be less. Due to the decreased area of a smaller driver, fewer droplets would be produced

from the liquid surface area above driver from which droplet generation occurs. By the same reasoning, higher droplet mass flow rates are expected when using a larger diameter driver with similar characteristics to the driver used in this study.

The heat transfer model developed in this study was configured so that it could accommodate a great number of parameter variations that can be used for the design of a simple heat transfer cell. The model was used to determine the effect of droplet cooling on the heat transfer rate from a heated surface, but it can also be used to determine the influence of other embodied parameters that may be of interest for thermal management applications. By comparing the results of this heat transfer model to results of an experimentally investigated droplet cooling heat transfer cell, the model provided reasonably accurate predictions of heat transfer performance. Combined with the results of the droplet generation results of this study, the heat transfer cell model was used to make predictions of heat transfer performance of a droplet cooling heat transfer cell.

Confidence in the results produced by the heat transfer cell model would be greater if a suitable phase change model for droplet cooling on an inverted heated surface was available. Because the performance of a heat transfer cell depends so heavily on the rate at which heat is removed from the heat source, it is necessary to have an accurate model that can be used for a range of heat source temperatures, heat fluxes, and droplet mass flow rates. In its present form, the model is an adequate tool for obtaining estimates of heat transfer performance and for identifying trends that can be used as guides in the development of improved droplet cooling heat transfer cells.

CHAPTER 6

FUTURE WORK AND RECOMMENDATIONS

Because of this study, there are several recommendations for future research. In the area of heat transfer, it would be of great benefit to droplet cooling heat transfer cell investigators if a study of heat transfer from inverted heated surfaces was performed. The lack of research of this heat source orientation leaves open opportunities for those who are interested in developing heat transfer correlations for regimes of two phase cooling in this area. Those correlations could then be integrated into a heat transfer cell model to yield results that may be closer to the measured results from actual cells.

As the droplet generation experiments were performed, it was observed that during the production of droplets, the sound level of the driver was much higher than when droplets were not being produced. The frequencies at which droplets were being generated were much lower than the measured resonant frequency of the driver in its enclosure. A study that focuses on the acoustic energy that is radiated into the liquid layer might yield results that might be useful in predicting the conditions necessary for droplet generation from the liquid layer.

The use of a laser measuring system to determine the droplet diameters and distribution of droplets produced during droplet generation would be a helpful tool for collecting information more quickly. The high-speed photography configuration used in this study yielded exceptionally high-resolution images for analysis, but the procedure for measurement of the droplet diameters was long and tedious. An investigation into the parameters that influenced generation of droplets whose average diameters deviated from

Lang's proposed relationship between average droplet diameter and frequency would also add to the body of knowledge concerning droplet generation using piezoelectric drivers.

Finally, an investigation that focuses on the influence of viscosity and surface tension on the generation of droplets from a liquid layer using a piezoelectric driver is also a potential source for interesting research. It is expected that there is a dependence of droplet generation, using a piezoelectric driver, on those liquid properties, just as results have shown in other droplet generation investigations. Results of such research would also be of benefit to those who seek to use other liquids in droplet cooling heat transfer cells.

APPENDIX

UNCERTAINTY ANALYSIS

This section contains the uncertainty analyses associated with measurements of the droplet mass flow rates and droplet diameters.

To measure the droplet flow rates as described in Section 3.3.1.3, the change in mass of the sponge was divided by the duration for which droplets were absorbed by it.

$$\dot{m} = \frac{m_2 - m_1}{t_2 - t_1}$$

The uncertainty of the individual mass measurements of the sponge was +/- 0.01 grams. The estimated uncertainty associated with the synchronization of the stopwatch measurement of time and activation of the signal generator that provided power to the driver was +/- 0.1 seconds.

Calculation of the mass flow rate for one condition follows.

m_1 = 16.32 +/- 0.01 g t_1 = 0.00 +/- 0.1 s

m_2 = 18.27 +/- 0.01 g t_2 = 10.52 +/- 0.1 s

The change in mass of the sponge was:

1.95 +/- 0.02 g or 1.95 g +/- 1.0 %

The duration of the experiment was:

10.52 +/- 0.2 s or 10.52 +/- 1.9 %

Thus, the measurement of mass flow rate at this condition was:

<u>0.185 g/s +/- 2.9% or 0.185 +/- 0.005 g/s</u>

To measure the average droplet diameter as described in Section 3.3.1.2, the droplet diameters were first measured in pixels of a digital image. The average diameter of the droplets was calculated and converted from pixels to millimeters using the conversion ratio that was determined by measurement of a known cylinder diameter in each image.

$$\text{Average droplet diameter (mm)} = \frac{\text{Average droplet diameter (pixels)}}{\text{Cylinder diameter (pixels)/Cylinder diameter (mm)}}$$

The uncertainty of the micrometer used to measure the cylinder was 0.005 mm. The uncertainty associated with measurement of the droplet and cylinder diameters from the digital images was one pixel. Within the depth of field, the uncertainty of the droplet diameter was 4.7%. This uncertainty is due to the occurrence of droplets within the depth of field, but closer or farther away than the focus distance.

Calculation of the average droplet diameter for one condition follows.

Average droplet diameter	9.13 +/- 1 pixel 9.13 pixels +/- 11.0%
Average droplet diameter	9.13 +/- 0.43 pixel 9.13 pixels +/- 4.7%
Cylinder diameter	4.127 +/- 0.005 mm 4.127 mm +/- 0.12%
Cylinder diameter	71 +/- 1 pixel 71 pixels +/- 1.4%

Thus, the average droplet diameter in the digital image was:

0.531 mm +/- 17.22% or 0.531 +/- 0.091 mm

REFERENCES

Airey, J., 1911, "The Vibration of Circular Plates and Their Relation to Bessel Functions," Physics Society, **23**, pp. 225-232.

Bechhoeffer, J., Ego, V., Manneville, S., and Johnson, B., 1995, "Experimental Study of the Onset of Parametrically Pumped Surface Waves in Viscous Fluids," Journal of Fluid Mechanics, **288**, pp. 325-350.

Bernardin, J. D., Stebbins, C. J., and Mudawar, I., 1997, "Effects of Surface Roughness on Water Droplet Impact History and Heat Transfer Regimes," International Journal of Heat and Mass Transfer, **40**(1), pp. 73-88.

Bonacina, C., Del Giudice, S., and Comini, G., 1979, "Dropwise Evaporation," ASME Journal of Heat Transfer, **101**(3), pp. 441-446.

Carrington, H., 1925, "The Frequencies of Vibration of Flat Circular Plates Fixed at the Circumference," Philosophical Magazine, **50**(6), pp. 1261-1264.

Cerda, E. A. and Tirapegui, E. L., 1998, "Faraday's Instability in Viscous Fluid," Journal of Fluid Mechanics, **368**, pp. 195-228.

Dean, R. G. and Dalrymple, R. A., 1991, *Water Wave Mechanics for Engineers and Scientists*, World Scientific, Singapore.

Denney, D. L., 1996, "High Heat Flux Cooling Via a Monodispersed Controllable Spray," Masters Thesis, School of Mechanical Engineering, Georgia Institute of Technology, Atlanta, GA.

Eisenmenger, W., 1959, "Dynamic Properties of the Surface Tension of Water and Aqueous Solutions of Surface-Active Agents with Standing Capillary Waves in the Frequency Ranged from 10 KHz to 1.5 MHz," Acoustica, **9**(4), pp. 327-340.

Faghri, A., 1995, *Heat Pipe Science and Technology*, Taylor & Francis, Washington, DC, Chap. 1-5.

Faraday, M., 1831, "On a Peculiar Class of Acoustical Figures and on Certain Forms Assumed by Groups of Particles Upon Vibrating Elastic Surfaces," Philosophical Transactions of the Royal Society of London, **121**(299).

Garner, S. D., 1996, "Heat Pipes for Electronics Cooling Applications," Electronics Cooling, **2**(3),

Goodridge, C. L., Shi, W. T., Hentschel, H. G. E., and Lathrop, D. P., 1997, "Viscous Effects in Droplet-Ejecting Capillary Waves," Physical Review E., **56**(1), pp. 472-475.

Goodridge, C. L., Shi, W. T., and Lathrop, D. P., 1996, "Threshold Dynamics of Singular

Gravity-Capillary Waves," Physical Review Letters, **76**(11), pp. 1824-1827.

Hall, D. and Mudawar, I., 1996, "Optimization of Quench History of Aluminum Parts for Superior Mechanical Properties," International Journal of Heat and Mass Transfer, **39**(1), pp. 81-95.

Halvorson, P. J., Carson, R. J., Jeter, S. M., and Abdel-Khalik, S. I., 1994, "Critical Heat Flux Limits for a Heated Surface Impacted by a Stream of Liquid Droplets," ASME Journal of Heat Transfer, **116**, pp. 679-685.

Heffington, S. N., 2000, "Development and Analysis of a Vibration-Induced Droplet Atomization Module for High Heat Flux Cooling Applications," Ph.D. Thesis, School of Mechanical Engineering, Georgia Institute of Technology, Atlanta, GA.

Heffington, S. N., Black, W. Z., and Glezer, A., 2001, "Vibration-Induced Droplet Atomization Heat Transfer Cell for Cooling of Microelectronic Components," *Intersociety Electronic Packaging Technical/Business Conference and Exhibition*, ASME, **2**, pp. 779-784.

Hughes, W. F. and Brighton, J. A., 1999, *Schaum's Outline of Theory and Problems of Fluid Dynamics*, McGraw-Hill, New York.

Incropera, F. P. and DeWitt, D. P., 1990, *Fundamentals of Heat and Mass Transfer*, John Wiley & Sons, New York.

James, A. J., 2000, "Vibration Induced Droplet Ejection," Ph.D. Thesis, School of Mechanical Engineering, Georgia Institute of Technology, Atlanta, GA.

Joshi, Y., 2001, "Heat out of Small Packages," Mechanical Engineering, **123**(12),

Kopchikov, I. A., Voronin, G. I., Kolach, T. A., Labuntsov, D. A., and Lebedev, P. D., 1969, "Liquid Boiling in a Thin Film," International Journal of Heat and Mass Transfer, **12**, pp. 791-796.

Kumar, K. and Tuckerman, L. S., 1994, "Parametric Instability of the Interface between Two Fluids," Journal of Fluid Mechanics, **279**, pp. 49-68.

Kurokawa, M. and Toda, S., 1991, "Heat Transfer of an Impacted Single Droplet on the Wall," *Proceedings of the 3rd ASME/JSME Thermal Engineering Joint Conference*, ASME, New York, NY, pp. 141-146.

Lang, R. J., 1962, "Ultrasonic Atomization of Liquids," Journal of the Acoustical Society of America, **34**(1), pp. 6-8.

Lee, S., 1998, "Calculating Spreading Resistance in Heat Sinks," Amkor Electronics, Inc., Chandler, AZ.

Leissa, A. W., 1993, *Vibration of Plates*, Acoustical Society of America, Chap. 1-3.

Lierke, E. G. and Griesshamer, G., 1967, "The Formation of Metal Powder by Ultrasonic Atomization of Molten Metals," Ultrasonics, pp. 224-228.

Lin, L. and Ponnappan, R., 2003, "Heat Transfer Characteristics of Spray Cooling in a Closed Loop," International Journal of Heat and Mass Transfer, **46**(20), pp. 3737-3746.

Makino, K. and Michiyoshi, I., 1984, "Behavior of Water Droplet on Heated Surfaces," International Journal of Heat and Mass Transfer, **27**(5), pp. 781-791.

Makino, K. and Michiyoshi, I., 1987, "Discussion of Transient Heat Transfer to a Water Droplet on Heated Surfaces under Atmospheric Pressure," International Journal of Heat and Mass Transfer, **30**(9), pp. 1895-1905.

Michiyoshi, I. and Makino, K., 1978, "Heat Transfer Characteristics of Evaporation of a Liquid Droplet on Heated Surfaces," International Journal of Heat and Mass Transfer, **21**(5), pp. 605-613.

Monde, M., 1979, "Critical Heat Flux in the Saturated Forced Convection Boiling on a Heated Disk with Impinging Droplets," Heat Transfer Japanese Research, **8**(2), pp. 54-64.

Mudawar, I., 2001, "Assessment of High-Heat-Flux Thermal Management Schemes," IEEE Transactions on Components and Packaging Technologies, **24**(2), pp. 122-141.

Munson, B. R., Young, D. F., and Okiishi, T. H., 1998, *Fundamentals of Fluid Mechanics*, John Wiley & Sons, Inc., New York, Chap. 6,10.

Ohtake, H. and Koizumi, Y., 2003, "Study on Boiling Heat Transfer and Critical Heat Flux in Mist Cooling (Effect of Air Flow Rate on Heat Transfer and Behavior of Liquid on Heating Surface)," *2003 ASME International Mechanical Engineering Congress*, ASME, **374**, pp. 55-59.

Ortiz, L. and Gonzalez, J., 1999, "Experiments on Steady-State High Heat Fluxes Using Spray Cooling," Experimental Heat Transfer, **12**(3), pp. 215-233.

Pais, M., Chow, L. C., and Mahefkey, E. T., 1992, "Surface Roughness and Its Effects on the Heat Transfer Mechanism in Spray Cooling," ASME Journal of Heat Transfer, **114**(1), pp. 211-219.

Pederson, C. O., 1970, "An Experimental Study of the Dynamic Behavior and Heat Transfer Characteristics of Water Droplets Impinging Upon a Heated Surface," International Journal of Heat and Mass Transfer, **13**(2), pp. 369-381.

Peskin, R. L. and Raco, R. J., 1963, "Ultrasonic Atomization of Liquids," Journal of the Acoustical Society of America, **35**(9), pp. 1378-1381.

Pohlmann, R. and Stamm, K., 1965, "Untersuchung Zum Mechanismus Der Ultraschallvernebelung an Fluessigkeitsoberflaechen Im Hinblick Auf Technische Anwendungen," Forschungsber, Landes Nordrhein-Westfalien, **1480**, pp. 1-5.

Rayleigh, J. W. S., 1896, *The Theory of Sound*, Vol. 2, Reprint, Dover Publications, New York, 1945, pp. 343-345.

Rohsenow, W. M., 1952, "A Method of Correlating Heat Transfer Data for Surface Boiling Liquids," Transactions of ASME, **74**, pp. 969.

Rozenberg, L. D., 1973, *Physical Principles of Ultrasonic Technology*, Plenum Press, New York.

Sadasivan, P. and Lienhard, J. H., 1987, "Sensible Heat Correction in Laminar Film Boiling and Condensation," Journal of Heat Transfer, **109**(45), pp. 545-547.

Sawyer, M. L., Jeter, S. M., and Abdel-Khalik, S. I., 1997, "A Critical Heat Flux Correlation for Droplet Impact Cooling," International Journal of Heat and Mass Transfer, **40**(9), pp. 2123-2131.

Sawyer, M. L., Messana, M. M., and Jeter, S. M., 1993, "High Intensity Heat Transfer to a Stream of Monodispersed Droplets with Variable Velocity and Uniform Mass Flow Rate," *ASME 29th National Heat Transfer Conference*, ASME.

Sellers, S. M., 2000, "Heat Transfer Resulting from the Evaporation of Liquid Droplets on a Horizontal Heated Surface," Ph.D. Thesis, School of Mechanical Engineering, Georgia Institute of Technology, Atlanta, GA.

Sheffield, R. J., 1994, "High Heat Flux Spray Cooling," Ph.D. Thesis, School of Mechanical Engineering, Georgia Institute of Technology, Atlanta, GA.

Shoji, M., Wakunaga, T., and Kodama, K., 1984, "Heat Transfer from a Heated Surface to an Impinging Subcooled Droplet (Heat Transfer Characteristics in the Non-Wetting Regime)," Heat Transfer Japanese Research, **13**(3), pp. 50-67.

Sollner, K., 1936, "The Mechanism of the Formation of Fogs by Ultrasonic Waves," Transactions of the Faraday Society, **32**, pp. 1532-1536.

Sorokin, V. I., 1957, "The Effect of Fountain Formation at the Surface of a Vertically Oscillating Liquid," Soviet Physical Acoustics, **3**, pp. 281-291.

Sozbir, N., Chang, Y. W., and Yao, S. C., 2003, "Heat Transfer of Impacting Water Mist on High Temperature Metal Surfaces," Journal of Heat Transfer, **125**(1), pp. 70-74.

Toda, S., 1972, "A Study of Mist Cooling (1st Report: Investigation of Mist Cooling)," Heat Transfer Japanese Research, **1**(3), pp. 39-50.

Toda, S., 1974, "A Study of Mist Cooling (2nd Report: Theory of Mist Cooling and Its Fundamental Experiments)," Heat Transfer Japanese Research, **3**(1), pp. 1-44.

Virnig, J. C., Berman, A. S., and Sethna, P. R., 1988, "On Three-Dimensional Nonlinear Subharmonic Resonant Surface Waves in a Fluid: Part II - Experiment," Journal of Applied Mechanics, **55**(1), pp. 220-224.

Vukasinovic, B., 2002, "Vibration-Induced Droplet Atomization," Ph.D. Thesis, School of Mechanical Engineering,, Georgia Institute of Technology, Atlanta, GA.

Vukasinovic, B., Smith, M. K., and Glezer, A., 2004, "Spray Characterization During Vibration-Induced Drop Atomization," Physics of Fluids, **16**(2), pp. 306-316.

Wachters, L. H. J., Smulders, L., Vermeulen, J. R., and Kleiweg, H. C., 1966, "The Heat Transfer from a Hot Wall to Impinging Mist Droplets in the Spheroidal State," Chemical Engineering Science, **21**, pp. 1231-1238.

Wijetunga, P. and Levi, A. F. J., 2002, "The Case for Fiber-to-the-Processor," *Electrochemical Society Proceedings*, **4**, pp. 381-397.

Wood, R. W. and Loomis, A. L., 1927, "The Physical and Biological Effects of High-Frequency Sound-Waves of Great Intensity," London, Edinburgh, and Dublin Philosophical Magazine and Journal of Science, **4**(22), pp. 417-436.

Xiong, T. Y. and Yuen, M. C., 1991, "Evaporation of a Liquid Droplet on a Hot Plate," International Journal of Heat and Mass Transfer, **7**, pp. 1881-1894.

Yao, S. C. and Choi, K. J., 1987, "Heat Transfer Experiments of Mono-Dispersed Vertically Impacting Sprays," International Journal of Multiphase Flow, **13**(5), pp. 639-648.

Zuber, N., 1958, "On the Stability of Boiling Heat Transfer," Transactions of ASME, **80**, pp. 711.

VITA

Frank Pyrtle, III. was born in February 1973, in Houston, Texas where he also attended Wesley Elementary School, Wainwright Magnet Elementary School, Clifton Middle School, and graduated from Jesse H. Jones Vanguard High School. He graduated with a Bachelor of Science in mechanical engineering from Texas A&M University in December 1996.

After graduation, he continued his academic career as a graduate student at Texas A&M University. In August 1999, he graduated with a Masters of Science in mechanical engineering after completion of his thesis, an analysis of the evaporator/artery of an alkali metal thermal to electric conversion cell.

Immediately after graduating from Texas A&M University, he continued his graduate career at the Woodruff School of Mechanical Engineering at the Georgia Institute of Technology. After completing a thesis investigation in droplet generation from a liquid layer for cooling, he graduated from the Georgia Institute of Technology. In August 2004, he began his new academic career when he joined the Mechanical Engineering Department at the University of South Florida, in Tampa, FL.